#### POLITECNICO DI MILANO

# Dipartimento di Fisica Corso di Dottorato in Fisica – XVII Ciclo



Generation of tunable few-optical-cycles laser pulses and their application to spectroscopy of organic molecules

Coordinatore: Prof. Lucio BRAICOVICH

Tutor: Prof. Giulio CERULLO

Candidato:

Dario POLLI

## **INDEX**

Fore	eword		i
Cha	pter 1. B	road-band parametric amplifier in the visible.	1
1.1	Introdu	ection	1
1.2	Theory	Theory of optical parametric amplification	
	1.2.1	The optical parametric amplification process	4
	1.2.2	Phase Matching	9
	1.2.3	Parametric amplification with ultrashort pulses	10
1.3	Optical	Optical parametric amplifier designs	
	1.3.1	General OPA design	17
	1.3.2	Optical Parametric Amplifiers in the visible	20
1.4	Ultrabroadband Visible Optical Parametric Amplifier		
	1.4.1	Noncollinear Visible Optical Parametric Amplifier	23
	1.4.2	Experimental Setup	25
	1.4.3	Results: amplified bandwidth and chirp	28
1.5	Pulse c	ompression using double-chirped mirrors	31
1.6	Cross-c	correlation SPIDER characterization of the compressed OPA pulses	35
	1.6.1	Introduction	35
	1.6.2	Theory of SPIDER	36
	1.6.3	SPIDER for visible pulses	37
	1.6.4	Results	39
1.7	Conclu	sions and perspectives	41
Cha		wo-colours pump-probe system broadly tunable ver the visible and near-IR with sub-20-fs resolution.	43
2.1	Introdu	ection	43
2.2		tion of femtosecond pulses from the infrared to the ultraviolet	
	wavele	ngth region	44

#### INDEX

	2.2.1	System layout and design considerations	44
	2.2.2	Tunable visible non-collinear optical parametric amplifier	47
	2.2.3	Near-IR non-collinear optical parametric amplifier	48
	2.2.4	Generation of blue pulses	50
	2.2.5	Generation of UV pulses	<u>5</u> 1
2.3	Pump-	probe system	52
	2.3.1	Theory of pump-probe	52
	2.3.2	Pump-probe experimental set-up	55
Cha		ltrafast spectroscopy of carotenoids: etection of an intermediate excited state.	59
3.1		action	
3.2		events of energy relaxation in β-carotene and lycopene	
	3.2.1	Ultrafast internal conversion in β-carotene	
	3.2.2	Data analysis	
	3.2.3	Ultrafast internal conversion in lycopene	
	3.2.4	The S <sub>x</sub> intermediate state revealed	67
3.3	Conjug	gation length dependence of internal conversion in carotenoids	69
	3.3.1	Ultrafast internal conversion in long carotenoids	70
	3.3.2	Ultrafast internal conversion in a short carotenoid	74
3.4	Discus	sion and conclusions	76
Cha		nergy Transfer from Carotenoids to Bacterio-Chlorophylls  LH2 complexes: detection of an intermediate excited state	79
4.1	Introdu	action	79
4.2	Experi	mental Results	83
	4.2.1	Sample preparation	83
	4.2.2	Ultrafast dynamics of okenone in solution	83
	4.2.3	Ultrafast dynamics of okenone inside the LH2	
		complex of C. purpuratum	90
	4.2.4	Ultrafast dynamics of rhodopin glucoside in solution	92

#### INDEX

I ict	of nublic	cations	119
References			
	4.3.3	Conclusions	102
	4.3.2	Coherent oscillations analysis	100
	4.3.1	Carotenoid-to-BChl energy transfer	97
4.3	Discus	sion and conclusions	97
		inside the LH2 complex of R. acidophila	95
	4.2.5	Ultrafast dynamics of rhodopin glucoside	

Foreword

#### **Foreword**

Ultrafast optical spectroscopy is a powerful technique for the investigation of electronic and vibrational dynamics in a variety of systems and has provided valuable information on the dynamical properties of atoms, molecules and solids. In a classical "pump-probe" experiment, the system is resonantly excited by a "pump" pulse and its subsequent evolution is monitored by the pump-induced absorption change of a delayed "probe" pulse. Our capability to observe fast dynamical processes is limited by the duration of the light pulses available to us, thus calling for the generation of shorter and shorter pulses; on the other hand, the need to excite a system on resonance and probe optical transitions occurring at different photon energies requires frequency tunability of both pump and probe pulses. Therefore, an ideal system for ultrafast optical spectroscopy should be able to deliver pulses that are as short as possible and broadly tunable; in addition, the frequencies of pump and probe pulses should be independently selectable.

The 1990s have witnessed a revolution in ultrafast laser technology, thanks to the advent of solid state active materials, such as Ti:sapphire, and powerful mode-locking techniques, such as Kerr lens mode-locking and the chirped pulse amplification technique. The increase in peak power achieved makes it possible to access a whole new class of nonlinear optical phenomena, triggering a renaissance in the field of nonlinear optics. These advances have led to the development of the collinear Optical Parametric Amplifier (OPA) as a simple and reliable source of tunable femtosecond pulses. The combination of two OPAs allows achieving independently-tunable pump and probe pulses. However, the gain bandwidth of OPAs is often limited by the wavelength dependence of the phase matching condition.

The purpose of this study is to implement a two-colour pump-probe system based on OPAs with as high as possible temporal resolution. This is achieved by exploiting the non-collinear interaction geometry, which enables to broaden the phase matching bandwidth of the OPA. By carefully controlling the dispersion of the OPA spectrum it is consequently possible to obtain few-optical-cycle pulses from the ultraviolet to the near-infrared wavelength region.

Foreword

Chapter 1 describes the non-collinear visible OPA apparatus, from the generation of the white light to its amplification, compression and complete pulse temporal profile characterization. Chapter 2 illustrates various extensions of the visible OPA set-up to other spectral ranges and their implementation into a two-colour pump-probe system with sub-20-fs temporal resolution.

In the second part of this work we present an application of this spectroscopic device to a very important multidisciplinary problem, interesting for physicists, chemists and biologists: the study of the early events of excited state relaxation in carotenoids. Carotenoids are ubiquitous pigments in photosynthetic systems, contributing to the efficiency of the light harvesting process. Light absorbed by carotenoids in the blue, green and yellow regions of the spectrum is transferred to (bacterio)chlorophylls, thereby making it available to drive photosynthesis. They also have distinct structural functions and perform the essential function of organism photo-protection by quenching singlet oxygen. In photosynthesis the carotenoids and (bacterio)chlorophylls are typically noncovalently bound into antenna complexes and reaction centers, which are, mainly, integral membrane proteins located within the photosynthetic membranes. The photoprotective and light-harvesting roles of carotenoids are ultimately determined by the energies, structures and dynamics of their low-lying excited electronic states. A complete description of these states is therefore a prerequisite for a detailed understanding of the molecular mechanisms involved in the photosynthetic reactions. The present studies have been further stimulated by the recent determination of several high-resolution x-ray crystal structures of photosynthetic antenna complexes in purple bacteria, which have revealed the structural arrangement of the chromophores.

Traditionally, the photophysics of carotenoids has been interpreted in terms of a three-level model with internal conversion from the optically allowed  $1^1B_u^+$  state ( $S_2$ ) to a lower-lying forbidden  $2^1A_g^-$  state ( $S_1$ ), taking place in a few hundred femtoseconds. Both  $S_2$  and  $S_1$  are involved in the energy transfer to (bacterio)chlorophylls, which is the first step of photosynthesis. In Chapter 3, using the special spectroscopic system described in Chapters 1 and 2, combining high temporal resolution and broadband detection, we present the first direct evidence of the existence, in the relaxation pathway of carotenoids,

Foreword

of an additional, intermediate state  $(S_x)$  lying between  $S_2$  and  $S_1$ . This state had been predicted by theoretical models but never observed experimentally due to the lack of temporal resolution. This intermediate state enables us to explain the dependence on the number of conjugated double bonds of the conversion rate to  $S_1$ . The results presented in Chapters 3 radically change our mechanistic understanding of photosynthetic light harvesting by carotenoids.

In Chapter 4 we study the early steps of excited state dynamics of two carotenoids, okenone and rhodopin glucoside, in solution and inside the LH2 complex of two purple bacteria, C. purpuratum and R. acidophila, respectively. Exploiting our improved temporal resolution, we can follow the details of the internal conversion processes in these carotenoids; by comparing their dynamics inside and outside the LH2 complexes, we are able to directly evaluate the efficiency of the carotenoid-to-(bacterio)Chlorophylls energy transfer processes both from  $S_2$  and  $S_1$ .

Foreword iv

### Chapter 1

# Broad-band parametric amplifier in the visible

#### 1.1 Introduction

Ultrafast optical science is a rapidly evolving multidisciplinary field: the ability to excite matter with femtosecond light pulses and probe its subsequent evolution on ultrashort timescales opens up completely new fields of research in physics, chemistry, and biology [For a overview of the state of the art of ultrafast spectroscopy, see for example, Zewail, 2000; Elsaesser et al., 2001; Kobayashi et al., 2005]. Furthermore, the high intensities that can be generated using femtosecond light pulses allow us to explore new regimes of light-matter interaction [Brabec and Krausz, 2000]. The implementation of more sophisticated spectroscopic techniques has been accompanied by improvements in laser sources. Considerable effort has been dedicated to the achievement of shorter light pulses [Zhou et al., 1994; Stingl et al., 1995; Steinmeyer et al., 1999] to improve temporal resolution; other efforts have worked to expand the frequency tunability of the pulses, since this would make it possible to excite in resonance different materials, and to probe optical transitions occurring at different frequencies. Early sources of femtosecond optical pulses were based on dye laser technology [Fork et al., 1981]; in that case, some frequency tunability could be achieved by simply changing the laser dye. This flexibility, however, came at the expense of a complicated and time consuming re-optimization.

The advent of solid state active materials, such as Ti:sapphire, and powerful mode-locking techniques, such as Kerr Lens Mode-locking (KLM) [Spence et al., 1991] has unleashed a revolution in ultrafast laser technology in the 1990s. With these advances, femtosecond lasers have gained tremendously in reliability and user-friendliness,

becoming "turnkey" devices available to a wide community of non-specialists. Another landmark of femtosecond technology has been the Chirped Pulse Amplification (CPA) technique [Strickland and Mourou, 1985; Backus et al., 1998], which enabled increasing the energy of femtosecond lasers by 2-3 orders of magnitude, from the millijoule to the multi-joule level. This increase in peak power makes it possible to access a whole new class of nonlinear optical phenomena, triggering a renaissance in the field of nonlinear optics. Parallel to these developments has been the discovery of novel nonlinear optical crystals, such as β-barium borate (BBO) and lithium triborate (LBO) [Eimerl et al., 1987; Chen et al., 1989; Lin et al., 1990; Zhang et al., 1993; Borsutzky et al., 1991], combining improved optical characteristics (high nonlinear optical coefficients, low group velocity dispersion, broad transparency ranges) with high damage thresholds.

KLM Ti:sapphire lasers amplified by the CPA technique are now widely used sources of stable, energetic femtosecond pulses: however their frequency tunability is limited to a narrow range around the Fundamental Wavelength (FW) of 0.8  $\mu$ m or around the Second Harmonic (SH) of 0.4  $\mu$ m. Their tuning range can be greatly extended by using Optical Parametric Generation (OPG) [Giordamaine and Miller, 1965; Byer and Herbst, 1977; Baumgartner and Byer, 1979; Shen, 1984; Boyd, 1992]. The principle of OPG is quite simple: in a suitable nonlinear crystal, a high frequency and high intensity beam (the *pump* beam, at frequency  $\omega_p$ ) amplifies a lower frequency, lower intensity beam (the *signal* beam, at frequency  $\omega_s$ ); in addition a third beam (the *idler* beam, at frequency  $\omega_i$ , with  $\omega_i < \omega_s < \omega_p$ ) is generated. In the OPG process, signal and idler beams play an interchangeable role. We will assume that the signal is at higher frequency, i.e.  $\omega_s > \omega_i$ . In the interaction, energy conservation

$$\hbar\omega_{\rm p} = \hbar\omega_{\rm s} + \hbar\omega_{\rm i} \tag{1}$$

is satisfied; for the interaction to be efficient, also the momentum conservation (or phase matching) condition

$$\hbar \mathbf{k}_{\mathbf{p}} = \hbar \mathbf{k}_{\mathbf{s}} + \hbar \mathbf{k}_{\mathbf{i}} \tag{2}$$

where  $\mathbf{k}_p$ ,  $\mathbf{k}_s$  and  $\mathbf{k}_i$  are the wave-vectors of pump, signal and idler, respectively, must be fulfilled. The signal frequency to be amplified can vary in principle from  $\omega_p/2$  (the so-called degeneracy condition) to  $\omega_p$ , and correspondingly the idler varies from  $\omega_p/2$  to 0; at degeneracy, signal and idler have the same frequency. In summary, the OPG process transfers energy from a high-power, fixed frequency pump beam to a low-power, variable frequency signal beam, thereby generating also a third idler beam. To be efficient, this process requires very high intensities of the order of tens of GW/cm<sup>2</sup>; it is therefore eminently suited to femtosecond laser systems, which can easily achieve such intensities even with modest energies, of the order of a few microjoules.

A suitably generated weak signal beam (the so-called "seed" beam) can be amplified in one or more OPG crystals, thus obtaining an Optical Parametric Amplifier (OPA). OPAs have the drawback of requiring high pump intensities, provided only by an amplified Ti:Sa system, which operate at low repetition rates (typically from 1 to 100 kHz); on the other hand, they provide high output energies, broad frequency tunability and are simple to operate.

Femtosecond OPAs have become the most widespread source of tunable femtosecond pulses and have reached a high level of stability and reliability, becoming true workhorses of ultrafast spectroscopy. These systems are usually pumped by an amplified Ti:sapphire laser, providing pulses with mJ-level energy, ≈100 fs duration and kHz repetition rate; pumping can occur either at the FW or at the SH of the laser beam. Femtosecond OPAs have demonstrated tunability from the ultraviolet (UV) to the medium-infrared (mid-IR), and produce pulse energies up to the 100 μJ level. In addition, femtosecond OPAs have the capability of generating pulses significantly shorter than the pump pulses, exploiting the broad gain bandwidths available in the parametric interaction. They can therefore be used as effective pulse compressors.

In paragraph 1.2 we will present the theory of parametric amplification, while in section 1.3 we will describe the most common OPA designs. In paragraphs 1.4, 1.5 and 1.6 we will present our experimental results on ultrabroadband visible pulse generation, compression and characterization, respectively.

#### 1.2 Theory of optical parametric amplification

#### 1.2.1 The optical parametric amplification process

In the following we will briefly derive the coupled nonlinear equations describing the optical parametric amplification process [Giordamaine and Miller, 1965; Byer and Herbst, 1977; Baumgartner and Byer, 1979; Shen, 1984; Boyd, 1992]. We start with a linearly polarized, monochromatic plane wave at frequency  $\omega$ , propagating in the z direction

$$E(z,t) = Re\{A(z) \exp[j(\omega t - kz)]\}, \qquad (3)$$

in a medium with nonlinear polarization, at the same frequency,

$$P^{nl}(z,t) = \operatorname{Re} \{P^{nl}(z) \exp[j(\omega t - k_n z)]\}. \tag{4}$$

Within the slowly-varying-amplitude approximation  $(\frac{d^2A}{dz^2} << 2k\frac{dA}{dz})$  we can derive the following propagation equation:

$$\frac{\mathrm{dA}}{\mathrm{dz}} = -\mathrm{j} \frac{\mu_0 c_0 \omega}{2 n} P^{\mathrm{nl}} \exp\left[-\mathrm{j} \left(k_p - k\right) z\right],\tag{5}$$

where  $c_0$  is the speed of light in vacuum and n is the refractive index at frequency  $\omega$ . Eq. (5) shows that the nonlinear polarization acts as a source term driving the amplitude variations of the propagating wave.

Let us now consider the interaction of three waves, at frequencies  $\omega_p$ ,  $\omega_s$  and  $\omega_i$ , with  $\omega_i < \omega_s < \omega_p$  and  $\omega_i + \omega_s = \omega_p$ , in a medium with second-order nonlinear polarization. The component of the nonlinear polarization vector along direction *i* is expressed as

$$P_i^{nl} = \varepsilon_0 \chi_{ijk}^{(2)} E_j E_k , \qquad (6)$$

where i, j, and k each take the values x, y, and z,  $\chi^{(2)}$  is the third-rank (27 components) second-order nonlinear susceptibility tensor and the Einstein summation convention is used. For the moment we will assume that the three beams are collinear, i.e. with parallel wavevectors, although in general their polarization will be different. We will however see

later that the non-collinear interaction geometry is important and is used to achieve ultrabroad amplification bandwidths. We can now easily derive the following coupled equations [Shen, 1984; Boyd, 1992]:

$$\frac{dA_{i}}{dz} = -j \frac{\omega_{i} d_{eff}}{n_{i} c_{0}} A_{s}^{*} A_{p} \exp[-j\Delta k z], \qquad (7a)$$

$$\frac{dA_s}{dz} = -j \frac{\omega_s d_{eff}}{n_s c_0} A_i^* A_p \exp[-j\Delta k z], \qquad (7b)$$

$$\frac{dA_{p}}{dz} = -j \frac{\omega_{p} d_{eff}}{n_{p} c_{0}} A_{i} A_{s} \exp[j\Delta k z], \qquad (7c)$$

where  $d_{eff}$  is the so-called effective nonlinear optical coefficient, depending on the propagation direction and the polarization of the three beams, and  $\Delta k = k_p - k_s - k_i$  is the so-called wave-vector mismatch. Equations (7) describe a wealth of second-order nonlinear optical phenomena, such as Sum-Frequency Generation (SFG), Second-Harmonic Generation (SHG), Difference-Frequency Generation (DFG) and optical parametric amplification. By some straightforward manipulations, these three coupled equations can be cast into the form:

$$\frac{1}{\omega_{i}} \frac{dI_{i}}{dz} = \frac{1}{\omega_{s}} \frac{dI_{s}}{dz} = -\frac{1}{\omega_{p}} \frac{dI_{p}}{dz}, \tag{8}$$

where  $I_i = \frac{1}{2} \epsilon_0 c_0 n_i |A_i|^2$  is the intensity of the beam at frequency  $\omega_i$ . Eqs. (8), also known as Manley-Rowe relationships, state photon conservation and show that the three-wave interaction in second-order nonlinear media manifests itself in the energy flow from the two lower-frequency fields to the sum-frequency field or vice-versa. In the case of SFG, two powerful beams at  $\omega_i$  and  $\omega_s$  interact to produce a beam at the sum frequency  $\omega_p$ , i.e. two photons at frequencies  $\omega_i$  and  $\omega_s$  combine to produce a photon at frequency  $\omega_p$  (SHG is just a particular case with  $\omega_s = \omega_i$ ). In the case of difference frequency generation two powerful beams at frequencies  $\omega_s$  and  $\omega_p$  interact; the beam at  $\omega_p$  loses power in favour of the beam at  $\omega_s$  and of the newly generated difference frequency beam at  $\omega_i$ . In terms of

photon balance, we can say that a photon at  $\omega_p$  is split into a photon at  $\omega_i$  and a photon at  $\omega_s$ . Optical parametric amplification differs from DFG only in the initial conditions: in this case, in fact, the beam at  $\omega_s$  (signal beam) is much weaker than that at  $\omega_p$  (pump beam) and gets significantly amplified during the interaction, while at the same time the beam at  $\omega_i$  (idler beam) is generated.

Neglecting pump depletion ( $A_p \cong cost.$ ) and assuming an initial signal intensity  $A_{s0}$  (seed beam) and no initial idler beam ( $A_{i0} = 0$ ) equations (7) can be solved to get the signal and idler intensities after a length L of nonlinear crystal:

$$I_{s}(L) = I_{s0} \left[ 1 + \frac{\Gamma^{2}}{g^{2}} \sinh^{2}(gL) \right], \qquad (9a)$$

$$I_{i}(L) = I_{s0} \frac{\omega_{i}}{\omega_{s}} \frac{\Gamma^{2}}{g^{2}} \sinh^{2}(gL), \qquad (9b)$$

where

$$g = \sqrt{\Gamma^2 - \left(\frac{\Delta k}{2}\right)^2} \,, \tag{10}$$

$$\Gamma^{2} = \frac{\omega_{i} \, \omega_{s} \, d_{\text{eff}}^{2} \left| A_{p} \right|^{2}}{n_{i} n_{s} c_{0}^{2}} = \frac{2\omega_{i} \, \omega_{s} \, d_{\text{eff}}^{2} I_{p}}{n_{i} n_{s} n_{p} \varepsilon_{0} c_{0}^{3}} = \frac{8\pi^{2} d_{\text{eff}}^{2} I_{p}}{n_{i} n_{s} n_{p} \lambda_{i} \lambda_{s} \varepsilon_{0} c_{0}}.$$
(11)

For the case of perfect phase matching ( $\Delta k = 0$ ,  $g = \Gamma$ ) and in the large gain approximation ( $\Gamma L >> 1$ ), equations (9) simplify to

$$I_s(L) \cong \frac{1}{4} I_{s0} \exp(2\Gamma L),$$
 (12a)

$$I_i(L) \cong \frac{\omega_i}{4\omega_s} I_{s0} \exp(2\Gamma L).$$
 (12b)

Note that the ratio of signal and idler intensities is such that an equal number of signal and idler photons are generated. Equations (12) allow defining a parametric gain as

$$G = \frac{I_s(L)}{I_{s0}} = \frac{1}{4} \exp(2\Gamma L), \qquad (13)$$

growing exponentially with the crystal length L and with the nonlinear coefficient  $\Gamma$ . Note that the exponential growth of signal and idler waves along the crystal is qualitatively different from the quadratic growth occurring in other second-order nonlinear phenomena, such as sum-frequency generation or second harmonic generation. This difference can be understood intuitively in the following way: in a strong pump field, the presence of a seed photon at the signal wavelength stimulates the generation of an additional signal photon and of a photon at the idler wavelength. Likewise, due to the symmetry of signal and idler, the amplification of an idler photon stimulates the generation of a signal photon. Therefore, the generation of the signal field reinforces the generation of the idler field and vice versa, giving rise to a positive feedback that is responsible for the exponential growth of the waves.

Equation (11) shows that the coefficient  $\Gamma$  depends on: (i) the pump intensity; (ii) the signal and idler wavelengths  $\lambda_s$  and  $\lambda_i$ ; (iii) the nonlinear coefficient  $d_{eff}$ ; (iv) the refractive indexes at the three interacting wavelengths. To characterize a parametric interaction and compare different nonlinear materials, it is possible to define the following figure of merit:

$$FM = \frac{d_{eff}}{\sqrt{\lambda_s \lambda_i n_p n_s n_i}}.$$
 (14)

In the following we discuss some examples of parametric gain calculation relevant to ultrashort pulses, assuming perfect phase matching. Figure 1.1 shows a plot of the parametric gain in BBO, at the infrared pump wavelength  $\lambda_p = 0.8~\mu m$  and the signal wavelength  $\lambda_s = 1.2~\mu m$ , as a function of pump intensity and for different crystal lengths. The gain scales as the exponential of the square root of the pump intensity:  $G \propto \exp(\sqrt{I_p})$ . At a pump intensity  $I_p = 25~GW/cm^2$ , a gain  $G \cong 6$  is calculated for a crystal length L = 1~mm; however it rapidly increases to  $G \cong 2 \times 10^6~for$  L = 5~mm. The same gain can be obtained with a 3-mm crystal increasing the pump intensity to 75 GW/cm<sup>2</sup>. The same plot for BBO at the visible pump wavelength  $\lambda_p = 0.4~\mu m$  and the signal wavelength  $\lambda_s = 0.6~\mu m$  is shown in Fig. 1.2. In this case, at a pump intensity  $I_p = 25~GW/cm^2$ , a gain  $G \cong 128~form$  is calculated for a crystal length L = 1~mm, about a factor of 20 larger than in the case of

infrared pump. The higher gain is due to the smaller values of  $\lambda_s$  and  $\lambda_i$ , which increase the figure of merit of the parametric interaction. Despite the improvement in figure of merit using a visible pump, the group velocity mismatch between the interacting pulses, as we will see later, prevents the use of long nonlinear crystals in this case.

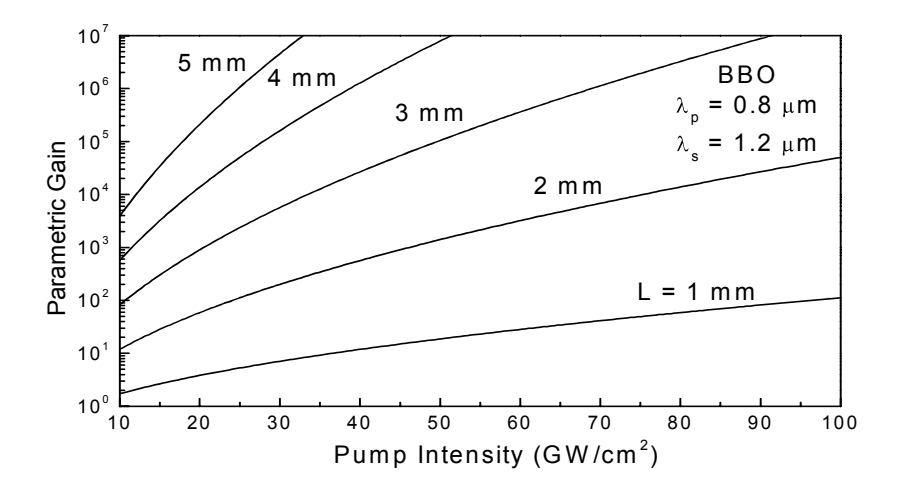


FIG 1.1. Parametric gain for an OPA at the pump wavelength  $\lambda_p$ =0.8  $\mu$ m and the signal wavelength  $\lambda_s$ =1.2  $\mu$ m, using type I phase matching in BBO (d<sub>eff</sub>=2 pm/V).

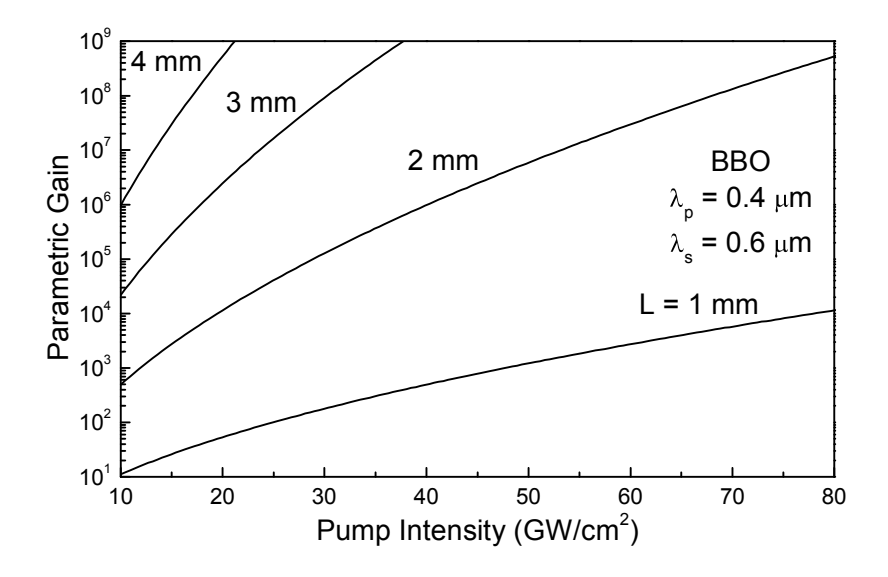


FIG 1.2. Parametric gain for an OPA at the pump wavelength and the signal wavelength  $\lambda_s$ =0.6  $\mu$ m, using type I phase matching in BBO BBO (d<sub>eff</sub>=2 pm/V).

#### 1.2.2 Phase matching

We now address the problem of phase matching: to achieve maximum gain, we must satisfy the phase matching condition,  $\Delta k = 0$ , which can be recast in the form

$$n_{p} = \frac{n_{i}\omega_{i} + n_{s}\omega_{s}}{\omega_{p}}.$$
 (15)

It is easy to show that this condition cannot be fulfilled in bulk isotropic materials in the normal dispersion region  $(n_i < n_s < n_p)$ . In some birefringent crystals, phase matching can be achieved by choosing for the higher frequency pump wave  $(\omega_p)$  the polarization direction giving the lower refractive index. In the case, common in femtosecond OPAs, of negative uniaxial crystals  $(n_e < n_o)$ , the pump beam is polarized along the extraordinary direction. If both signal and idler beams have the same ordinary polarization (perpendicular to that of the pump beam) we talk about type I (or  $o_s + o_i \rightarrow e_p$ ) phase matching. If one of the two is polarized parallel to the pump beam, we talk about type II phase matching; in this case either the signal  $(e_s + o_i \rightarrow e_p)$  or the idler  $(o_s + e_i \rightarrow e_p)$  can have the extraordinary polarization [Dmitriev et al., 1991]. Both types of phase matching can be used and have their specific advantages according to the system under consideration. Usually the phase matching condition is achieved by adjusting the angle  $\theta_m$  between the wave vector of the propagating beams and the optical axis of the nonlinear crystal (angular phase matching). Alternatively, the refractive indexes can be changed by adjusting the crystal temperature (temperature phase matching).

As an example, we consider the case of a negative uniaxial crystal, for which type I phase matching is achieved when [Koechner, 1996]

$$n_{ep}(\theta_{m})\omega_{p} = n_{os}\omega_{s} + n_{oi}\omega_{i}, \qquad (16)$$

which allows to compute  $n_{ep}(\theta_m)$ . Recalling the dependence of the extraordinary index on the propagation direction in uniaxial crystals

$$\frac{1}{n_{\rm ep}^2(\theta_{\rm m})} = \frac{\sin^2(\theta_{\rm m})}{n_{\rm ep}^2} + \frac{\cos^2(\theta_{\rm m})}{n_{\rm op}^2},\tag{17}$$

where  $n_{ep}$  and  $n_{op}$  are the principal extraordinary and ordinary refractive indexes at the pump wavelength, the phase matching angle can then be obtained as:

$$\theta_{\rm m} = a \sin \left[ \frac{n_{\rm ep}}{n_{\rm ep}(\theta_{\rm m})} \sqrt{\frac{n_{\rm op}^2 - n_{\rm ep}^2(\theta_{\rm m})}{n_{\rm op}^2 - n_{\rm ep}^2}} \right]. \tag{18}$$

Figures 1.3 and 1.4 show the phase matching angles as a function of wavelength for BBO type I and Type II OPAs at the pump wavelengths 0.8  $\mu$ m and 0.4  $\mu$ m. Note that, in general, the phase matching angle shows a less pronounced wavelength dependence for type I with respect to type II phase matching.

#### 1.2.3 Parametric amplification with ultrashort pulses

So far we have studied the interaction of three monochromatic waves, i.e. cw beams. Let us now consider the case, relevant for femtosecond OPAs, of three pulses like

$$E_i(z,t) = \operatorname{Re}\{A_i(z,t) \exp[j(\omega_i t - k_i z)]\}, \tag{19}$$

propagating in the nonlinear crystal with different group velocities  $v_{gi} = \frac{d\omega_i}{dk_i}$ . Within the

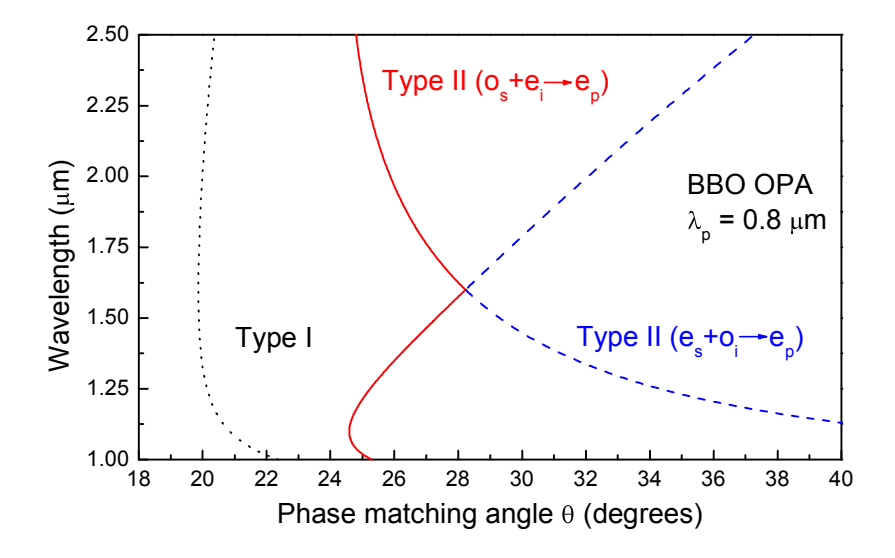


FIG. 1.3. Angle tuning curves for a BBO OPA at the pump wavelength  $\lambda_p$ =0.8  $\mu$ m for type I phase matching (black dotted line), type II  $o_s+e_i\rightarrow e_p$  phase matching (red solid line), and type II  $e_s+o_i\rightarrow e_p$  phase matching (blue dashed line).

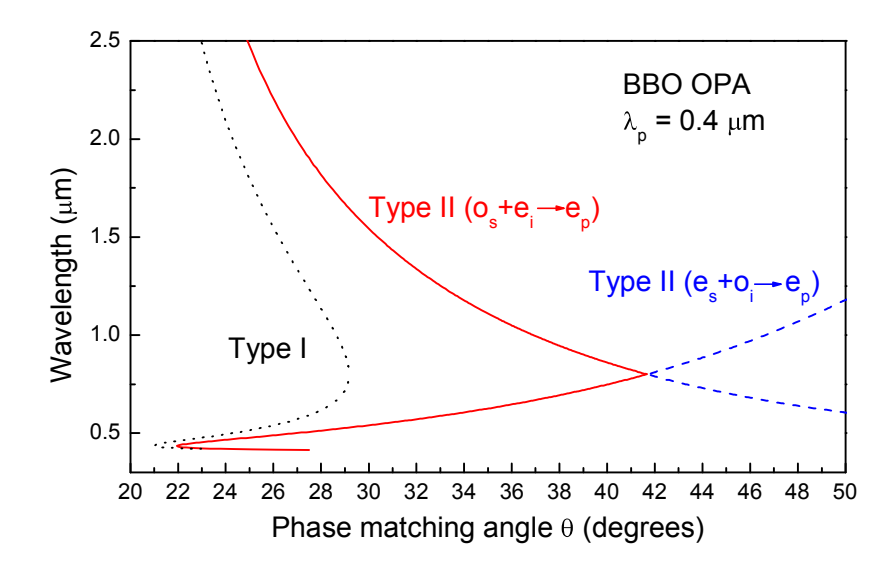


FIG. 1.4. Angle tuning curves for a BBO OPA at the pump wavelength  $\lambda_p$ =0.4  $\mu$ m for type I phase matching (black dotted line), type II  $o_s+e_i\rightarrow e_p$  phase matching (red solid line), and type II  $e_s+o_i\rightarrow e_p$  phase matching (blue dashed line).

slowly varying amplitude approximation and neglecting pulse lengthening due to second or higher order dispersion (which is a good approximation for pulses in the 100-fs range), we obtain the following equations [Akmanov et al., 1968, 1992]

$$\frac{\partial A_{s}}{\partial z} + \frac{1}{v_{os}} \frac{\partial A_{s}}{\partial t} = -j \frac{\omega_{s} d_{eff}}{n_{s} c_{0}} A_{i}^{*} A_{p} \exp[-j\Delta k z], \qquad (20a)$$

$$\frac{\partial A_{i}}{\partial z} + \frac{1}{v_{oi}} \frac{\partial A_{i}}{\partial t} = -j \frac{\omega_{i} d_{eff}}{n_{i} c_{0}} A_{s}^{*} A_{p} \exp[-j\Delta k z], \qquad (20b)$$

$$\frac{\partial A_{p}}{\partial z} + \frac{1}{v_{gp}} \frac{\partial A_{p}}{\partial t} = -j \frac{\omega_{p} d_{eff}}{n_{p} c_{0}} A_{s} A_{i} \exp[+j\Delta k z]. \tag{20c}$$

Note that equations (20) neglect also third order nonlinear effects (self and cross phase modulation). By transforming to a frame of reference that is moving with the group velocity of the pump pulse  $(\tau = t - \frac{z}{v_{gp}})$  we obtain the equations

$$\frac{\partial A_{s}}{\partial z} + \left(\frac{1}{v_{os}} - \frac{1}{v_{on}}\right) \frac{\partial A_{s}}{\partial \tau} = -j \frac{\omega_{s} d_{eff}}{n_{s} c_{0}} A_{i}^{*} A_{p} \exp[-j\Delta k z], \qquad (21a)$$

$$\frac{\partial A_{i}}{\partial z} + \left(\frac{1}{v_{gi}} - \frac{1}{v_{gp}}\right) \frac{\partial A_{i}}{\partial \tau} = -j \frac{\omega_{i} d_{eff}}{n_{i} c_{0}} A_{s}^{*} A_{p} \exp[-j\Delta k z], \qquad (21b)$$

$$\frac{\partial A_{p}}{\partial z} = -j \frac{\omega_{p} d_{eff}}{n_{p} c_{0}} A_{s} A_{i} \exp[j\Delta k z].$$
 (21c)

Despite the many simplifications, equations (21) capture the main issues of parametric amplification with ultrashort pulses, which are related to Group Velocity Mismatch (GVM) between the interacting pulses. In particular, GVM between the pump and the amplified (signal and idler) pulses limits the interaction length over which parametric amplification takes place, while GVM between the signal and the idler beams limits the phase matching bandwidth.

The useful interaction length for parametric interaction is quantified by the pulse splitting length, which is defined as the propagation length after which the signal (or the idler) pulse separates from the pump pulse in the absence of gain, and is expressed as

$$l_{jp} = \frac{\tau}{\delta_{jp}} \qquad (j = s, i)$$
 (22)

where  $\tau$  is the pump pulse duration and  $\delta_{jp} = \frac{1}{v_{gj}} - \frac{1}{v_{gp}}$  is the GVM between pump and

signal/idler. Note that the pulse splitting length becomes shorter for decreasing pulse duration and for increasing GVM. GVM depends on the crystal type, pump wavelength and type of phase matching. Figures 1.5 and 1.6 show examples of GVM curves for a BBO OPA pumped by 0.8  $\mu$ m and 0.4  $\mu$ m pulses, respectively. Note that, due to greater dispersion values in the visible, GVM is in general larger in this wavelength range.

For crystal lengths shorter than the pulse splitting length, GVM effects can be neglected, to a first approximation, and the equations (9-12), valid for cw beams, can be used for gain calculations. For crystals longer than or comparable to the pulse splitting length, GVM plays a crucial role and equations (21) must be solved numerically to properly account for it. There is a qualitatively significant difference between the cases in which  $\delta_{sp}$  and  $\delta_{ip}$  have the same or different signs. When  $\delta_{sp}$   $\delta_{ip} > 0$ , both the signal and the idler pulses walk away from the pump in the same direction, so that the gain rapidly

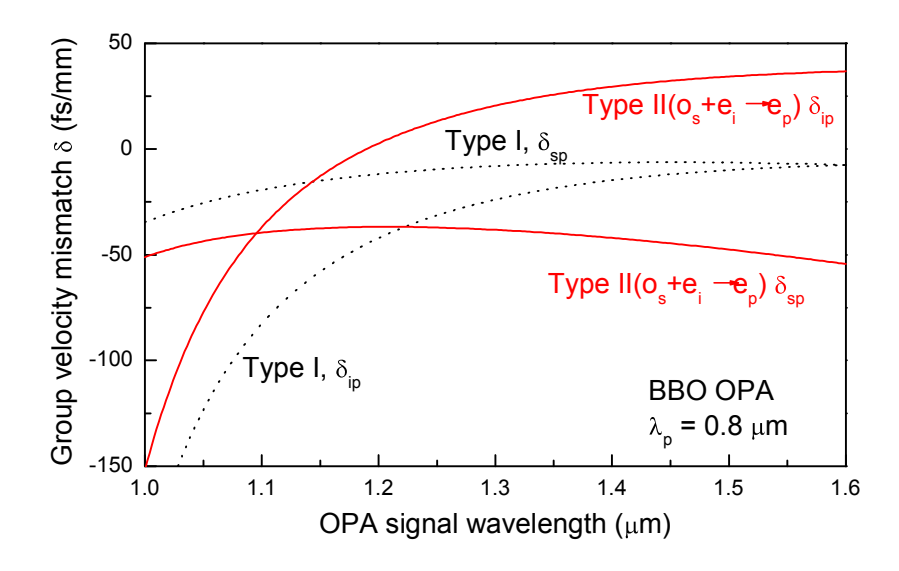


FIG. 1.5. Pump-signal ( $\delta_{sp}$ ) and pump-idler ( $\delta_{ip}$ ) group velocity mismatch curves for a BBO OPA at the pump wavelength  $\lambda_p$ =0.8  $\mu$ m for type I phase matching (black dotted line) and type II  $o_s+e_i\rightarrow e_p$  phase matching (red solid line).

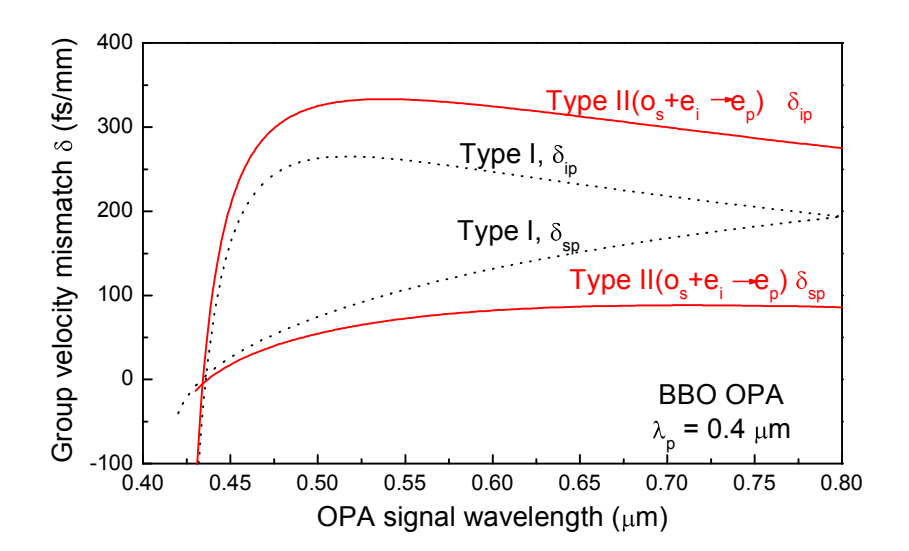


FIG. 1.6. Pump-signal ( $\delta_{sp}$ ) and pump-idler ( $\delta_{ip}$ ) group velocity mismatch curves for a BBO OPA at the pump wavelength  $\lambda_p$ =0.4  $\mu$ m for type I phase matching (black dotted line) and type II  $o_s+e_i\rightarrow e_p$  phase matching (red solid line).

decreases for propagation distances longer than the pulse splitting length and eventually saturates. On the other hand, when  $\delta_{sp}$   $\delta_{ip}$  < 0 signal and idler pulses move in opposite direction with respect to the pump; in this way the signal and idler pulses tend to stay localized under the pump pulse and the gain grows exponentially even for crystal lengths well in excess of the pulse splitting length. To try to rationalize this effect, we can

consider the situation in which the signal pulse has moved slightly to the left and the idler pulse to the right of the pump pulse: during the parametric process, the signal pulse generates idler photons, which move to the right, i.e. towards the peak of the pump; on the other hand the idler pulse will generate signal photons which in turn move to the left, again towards the peak of the pump. This concentration of photons under the peak of the pump explains the exponential gain growth. In Fig. 1.7 we show an example of solution of equations (21) for the case  $\delta_{sp} \delta_{ip} > 0$ ; we consider a type I BBO OPA pumped at 0.4  $\mu m$  with signal wavelength  $\lambda_s = 0.7~\mu m$ , with GVMs  $\delta_{sp} = 167$  fs/mm and  $\delta_{ip} = 220$ fs/mm. We see that, after an initial growth, the gain rapidly tends to saturate because both signal and idler pulses temporally separate from the pump. Note that, because the trailing edge of the pulse resides for a longer time in the amplification region, there is a modest pulse shortening (20-30%) and asymmetry. The case  $\delta_{sp} \delta_{ip} < 0$  is shown in Fig. 1.8; we consider a type II BBO OPA pumped at 0.8  $\mu$ m with signal wavelength  $\lambda_s = 1.5 \mu$ m, having group velocity mismatches  $\delta_{ip} = -47.5$  fs/mm and  $\delta_{sp} = 34.6$  fs/mm. Here we see that the signal growth stays exponential for propagation distances well exceeding the pulse splitting length and that the signal pulse tends to stay localized under the pump.

In the following we will show that GVM between signal and idler pulses determines

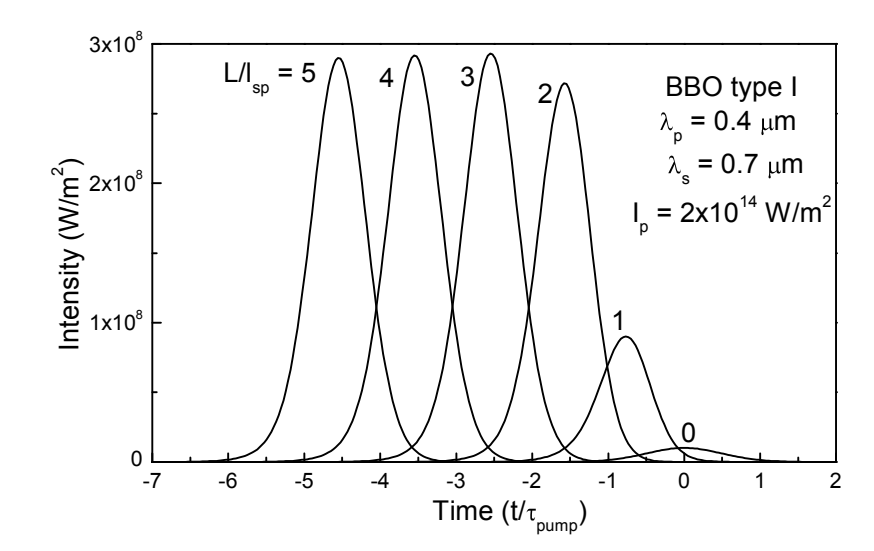


FIG. 1.7. Signal pulse evolution for a BBO type I OPA with  $\lambda_p$ =0.4  $\mu$ m,  $\lambda_s$ =0.7  $\mu$ m, for different lengths L of the nonlinear crystal. Pump intensity is 20 GW/cm<sup>2</sup>. Time is normalized to the pump pulse duration and the crystal length to the pump-signal pulse splitting length.

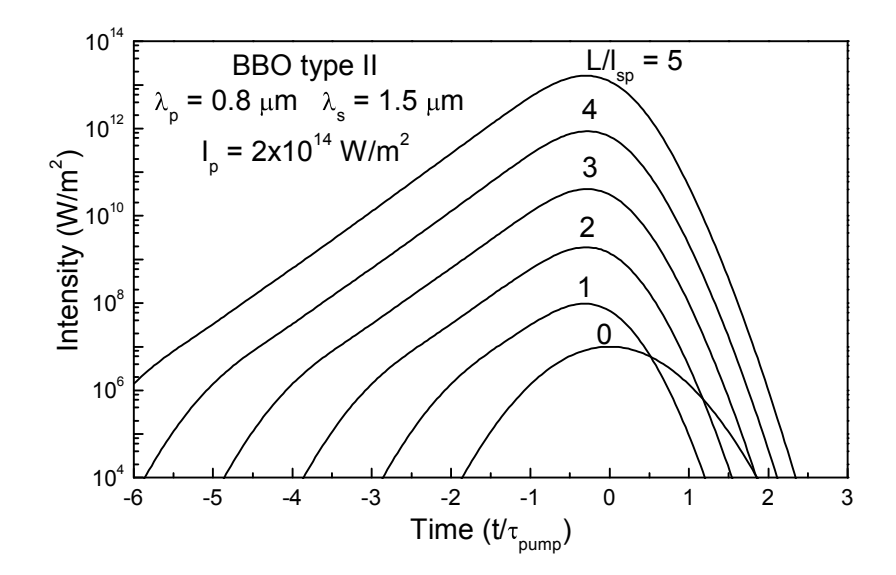


FIG. 1.8. Signal pulse evolution for a BBO type II OPA with  $\lambda_p$ =0.8  $\mu$ m,  $\lambda_s$ =1.5  $\mu$ m, for different lengths L of the nonlinear crystal. Pump intensity is 20 GW/cm<sup>2</sup>. Time is normalized to the pump pulse duration and the crystal length to the pump-signal pulse splitting length.

the phase matching bandwidth for the parametric amplification process. Let us assume that perfect phase matching is achieved for a given signal frequency  $\omega_s$  (and for the corresponding idler frequency  $\omega_i = \omega_p - \omega_s$ ). If the signal frequency increases to  $\omega_s + \Delta \omega$ , by energy conservation the idler frequency decreases to  $\omega_i - \Delta \omega$ . The wave-vector mismatch can then be approximated to the first order as:

$$\Delta k \cong -\frac{\partial k_s}{\partial \omega_s} \Delta \omega + \frac{\partial k_i}{\partial \omega_i} \Delta \omega = \left(\frac{1}{v_{gi}} - \frac{1}{v_{gs}}\right) \Delta \omega. \tag{23}$$

The FWHM phase matching bandwidth can then, within the large-gain approximation, be calculated as:

$$\Delta v \cong \frac{2(\ln 2)^{1/2}}{\pi} \left(\frac{\Gamma}{L}\right)^{1/2} \frac{1}{\left|\frac{1}{v_{gs}} - \frac{1}{v_{gi}}\right|}.$$
 (24)

Large GVM between signal and idler waves dramatically decreases the phase matching bandwidth; large gain bandwidth can be expected when the OPA approaches degeneracy  $(\omega_s \rightarrow \omega_i)$  in type-I phase matching or in the case of group-velocity matching

between signal and idler ( $v_{gs} = v_{gi}$ ). Obviously, in this case Eq. (24) loses validity and the phase mismatch  $\Delta k$  must be expanded to the second order, giving:

$$\Delta v = 2 \frac{\left(\ln 2\right)^{1/4}}{\pi} \left(\frac{\Gamma}{L}\right)^{1/4} \frac{1}{\left|\frac{\partial^2 \mathbf{k}_s}{\partial \omega_s^2} + \frac{\partial^2 \mathbf{k}_i}{\partial \omega_i^2}\right|}.$$
 (25)

Figures 1.9 and 1.10 show typical plots of phase matching bandwidths for BBO OPAs, pumped at 0.8 μm and 0.4 μm, respectively. We see a remarkable difference between type I and type II phase matching: for type II interaction, the bandwidth is smaller than in type I and stays more or less constant over the tuning range, while for type I interaction, as previously said, the bandwidth increases as the OPA approaches degeneracy. These features can be exploited for different applications: type I phase matching is used to achieve the shortest pulses, while type II phase matching allows obtaining relatively narrow bandwidths over broad tuning ranges, which are required for many spectroscopic investigations.

So far we have only considered a collinear interaction, in which, once the phase matching condition ( $\Delta k = 0$ ) is achieved, the group velocities of signal and idler, and thus

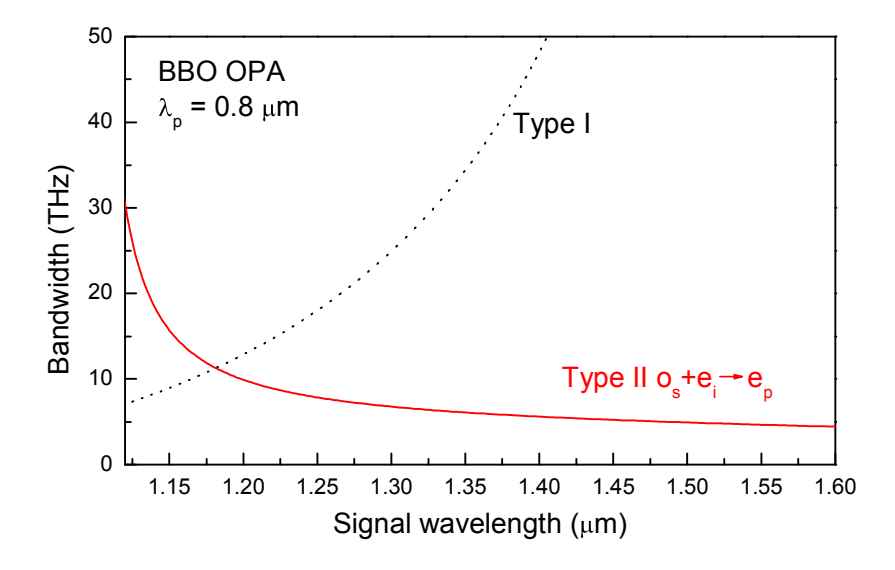


FIG. 1.9. Phase matching bandwidth for a BBO OPA at the pump wavelength  $\lambda_p$ =0.8 µm for type I phase matching (black dotted line) and type II  $o_s$ + $e_i$ → $e_p$  phase matching (red solid line). Crystal length is 4 mm and pump intensity 50 GW/cm<sup>2</sup>.

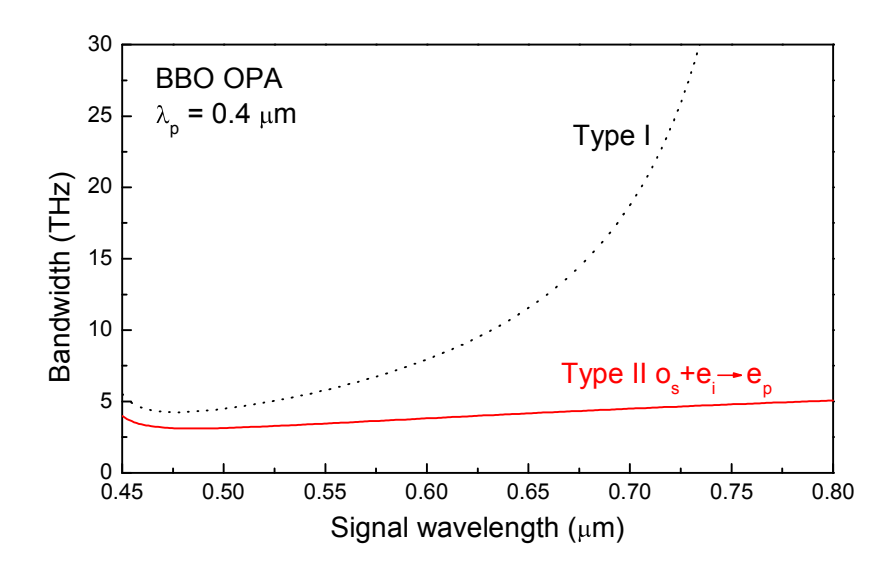


FIG. 1.10. Phase matching bandwidth for a BBO OPA at the pump wavelength  $\lambda_p$ =0.4  $\mu$ m for type I phase matching (black dotted line) and type II o<sub>s</sub>+e<sub>i</sub>→e<sub>p</sub> phase matching (red solid line). Crystal length is 2 mm and pump intensity 100 GW/cm<sup>2</sup>.

the phase matching bandwidth, are set. In paragraph 1.4 we will see that in a non-collinear interaction there is an additional degree of freedom, the pump-signal angle  $\alpha$ ; suitably selecting this angle, it is often possible to simultaneously achieve phase matching and group velocity matching between signal and idler, thus obtaining very broad gain bandwidths.

#### 1.3 Optical parametric amplifier designs

#### 1.3.1 General OPA design

Although a great variety of femtosecond optical parametric amplifier designs have been reported, there are a few basic principles underlying the different implementations. Before illustrating in detail visible OPA designs, we will try to present a very general description of the operating principles of an OPA, according to the scheme shown in Fig. 1.11. Femtosecond OPAs are in general pumped by amplified Ti:sapphire lasers: standard systems typically run at 1 kHz repetition rate and generate pulses at the wavelength

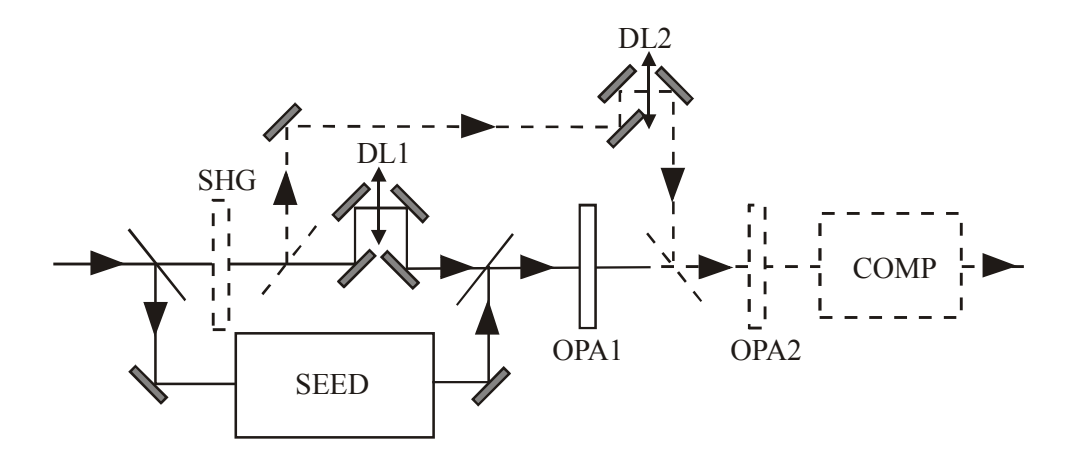


FIG. 1.11. Scheme of an ultrafast optical parametric amplifier. SEED: seed generation stage; DL1, DL2: delay lines; OPA1, OPA2 parametric amplification stages; COMP: compressor.

 $\lambda \cong 0.8~\mu m$ , with 0.5–1-mJ energy and duration ranging from 50 fs to 150 fs. Other work has reported OPAs pumped by systems running at much higher repetition rate (up to 250 kHz) but with much lower pulse energy (5–10  $\mu$ J) [Norris, 1992]. Pumping can take place at the FW or at the SH of the Ti:sapphire laser (i.e. 800 or 400 nm). Since the optical parametric amplification process consists of the interaction of a weak signal beam with a strong pump beam, the first stage of any OPA system is the generation of the initial signal beam, the so-called "seed" beam. Since the seed beam is at a different frequency from the pump beam, a nonlinear optical process is required for its generation. Two different techniques have been used for the seed generation: parametric superfluorescence and white-light continuum generation.

Parametric superfluorescence [Shen, 1984; Harris et al., 1967] is a parametric amplification of the vacuum or quantum noise, and can be also thought as two-photon spontaneous emission from a virtual level excited by the pump field. In practice it is simply achieved by pumping a suitable nonlinear crystal, which is often of the same types as the ones used in the subsequent OPA stages; amplification will occur at those wavelengths for which the parametric interaction is phase-matched. The advantage of parametric superfluorescence is the possibility of achieving large amplification and substantial seed pulse energies; its disadvantage is the inherent fluctuations of a process starting from quantum noise, and the poor spatial quality of the generated seed beam.

White light generation [Alfano, 1989; Fork et al., 1983] occurs when an intense ultrashort pulse is focused inside a transparent material, such as fused silica or sapphire: as a result of the interplay between self-focusing and self-phase modulation, a large spectral broadening takes place. Although the processes occurring during the generation of white-light continuum are still not fully understood [Gaeta, 2000], its properties are very good for its use as an OPA seed. When focusing 0.8- $\mu$ m, 100-fs pulses into a sapphire plate, with thickness ranging from 1 to 3 mm, the threshold for white-light generation is around 1  $\mu$ J (the exact value depends on the focusing conditions). The continuum spectrum extends throughout the visible (down to  $\approx$ 0.42  $\mu$ m) and the near-IR (up to  $\approx$ 1.5  $\mu$ m), with an energy of approximately 10 pJ per nm of bandwidth. Under the correct conditions (i.e. a single self-focused filament) the white light has an excellent spatial quality, with a circular gaussian beam, and a very high pulse-to-pulse stability. When using materials with high thermal conductivity and low UV absorption such as sapphire, no long-term degradation of the material is experienced.

Following generation of the seed pulse, the pump and seed pulses are combined in a suitable nonlinear crystal, in a first parametric amplification stage (preamplifier). To achieve temporal overlap, their relative timing must be adjusted by a delay line. Often the pump spot size in the nonlinear crystal is set by a telescope and is chosen to achieve the highest possible gain without causing optical damage of the crystal, or inducing thirdorder nonlinear effects (self focusing, self phase modulation or white light generation) that would cause beam distortion or breakup. In case of parametric superfluorescence seed, the preamplifier is also used as a spatial filter, to improve the spatial coherence of the signal beam by amplifying only those spatial components of the superfluorescence that overlap the pump beam in the crystal. After the first amplification stage, the signal beam can be further amplified in a second stage, power amplifier. Usually this stage is driven into saturation, i.e. with significant pump depletion and conversion efficiency above 30%. In this regime, the amplified energy is less sensitive to seed fluctuations, and high pulse stability can be achieved. The purpose of using two amplification stages instead of one long crystal is twofold: (i) the GVM between pump and signal pulses in the first stage can be compensated by a delay line; (ii) this scheme gives the flexibility of separately adjusting the pump intensity, and thus the parametric gain, in the two stages. After the power amplifier, signal and idler beams are separated from the pump and from each other using dichroic filters or mirrors. Finally, in case of broadband amplification, a pulse compressor is used to obtain Transform-Limited (TL) pulse duration.

#### 1.3.2 Optical Parametric Amplifiers in the visible

The generation of femtosecond pulses tunable in the visible is important for a variety of spectroscopic applications, because many systems of interest in physics, chemistry and biology have absorption bands in this range. A straightforward way of achieving tunable visible pulses consists in frequency doubling the output of an 0.8-µmpumped near-IR OPA [Yakovlev et al., 1994]; however, since absorption of the idler in the nonlinear crystal sets a blue tuning limit of  $\approx 1.1 \mu m$ , the SH would be tunable down to only 0.55 µm, leaving a substantial part of the visible range uncovered. Pumping with the SH of a Ti:sapphire laser around 0.4 µm, the signal can be tuned through most of the visible range, from ≈0.45 μm to degeneracy (0.8 μm). Correspondingly, the idler tunes from 0.8 µm to 2.5 µm; this fills the gap in the tuning range for near-IR OPAs [Yakovlev et al., 1994; Seifert et al., 1994; Nisoli et al., 1994]. Visible OPAs [Reed et al., 1994, 1995; Petrov and Noack, 1995; Greenfield and Wasielewski, 1995; Di trapani et al., 1997] in general obtain lower energies than near-IR ones, because of the lower pump energy available from a frequency-doubled pump. Furthermore GVM is much larger in the visible range (see Fig. 1.6), which limits the use of long nonlinear crystals. This disadvantage is partially compensated for by the larger figures of merit for parametric interaction in the visible. Also for visible OPAs the most popular nonlinear material is BBO. Type II phase matching provides gain bandwidths that are narrower and stay essentially constant over the tuning range, which may be beneficial for some spectroscopic applications [Greenfield and Wasielewski, 1995].

Figure 1.12 shows a typical visible OPA design [Reed et al., 1994, 1995]; the system is pumped by an high-repetition-rate amplified Ti:sapphire laser, generating 4-µJ, 170-fs pulses at 250 kHz repetition rate. A fraction of the beam is used to generate a white-light seed in a 3-mm-thick sapphire plate, while the remaining part is frequency

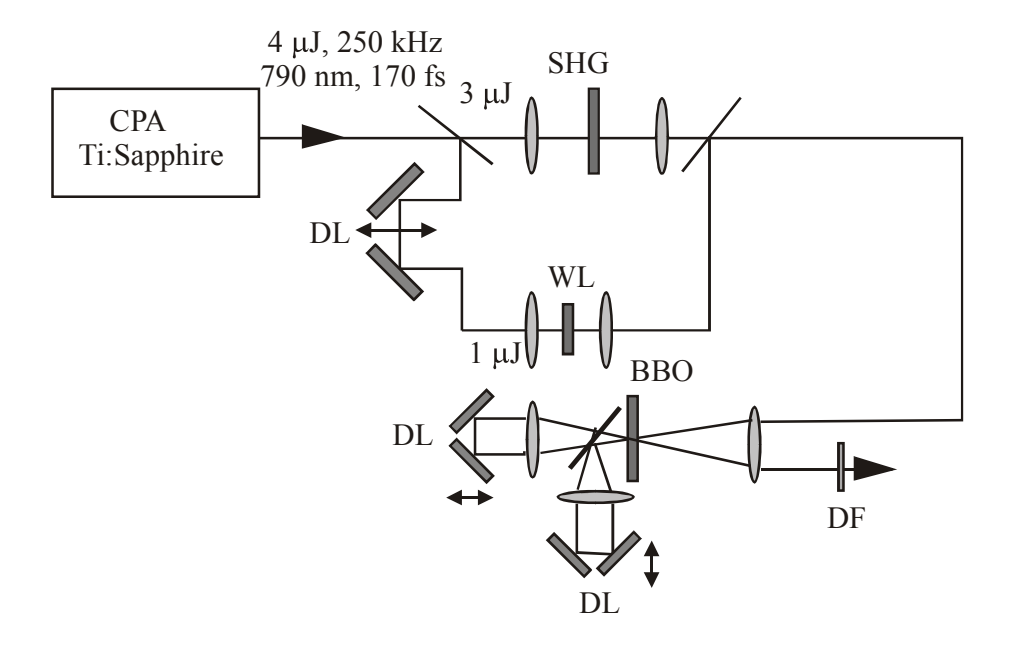


FIG. 1.12. Scheme of a visible OPA. DL: delay lines; WL: white light generation stage; SHG: second harmonic generation stage; DF: dichroic filter.

doubled in a BBO crystal to give 1 µJ of energy at 0.4 µm; the pump and seed beams are then combined by a dichroic mirror and their path lengths are matched by a suitable delay line. The two pulses are then focused on a 1-mm-thick BBO OPA crystal, cut for type-I phase matching; the crystal thickness is close to the pump \in signal pulse splitting length for BBO in the visible (see Fig. 1.6). The white-light seed component to be amplified is selected by simply rotating the BBO crystal and re-optimizing the pump-seed delay in order to compensate for the group velocity dispersion in the continuum. Given the small crystal thickness, high pump intensities are required to achieve high parametric gain; in this design, intensities lower than 50 GW/cm<sup>2</sup> are used to avoid the onset of self-focusing effects in the BBO crystal. Typical single-pass gains in this system are in the order of 100. The BBO crystal is placed after the focus of the lens, i.e. in a diverging beam. This technique makes it possible to prevent self-focusing and use higher intensities than would be possible by just putting the crystal at the focus of a longer-focal-length lens. After the first pass, pump and signal beams are separated by a dichroic beam splitter, and then reflected back into the BBO OPA crystal for a second amplification pass. Two passes in the crystal, instead of a single pass in a crystal of double length, are required to compensate for the GVM effects by suitably adjusting the delays. Typical gains in the

second pass are around 10, giving signal energies of ≈ 150 nJ, which represent a 15% conversion efficiency of the pump pulse energy. After amplification, the signal beam is collimated and separated from the remaining pump and idler beams by dichroic reflectors. The amplified pulses are tunable, in the visible, from 0.47 µm to beyond 0.7 um; they display excellent spatial quality peak-to-peak noise (less than 5% across the entire tuning range). Because of type I phase matching, the amplified pulse bandwidth strongly depends on signal wavelength (see Fig. 1.10), increasing in the red as degeneracy is approached. The pulses generated by the OPA are not transform-limited, but are frequency chirped by the white-light generation process and by Group Velocity Dispersion (GVD) in the optics and the BBO crystal. This chirp can be removed with a prism compressor and TL pulses are generated, with duration ranging from 80 fs in the blue to less than 30 fs in the red; note that the OPA generates pulses that are considerably shorter than the pump pulses. The limitation in achievable pulsewidth is set by the relatively narrow phase matching bandwidths available in a collinear interaction geometry. A possible solution to this problem consists of changing the phase-matching angle in the subsequent amplification stage, so as to amplify at each pass a different spectral region of the white light; this technique makes it possible to generate 30-fs pulses tuneable throughout the visible.

#### 1.4 Ultrabroadband Visible Optical Parametric Amplifier

A more effective solution to the aforementioned problem will be discussed in the following. We will report on an optical parametric amplifier scheme which overcome the pulsewidth limitation due to the narrow phase matching bandwidths and generate few-optical-cycle pulses with μJ-level energy in the visible. Relatively long pump pulses (≈100 fs) are used and the properties of non-collinear phase matching are exploited to achieve broadband amplification of the white light seed; the amplified pulses are then compressed to sub-10-fs duration using suitable dispersive delay lines.

#### 1.4.1 Noncollinear Visible Optical Parametric Amplifier

In an OPA using a collinear interaction geometry, the propagation direction in the nonlinear crystal is selected to satisfy, for a given signal wavelength, the phase-matching condition  $\Delta k = 0$ . In this condition the signal and idler group velocities are fixed and so the phase matching bandwidth of the process (see Eq. 24). An additional degree of freedom can be introduced using a non-collinear geometry, such as that shown in Fig. 1.13(a): pump and signal wave-vectors form an angle  $\alpha$  (independent of signal wavelength) and the idler is emitted at an angle  $\Omega$  with respect to the signal. In this case the phase matching condition becomes a vector equation, which, projected on directions parallel and perpendicular to the signal wave-vector, becomes

$$\Delta k_{\text{par}} = k_{\text{n}} \cos \alpha - k_{\text{s}} - k_{\text{i}} \cos \Omega = 0, \qquad (26a)$$

$$\Delta k_{perp} = k_p \sin \alpha - k_i \sin \Omega = 0.$$
 (26b)

Note that the angle  $\Omega$  is not fixed, but depends on the signal wavelength. If the signal frequency increases by  $\Delta\omega$ , the idler frequency decreases by  $\Delta\omega$  and the wavevector mismatches along the two directions can be approximated, to the first order, as

$$\Delta k_{par} \cong -\frac{\partial k_{s}}{\partial \omega_{s}} \Delta \omega + \frac{\partial k_{i}}{\partial \omega_{i}} \cos \Omega \Delta \omega - k_{i} \sin \Omega \frac{\partial \Omega}{\partial \omega_{i}} \Delta \omega , \qquad (27a)$$

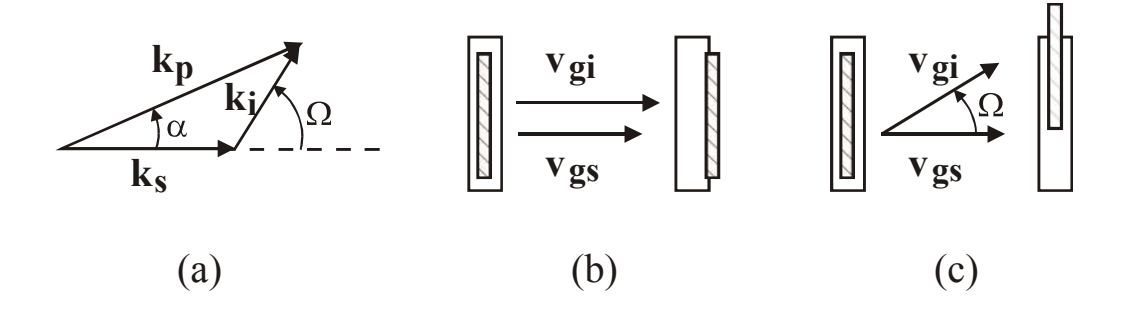


FIG. 1.13. (a) Schematic of a noncollinear interaction geometry; (b) representation of signal and idler pulses in the case of collinear interaction; (c) same as (b) for noncollinear interaction.

$$\Delta k_{perp} \cong \frac{\partial k_{i}}{\partial \omega_{i}} \sin \Omega \, \Delta \omega + k_{i} \cos \Omega \, \frac{\partial \Omega}{\partial \omega_{i}} \, \Delta \omega \,. \tag{27b}$$

To achieve broadband phase matching, both  $\Delta k_{par}$  and  $\Delta k_{perp}$  must vanish. Upon multiplying (27a) by  $\cos\Omega$  and (27b) by  $\sin\Omega$  and adding the results, we get

$$\frac{\partial k_{i}}{\partial \omega_{i}} - \cos \Omega \frac{\partial k_{s}}{\partial \omega_{s}} = 0, \qquad (28)$$

which is equivalent to

$$v_{gs} = v_{gi} \cos \Omega. (29)$$

Eq. (29) shows that broadband phase-matching can be achieved for a signal-idler angle  $\Omega$  such that the signal group velocity equals the projection of the idler group velocity along the signal direction. This effect is shown pictorially in Fig. 1.13: for a collinear geometry (Fig. 1.13(b)), signal and idler moving with different group velocities get quickly separated giving rise to pulse lengthening and bandwidth reduction, while in the non-collinear case (Fig. 1.13(c)) the two pulses manage to stay effectively overlapped. Note that Eq. (29) can be satisfied only if  $v_{gi} > v_{gs}$ ; this is however always the case in the commonly used type I phase matching in negative uniaxial crystals, where both signal and idler see the ordinary refractive index. Eq. (29) allows to determine the signal-idler angle  $\Omega$  required for broadband phase-matching; from a practical point of view, it is more useful to know the pump-signal angle  $\alpha$ , which is given by

$$\alpha = \arcsin \left( \frac{1 - v_{gs}^2 / v_{gi}^2}{1 + 2 v_{gs} n_s \lambda_i / v_{gi} n_i \lambda_s + n_s^2 \lambda_i^2 / n_i^2 \lambda_s^2} \right)^{1/2}.$$
 (30)

As an example, in a type I BBO OPA pumped at  $\lambda_p = 0.4$  µm, for a signal wavelength  $\lambda_s = 0.6$  µm broadband phase-matching is achieved for  $\alpha \cong 3.7^{\circ}$ . To better illustrate the effect of non-collinear phase-matching, in Fig. 1.14 we plot, for a type I BBO OPA pumped at 0.4 µm, the phase matching angle  $\theta_m$  as a function of signal wavelength for different values of pump-signal angle  $\alpha$ . For a collinear configuration ( $\alpha = 0^{\circ}$ )  $\theta_m$  shows a strong dependence on the signal wavelength so that, for a fixed crystal orientation, phase-matching can be achieved only over a narrow signal frequency range.

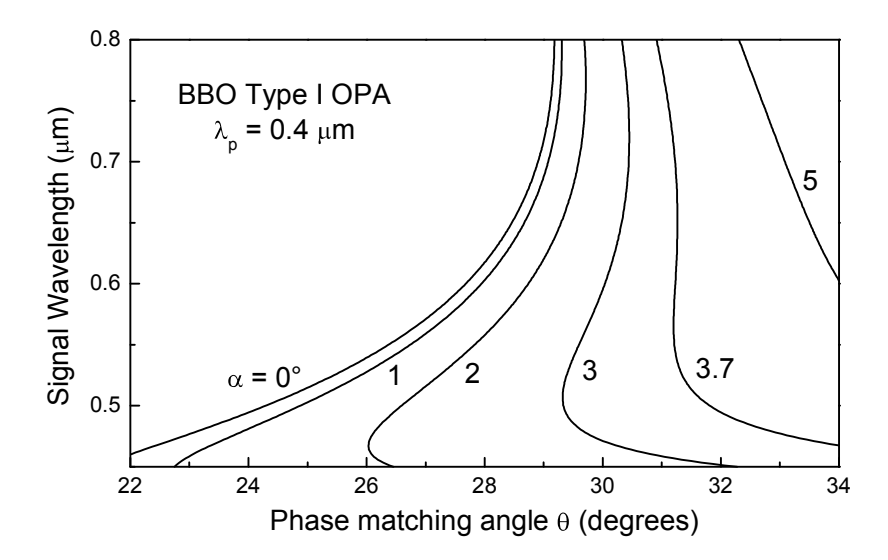


FIG. 1.14. Phase-matching curves for a noncollinear type I BBO OPA pumped at 0.4  $\mu$ m, as a function of the pump-signal angle  $\alpha$ .

By going to a non-collinear configuration and increasing  $\alpha$ , the wavelength dependence of  $\theta_m$  becomes progressively weaker until, for the optimum value  $\alpha = 3.82^{\circ}$ , a given crystal orientation ( $\theta \cong 32^{\circ}$ ) allows to achieve simultaneously phase matching over an ultrabroad bandwidth, extending from 0.5 to 0.75  $\mu$ m. Note that, in this configuration, the symmetry between signal and idler is lost, because they propagate at different angles.

#### 1.4.2 Experimental Setup

This favourable property of the non-collinear geometry for broadband parametric amplification was first recognized by Gale *et al.* [Driscoll et al., 1994; Gale et al., 1995, 1998a, 1998b] and was exploited to build broadband OPOs generating pulses as short as 13 fs; more recently, the same concept was extended by several research groups to OPAs seeded by the white-light continuum [Wilhelm et al., 1997; Cerullo et al., 1997, 1998, 1999, 2000; Shirakawa and Kobayashi, 1998a, 1998b; Shirakawa et al., 1998c, 1999; Kobayashi and Shirakawa, 2000; Riedle et al., 2000; Zavelani-Rossi et al., 2001]. A schematic of the experimental set up of the non-collinear OPA used in our experiments is shown in Fig. 1.15 [Cerullo et al., 1997, 1998, 1999, 2000]. Briefly, it starts from an amplified Ti:sapphire laser (Clark-MXR model CPA-1) producing 150-fs pulses at

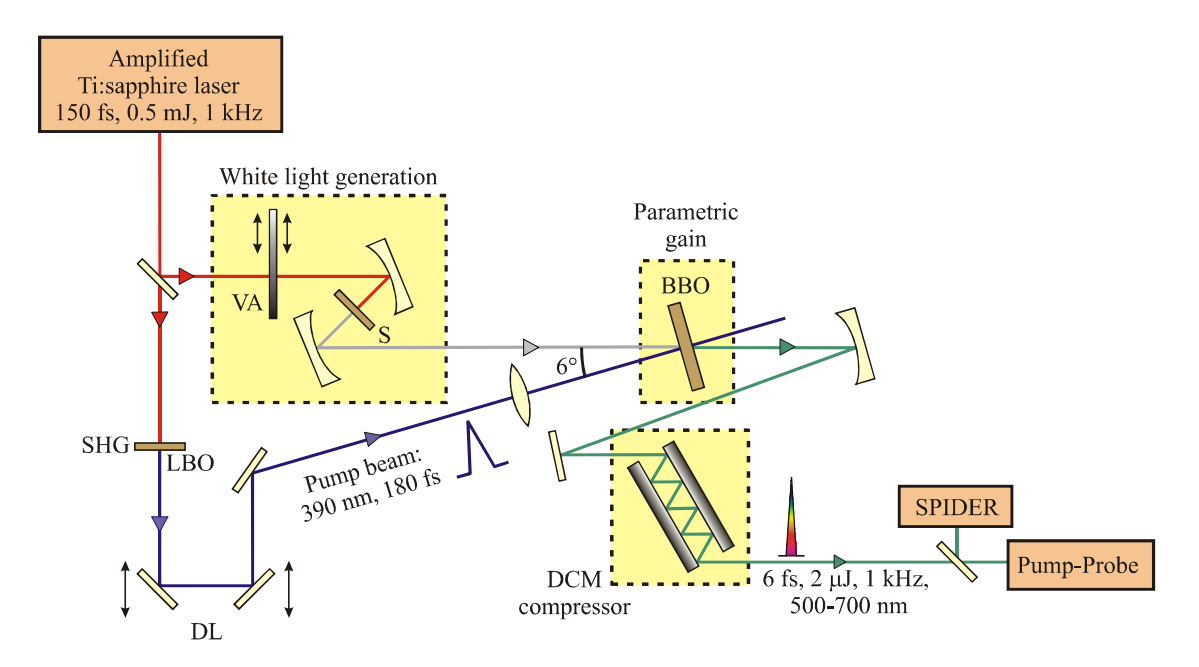


FIG. 1.15. Schematic of the noncollinear OPA and the pulse compressor: BS, beam splitter; SHG, second-harmonic generator; LBO, lithium triborate crystal; DL, delay line; L, spherical lens; VA, variable attenuator; M, spherical mirrors; S, 1-mm-thick sapphire plate; SF, short-pass filter; BBO, β-barium borate crystal; DCMs, double-chirped mirrors.

780 nm and 1-kHz repetition rate with energy up to 750  $\mu$ J. The pump pulses for the OPA (390 nm wavelength, 10  $\mu$ J energy, ≈180 fs duration) are obtained by frequency doubling a major fraction of the light in a 1-mm-thick lithium triborate crystal. We produce the seed pulses by white continuum generation obtained focusing a small fraction (1-2  $\mu$ J) of the remaining 780-nm beam light in a 1-mm-thick sapphire plate. By carefully controlling the energy incident on the plate (using a variable-optical-density attenuator) and the position of the plate around the focus, a highly stable single-filament white light continuum is generated. We use, for the plate, the minimum thickness allowing for stable white light generation in order to minimize the Group Delay (GD)  $\tau_g$  of the seed pulse, defined as the first derivative of the spectral phase  $\phi_{\omega}$  with respect to the frequency  $\omega$ :  $\tau_g(\omega) = \frac{d\phi_{\omega}}{d\omega}$ . Parametric gain is obtained in a single pass through a 1-mm-thick  $\beta$ -barium borate (BBO) crystal, cut at  $\theta = 32^{\circ}$ , by use of type I phase matching, with a pump-seed angle of  $\alpha$ =3.82°. Note that, due to Snell refraction, this (internal) angle corresponds to an external pump-seed angle of  $\alpha$   $\cong$  6.4°. This angle is suggested by

the appearance of a strong superfluorescence ring when the 390-nm pump is focused normally to the crystal. This ring is due to the parametric amplification of the visible portion of background noise, and its reduced thickness hints the broadband acceptance of the crystal over a narrow angle.

The alignment requires to spatially overlap the white-light seed with the blue pump on the crystal and with the superfluorescence ring in the far field. Both the pump and the signal should be focused some millimiters before the crystal: this prevents a detrimental pulse breaking of the pump during its propagation, and the amplified beam will be generated with a better spatial profile. When pump and signal are spatially and temporally overlapped and the interaction takes place, the superfluorescence ring vanishes, thus conveying a strong depletion of the pump beam due to the high efficiency of the process.

Let's now discuss the two possible configurations of the crystal optical axis with respect to the signal, shown in Fig. 1.16. The phase-matching condition  $\theta_m$  refers to the

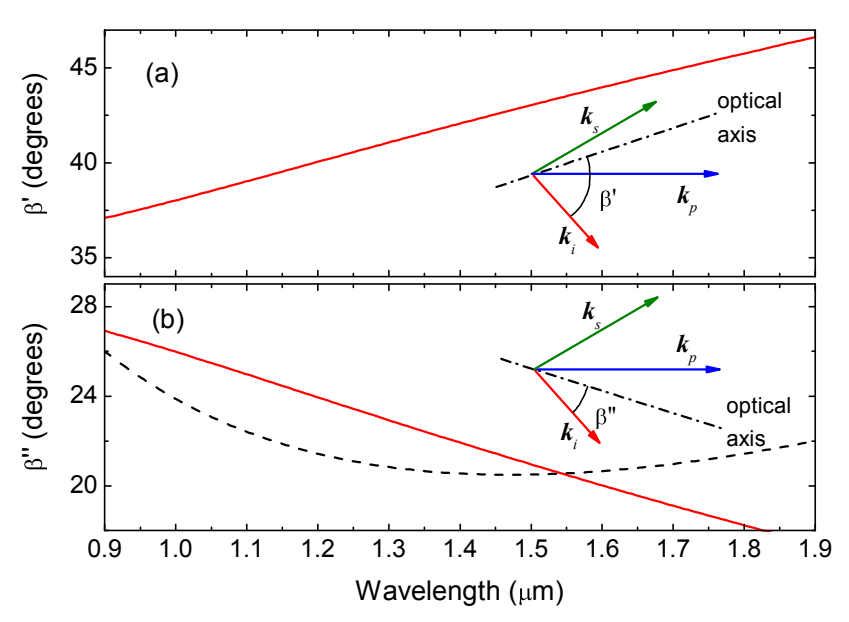


FIG. 1.16. Red solid lines: plots of the resulting angle between the optical axis of a BBO crystal and the idler wavevector at the exit of a non-collinear optical parametric amplifier (type I) pumped at  $\lambda$ =390 nm, as a function of idler wavelength, when the optical axis is placed close to the signal wavevector (a) or to the idler wavevector (b), as indicated by the corresponding schemes. Black dashed line in (b) correspond to the phase-matching angle for Second Harmonic generation in the near infrared.

angle between the optical axis and the extraordinary pump only, while the ordinary signal can be sent either in the direction suggested in panel (a) or in the one of panel (b). Both convey the same phase-matching, except for the fact that the idler propagates at different angles with respect to the optical axis, as indicated by the two solid lines. On the same graph we indicated (dashed line) the angle at which an IR signal as the idler should see the optical axis to fulfil the Second Harmonic phase-matching condition. The comparison between these curves suggests that configuration (b) favours the frequency doubling of the idler; the presence of a clean, broadly coloured rainbow in the far field conveys a first order hint on the spectral and spatial good quality of the amplified beam, even though this effect slightly reduces the efficiency of the OPG process.

The chosen crystal length is close to the pulse-splitting length for signal and pump in the wavelength range of interest. The white light seed is imaged into the BBO crystal by spherical mirror  $M_2$  (see Fig. 1.15), with a spot size nearly matching that of the pump beam. Pump intensities of  $\approx 120~\text{GW/cm}^2$  are used; at higher intensities distortion and beam break-up due to higher order nonlinear effects in the BBO crystal are observed. The amplified pulses have  $\approx 2~\mu\text{J}$  energy, peak-to-peak fluctuation of less than 7%, and maintain a good TEM<sub>00</sub> beam quality. The white light seed and the amplified beam are guided by only reflective optics to avoid the introduction of additional chirp. After the gain stage the amplified pulses are collimated by the spherical mirror  $M_3$  and sent to the compressor.

#### 1.4.3 Results: amplified bandwidth and chirp

The OPA pulse bandwidth strongly depends on the system alignment and on the chirp of the white-light seed. Optimum alignment is achieved by adjusting the pump-seed angle to match the apex angle of the strong superfluorescence cone emitted by the BBO crystal when illuminated by the pump pulse [Danielius et al., 1996]; under these conditions, the spectrum of the amplified beam extends from 500 to 750 nm (blue line in Fig. 1.17(a)), with a FWHM bandwidth of 180 THz, and is virtually not tunable, since it covers the maximum available gain bandwidth. Narrower gain bandwidths, which may be required for some experiments, can be simply achieved by detuning the pump-seed angle

from the optimum value and/or deliberately increasing the white light chirp: in this case, the OPA can be tuned by slightly tilting the BBO crystal and/or varying the pump-seed delay. A typical sequence of amplified pulse spectra obtained under these conditions is shown in Fig. 1.17(b). For reasons to be discussed later, in the experiments here reported we suppressed part of the non-collinear OPA spectrum on the low frequency side by inserting a thin short-pass glass filter into the seed beam path. A typical spectrum thus obtained is shown in Fig. 1.17(a) as a black hashed area.

The pulses emerging from the OPA are strongly chirped; before designing the compressor, we first carefully characterized their GD. The experimental setup of the apparatus we used is shown in Fig. 1.18. An interference filter with 10-nm bandwidth selects a spectral slice of part of the non-collinear OPA pulses, producing ≈70-fs gate pulses. These pulses and the broadband OPA pulses are cross-correlated in a 20-µm-thick BBO crystal. After the crystal an UV monochromator selects the single frequencies of the upconverted signal allowing us to determine the relative arrival times of the different frequency components of the OPA pulse. The results of the measurement are shown in Fig. 1.19 as diamonds: an overall group delay of ≈400 fs between the extreme parts of the amplified pulse is measured. The experimental data can be accurately reproduced by an

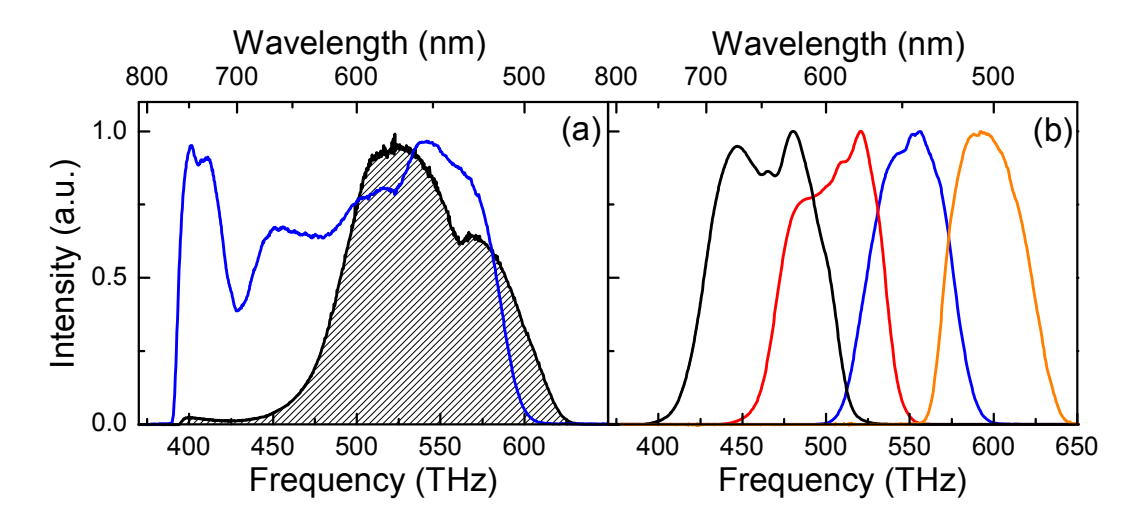


FIG. 1.17. (a) Non-collinear OPA spectrum with full-bandwidth operation (blue line) and with a short-pass filter on the seed beam (black hashed area); (b) Typical sequence of NOPA amplified pulse spectra with narrower gain bandwidths, achieved by detuning the pump-seed angle from the optimum.

independent calculation of the GD. The calculation takes into account the group delays introduced by the different optical elements (sapphire plate, BBO crystal, beam splitters and ≈3.5 m air path). The measured GD vs. frequency dependence notably deviates from a linear behaviour due to higher order dispersion.

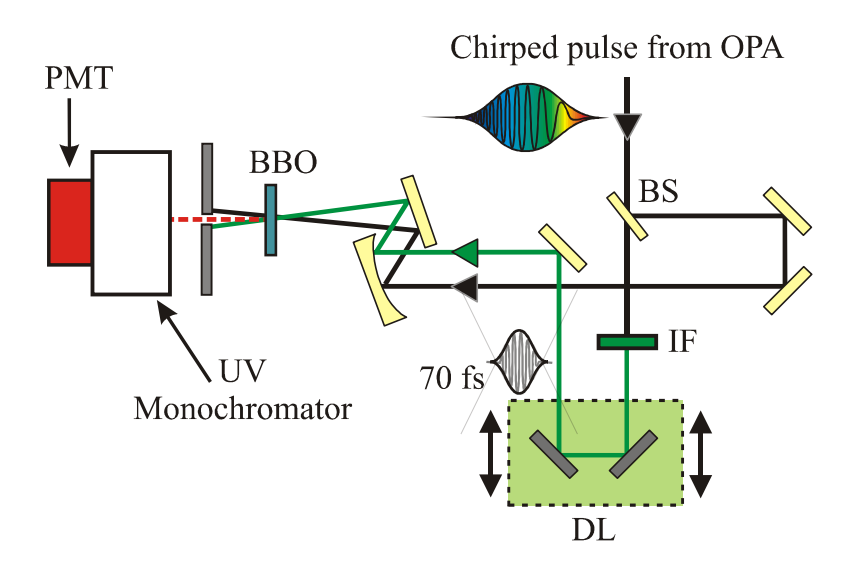


FIG 1.18. Schematic of the setup used for measuring the group delay of the amplified pulses: PMT, photomultiplier; BBO,  $\beta$ -barium borate crystal; BS, beam splitter; IF, interference filter (10-nm bandwidth); DL, delay line.

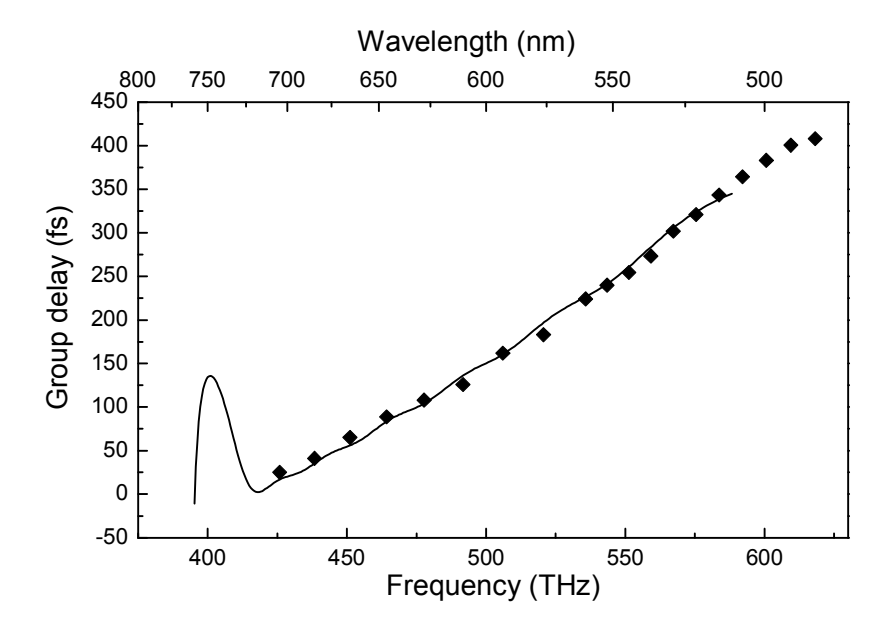


FIG. 1.19. Diamonds, measured GD of the non-collinear OPA pulses before compression; solid line: GD (with reversed sign) after 10 bounces on the DCMs.

#### 1.5 Pulse compression using double-chirped mirrors

The OPA generates pulses with very broad bandwidths and thus potentially very short. In order to obtain the minimum pulse duration compatible with their bandwidth (the so-called transform-limited duration), however, delay lines with dispersion characteristics accurately controlled over such broad bandwidths are needed. Different approaches have been proposed. Standard Brewster-cut prism pairs can be used to compress the narrower bandwidth pulses down to a duration of 10-15 fs [Wilhelm et al., 1997; Cerullo et al., 1997; Shirakawa and Kobayashi, 1998a, 1998b]; for broader bandwidths, thin prism sequences [Cerullo et al., 1998], prism-grating [Shirakawa et al., 1998c] and prism-chirped mirror combinations [Shirakawa et al., 1999] or adaptive pulse compressors [Baltuska et al., 2002a] were used. These systems show different performance in terms of corrected bandwidth and energy throughput. The shortest pulses generated by the OPA were obtained by a prism-chirped mirror combination and have a nearly Transform Limited (TL) duration of 4.4 fs [Shirakawa et al., 1999]. Note the dramatic shortening of the pulsewidths with respect to the pump pulse duration, which is in the 100-fs range. As a matter of fact, using short pump pulses does not help in getting shorter pulses from the OPA, but on the contrary could be detrimental to the broadband amplification process, because of the reduced temporal overlap between the pump pulses and the chirped white light seed.

Chirped mirrors are often used in conjunction with other dispersive elements, such as prism or grating pairs, to achieve the desired phase characteristics; these additional elements, however, increase the complexity of the system, making it bulky and more sensitive to alignment. A simple and experimentally convenient compressor design employs exclusively chirped dielectric mirrors [Szipöcs et al., 1994; Kärtner et al., 1997], with dispersion characteristics tailored to compensate for the OPA GD: this approach, besides the high energy throughput and the broadband phase correction, greatly simplifies the system design, allowing for compactness, reproducibility and insensitivity to misalignment which are of great importance in practical applications [Cerullo et al., 2000; Zavelani-Rossi et al., 2001]. Chirped dielectric mirrors introduce a frequency-

dependent GD by reflecting different frequency components of the incident radiation at different positions within the multilayer structure. This dispersion management strategy was previously applied to laser oscillators [Stingl et al., 1994], optical parametric oscillators [Hebling et al., 1995] and extracavity pulse compressors [Sartania et al., 1997].

The simplest type of chirped mirrors is composed of alternating quarter-wave layers of high and low refractive index materials, in which the Bragg wavelength is varied from layer pair to layer pair, such that long wavelengths are made to penetrate deeper into the mirror structure than short ones. Such mirrors introduce a negative Group-Delay Dispersion (GDD), defined as the second derivative of the spectral phase  $\phi_{\omega}$  with respect to the frequency  $\omega$ : GDD =  $\left(\frac{d^2\phi_{\omega}}{d\omega^2}\right)$ . Additionally, they exhibit a broader high-reflectance

range compared to standard quarter-wave Bragg mirrors. The main problem in chirped mirrors is avoiding interference between reflections from the front section and the back of the mirror, which create an effective Gires-Tournois interferometer introducing large unwanted oscillations of the GD with wavelength. These dispersion oscillations can only be reduced by time-consuming computer optimization.

It has been shown [Kärtner et al., 1997] that the coupled-mode equations describing a Bragg mirror are equivalent to describing voltage and current of a microwave transmission line. In this picture any impedance discontinuity in the transmission line causes a spurious reflection, giving rise to dispersion oscillations. Adiabatic matching of the impedance suits to suppress this problem. Matching is achieved by a sufficiently slow increase of the coupling coefficient in the front section of the mirror, i.e. an additional chirp in the optical thickness ratio of high-index and low-index layer. The resulting structure is called a Double-Chirped Mirror (DCM), as it combines the chirp of the Bragg wavelength and that of the layer duty cycle. Matching within the layer stack only provides a partial solution to the problem. It has to be combined with an additional matching section to the impedance of the ambient medium on top of the DCM structure. For this purpose, an antireflection coating is typically deposited on top of the chirped mirror. This concept allows achieving highly controlled dispersion characteristics over

bandwidths approaching 200 THz. A bandwidth limitation, however, is imposed by the broadband antireflection coating matching the coating to the ambient medium (air).

Using the DCM concept we designed mirrors with the following properties: (a) high reflectivity in the OPA wavelength range, (b) incorporation of a long-wavelength transmission window to suppress the remaining fundamental wavelength component of the seed pulse, and (c) a GDD vs. frequency characteristics that allows compensating, in a finite number of bounces, for the OPA dispersion. The main contributions to the OPA dispersion are 1 mm of sapphire, 1 mm of BBO, and the air path of the set-up. The chirped mirrors consist of 30 pairs of alternating  $SiO_2/TiO_2$  layers and were manufactured by ion beam sputtering which, together with on-line optical monitoring during the process, gives very reproducible results. We estimate a layer deposition accuracy of  $\approx 0.2$  nm (rms). As shown in Fig. 1.20 (dashed line), the mirrors display a high reflectivity larger than 99.8% in the 480–750 nm spectral range. The designed GDD of the mirrors (solid line in Fig. 1.20) is negative over the 510–710 nm wavelength range and oscillates around the desired value (dotted line in Fig. 1.20) with an  $\approx 8-9$  fs<sup>2</sup> oscillation amplitude. In the group delay picture, the dispersion oscillations translate into

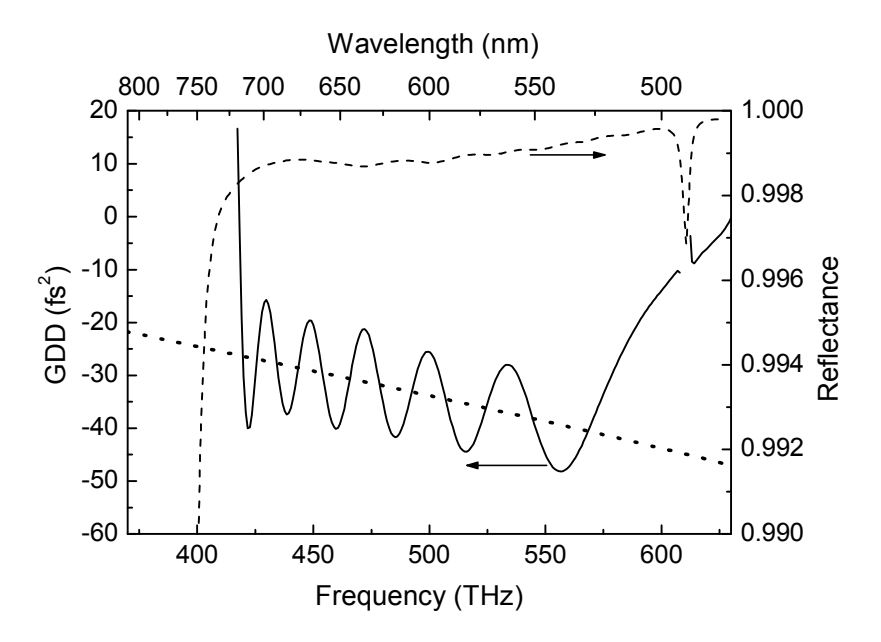


FIG. 1.20. Reflectivity of the DCM (dashed line), designed (solid line) and desired (dotted line) GDDs of the DCM.

only 0.15-fs (rms) deviations from the designed value (solid line in Fig. 1.21). This makes it clear that such small residual dispersion oscillations, which are ultimately unavoidable even with the DCM concept and subsequent computer optimization, cause only negligible deterioration of the pulse quality. The dispersion compensation range is further limited by the roll-on of the incorporated filter at 780 nm, which introduces phase distortions at above 720 nm. For this reason we are unable to compress the OPA pulse under full-bandwidth operation (blue solid line in Fig. 17(a)) and must introduce a thin colour glass filter on the seed beam to suppress part of the red spectrum in the amplified pulses.

Figure 1.21 shows the calculated GD of the mirrors as a solid line. We can see that the GDD oscillations are averaged out by integration and the GD displays a smooth frequency dependence with very low residual dispersion oscillations. Diamonds indicate measurements of the GD of the manufactured mirrors as measured by a white-light interferometry [Naganuma et al., 1990]. Within the accuracy of these measurements, the experimental data fits well to the designed values. For a more illustrative image of the DCM properties, Fig. 1.22 shows the calculated standing-wave intensity distribution inside the DCM coating. It can be clearly seen that longer wavelengths penetrate deeper

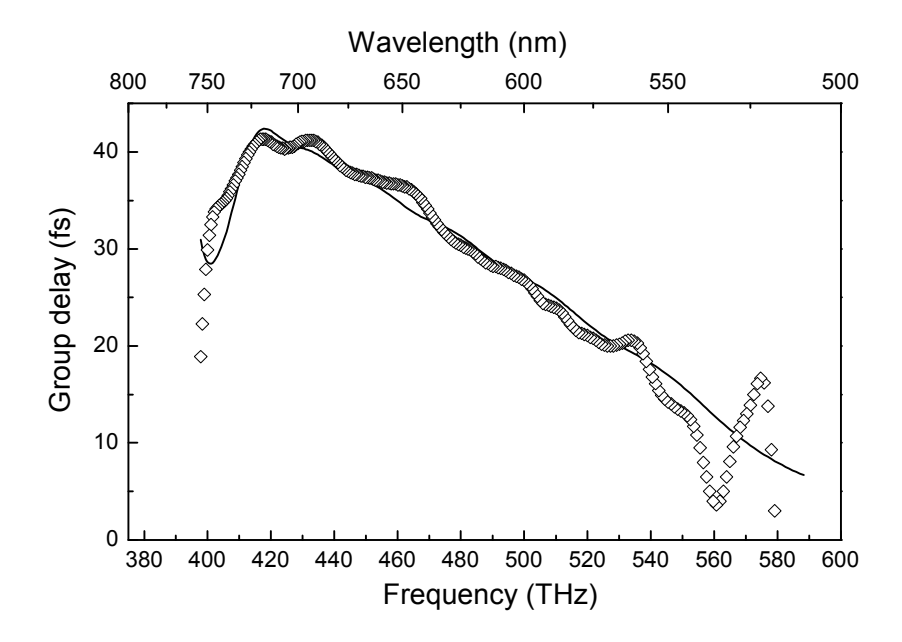


FIG. 1.21. Calculated (solid curve) and measured (diamonds) group delays introduced by the DCMs.

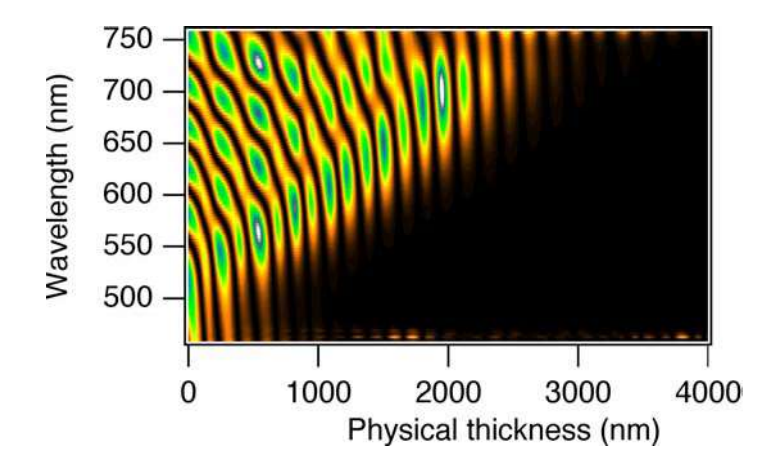


FIG. 1.22. Normalized standing wave intensity distribution inside the DCM vs. wavelength. The dispersion of the mirrors is clearly illustrated by the dependence of penetration depth on wavelength.

into the mirror structure and therefore experience a larger group delay upon reflection.

As a final check we included as a solid line in Fig. 1.19 the GD introduced by 10 bounces on the DCMs multiplied by -1. Again, we can see that the GD of the manufactured mirrors matches the OPA GD very accurately over the wavelength range from 510 to 710 nm, with an rms error of 1.8 fs. These DCMs allow for a compact and reproducible compressor for the OPA pulses, without any need for additional prism or grating sequences.

### 1.6 Cross-correlation SPIDER characterization of the compressed OPA pulses

#### 1.6.1 Introduction

The characterization of ultrabroadband pulses with duration in the sub-10-fs regime is a crucial point. Traditional autocorrelation techniques, which require an *a priori* knowledge of the pulse shape, provide only rough estimates of the pulse duration. An accurate pulse characterization requires a full knowledge of the amplitude and phase of the pulse, and ideally (though less commonly in practice) knowledge of the variations of

the parameters across the pulse profile. To this purpose, several methods have been proposed, among which the most popular are: (i) Frequency-Resolved Optical Gating (FROG), which measures amplitude and phase in the time-frequency domain [Kane and Trebino, 1993; Trebino et al., 1997]; (ii) Spectral Phase Interferometry for Direct Electric-field Reconstruction (SPIDER) [Iaconis and Walmsley, 1998, 1999], which retrieves the pulse spectral phase and obtains a time-domain reconstruction of the pulse by combining it to a separate spectral amplitude measurement from a spectrometer. These techniques have been prevalently employed with near-infrared pulses and their extension to the visible spectral range, especially with very short pulses, is not straightforward.

#### 1.6.2 Theory of SPIDER

To fully characterize the compressed pulses in amplitude and phase, we use the SPIDER technique. This technique extracts the spectral phase of the pulse from an interferogram obtained from the interference of two spectrally sheared replicas of the pulse to be characterized. Measurement of the spectral phase can be combined with measurement of a power spectrum of the fundamental. The combined spectral amplitude and phase information then gives access to the complex electric field of the optical pulse  $E(\omega) = |E(\omega)| \exp[j\phi(\omega)]$  in the frequency domain. An inverse Fourier transform then returns the temporal amplitude and phase of the pulse.

SPIDER is a self-referencing interferometric technique, i.e. there is no need for a well-characterized reference. It is an intrinsically fast technique and has been demonstrated for real-time single-shot characterization of a 10-Hz amplifier system [Dorrer et al., 1999] and with refresh rates as high as 20 Hz [Shuman et al., 1999]. When applied to ultrabroadband pulses, SPIDER has several advantages with respect to other pulse characterization techniques. In particular, the accuracy of spectral phase reconstruction is widely insensitive to the phase-matching bandwidth of the upconversion crystal and the spectral responsivity of the detector, since it depends only on the fringe spacing. In addition, there is a direct, non-iterative phase retrieval algorithm and no moving parts in the apparatus.

To retrieve the spectral phase, two replicas of the pulse to be characterized are shifted in frequency by a spectral shear  $\Omega$  and delayed in time by  $\tau$ . The resulting spectral interference pattern they generate is:

$$S(\omega) = |E(\omega)|^2 + |E(\omega + \Omega)|^2 + 2|E(\omega)E(\omega + \Omega)| \cdot \cos[\phi_{\omega}(\omega + \Omega) - \phi_{\omega}(\omega) + \omega\tau], \quad (31)$$

where  $\phi(\omega)$  is the spectral phase of the input pulse. This interferogram can be easily recorded by an integrating spectrometer. The cosine term of (31) contains all the spectral phase information we need and it is responsible for the fringes of the interferogram. The argument of the cosine can be extracted from (31) by straightforward Fourier transform and filtering operations [Takeda et al., 1982]. Note that information on the amplitudes of the interferogram is at no point required for analysis of the data. The constant delay  $\tau$  is determined by separate spectral interferometry of the two pulse replicas. After subtraction of the linear phase term  $\omega \tau$ , one is left with the phase difference  $\phi(\omega + \Omega) - \phi(\omega)$ , from which the spectral phase is extracted by integration.

The spectral shear  $\Omega$  is generated by up-converting two replicas of the pulse with a strongly stretched pulse using sum-frequency generation in a nonlinear optical crystal. The upconverter pulse has to be stretched such that its instantaneous frequency can be considered constant for the duration of the pulse to be measured. The interferogram is then obtained between the two up-converted pulses, which are exact, but frequency-shifted, replicas of the pulse to be characterized.

#### 1.6.3 SPIDER for visible pulses

The extension of this technique to the visible spectral range with ultrabroadband pulses is not straightforward and requires a careful design of the setup. The SPIDER apparatus used in this work is shown in Fig. 1.23. We employ a novel cross-correlation variant of the SPIDER technique, that derives the reference pulse from the infrared pump laser ( $\lambda = 780$  nm) rather than from the OPA pulse to be measured. This variant has the advantage of higher signal powers and a more favorable wavelength range (300-380 nm) of the SPIDER trace. A 5-cm long SF10 glass block (GDD: 8270 fs²) is employed as stretcher, which results in a spectral shear of 5.22 THz between the up-converted

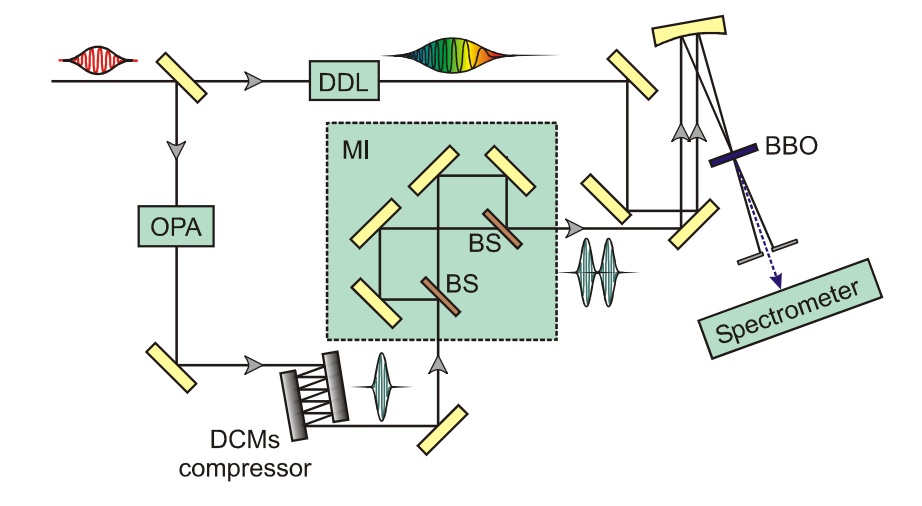


FIG. 1.23. Schematic of the SPIDER setup. OPA, optical parametric amplifier; DDL, dispersive delay line; MI, balanced Michelson interferometer; BS, 100-μm-thick Inconel-coated beam splitters.

replicas, obtained upon dividing the delay by the GDD. A balanced Michelson interferometer with 100-µm-thick Inconel-coated beam splitters is used to generate the two replicas of the non-collinear OPA pulse. These replicas are up-converted with the stretched infrared pulse in a 20-um-thick type II BBO crystal. Type II phase matching for sum-frequency generation provides a very broad bandwidth in the ordinary axis and a considerably narrower one in the extraordinary axis. We can take advantage of these properties by orienting the narrow-band pump beam along the extraordinary axis and the broadband OPA beam along the ordinary one [Gallmann et al., 1999]. The up-converted pulses are detected by a spectrograph with a 1200 groove/mm grating and a 25 µm entrance slit: this setup allows spectrally resolving the individual fringes and still covering the full bandwidth of the SPIDER interferogram. To calibrate the apparatus we separately measure the linear phase term ωτ by conventional spectral interferometry. To this purpose one could simply use the interferogram of the two OPA pulse replicas; however, due to the large difference in wavelength range with respect to the SPIDER trace, even small inaccuracies of the spectrometer wavelength calibration would lead to significant errors. Therefore we prefer to record the interferogram of the second harmonic (SH) of the replica pulses, which can be done with the same spectrograph adjustment used to acquire the SPIDER trace. Since the SH and the SPIDER interferograms are not

completely overlapped spectrally, a very accurate calibration of the spectrometer is needed to reliably extract the linear phase term. This is achieved by measuring the wavelength of 12 spectral lines of a mercury lamp in the UV spectral region.

#### 1.6.4 Results

Figure 1.24 shows the SPIDER interferogram of a typical compressed non-collinear OPA pulse [Zavelani-Rossi et al., 2001]. The time delay  $\tau$  between the two pulse replicas is 271 fs. Note that the up-converted spectrum is somewhat narrower than the OPA spectrum, due to the spectral shaping induced by the finite phase matching bandwidth of the up-conversion process. This does not cause a problem, because the SPIDER technique relies only on the fringe spacing for the reconstruction of the spectral phase and does not need the fringe amplitude information. The only effect of spectral shaping due to finite phase matching bandwidth is a reduction of the signal and the consequent deterioration of the signal-to-noise ratio. In our case, however, signal-to-noise ratio is very high even out in the tails of the SPIDER trace, so that the phase extraction is fully reliable. Using a thinner crystal would increase the phase matching bandwidth at the expense of a lower signal, so that the thickness used in this work represents an optimum

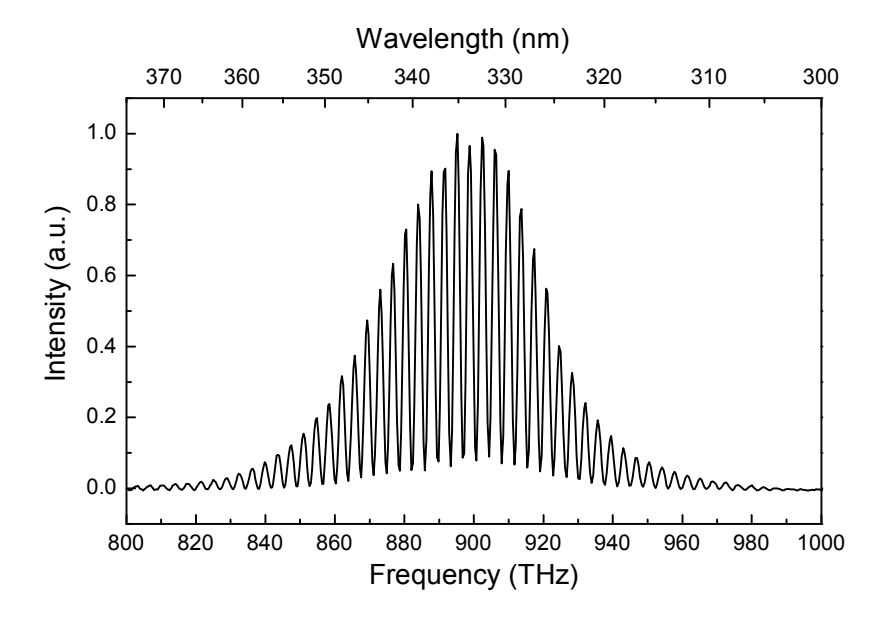


FIG. 1.24. SPIDER trace of the compressed non-collinear OPA pulse.

trade-off.

The spectral phase reconstructed from the SPIDER trace is plotted in Fig. 1.25(a) (blue solid line) together with an independently measured pulse spectrum (filled area). The measurements indicate a nearly flat spectral phase in the range from 510 to 710 nm. There are some residual dispersion oscillations, which are of comparable magnitude as those introduced by the 10 bounces on the chirped mirrors (compare Fig. 1.21). Phase distortions occur in the red for wavelengths longer than 720 nm and in the blue around 500 nm, again in agreement with the GD characteristics of the chirped mirrors. Fig. 1.25 (b) shows the reconstructed pulse temporal phase (blue solid line) and amplitude (filled area) profile. The FWHM duration of the pulse is of 5.7 fs, which is to be compared to the transform-limit of 5.2 fs. The pulse shape is remarkably clean, and nearly free of side-lobes. It is also confirmed that the dispersion oscillations of our DCMs have negligible impact on the pulse shape.

Fig. 1.26 shows the Wigner representation [Paye, 1992; Yeremenko et al., 2000] of the reconstructed pulse. The Wigner trace is a two-dimensional distribution in the time-frequency domain taking into account both temporal and spectral properties of light pulses and providing an intuitive representation of the temporal ordering of the different spectral components of the pulses. It is worth noting that all the frequency components of

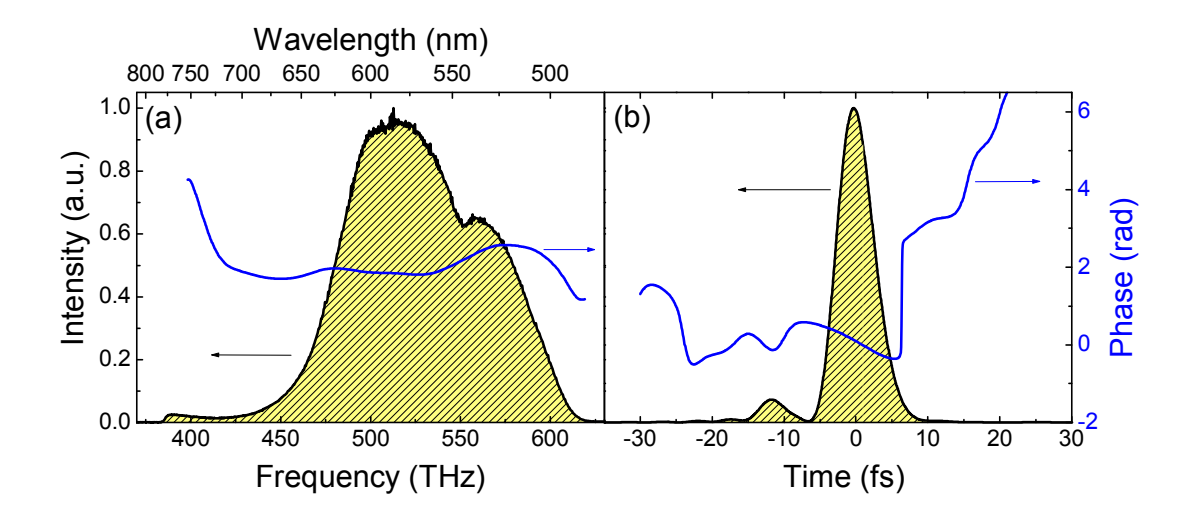


FIG. 1.25. (a) Spectral intensity (filled orange area) and reconstructed spectral phase (blue solid curve) of the compressed non-collinear OPA pulse. (b) Reconstructed temporal intensity (filled orange area) and phase (blue solid curve) of the pulse.

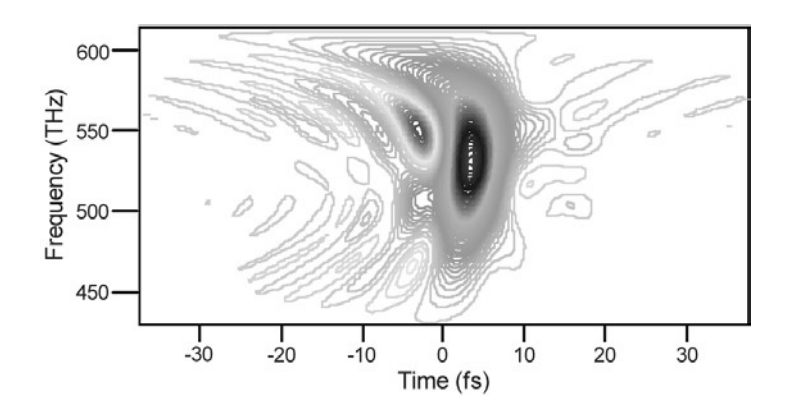


FIG. 1.26. Wigner representation of the compressed OPA pulses in the time–frequency phase space.

the compressed pulses arrive simultaneously, denoting very small phase distortions of the pulse. The SPIDER measurements allow identifying residual detrimental contributions to the spectral phase. This clearly demonstrates the advantage of using a full characterization technique over the traditional autocorrelation.

#### 1.7 Conclusions and perspectives

In this chapter we have reviewed ultrafast OPAs, showing that technology has matured, making it possible to extend considerably the tuning range of femtosecond Ti:sapphire laser systems. Some OPA designs have become standard and are even commercially available.

In particular, we showed how OPAs pumped by the SH of a Ti:sapphire laser with non-collinear geometry and proper phase matching can amplify a very broad visible bandwidth, comparable to the carrier frequency. If properly compressed, these visible pulses contain only a few carrier cycles under their envelope and have duration well below 10 fs.

We have demonstrated the possibility of engineering DCMs with custom-tailored dispersion characteristics over bandwidths of 170 THz in the visible; these mirrors are used in a prismless dispersive delay line to compress pulses from a non-collinear visible OPA to a near transform-limited duration of 5.7 fs. We have performed a complete

characterization in amplitude and phase of the compressed pulses, revealing a nearly satellite-free pulse shape with flat spectral phase over the wavelength range 510–710 nm. Such short pulses are easily reproducible on a daily basis without any need of compressor adjustment. The DCM compressor therefore considerably simplifies the use of the OPA for spectroscopy experiments with extreme time resolution over ultrabroad bandwidths.

Our measurements indicate that, despite these results, the bandwidth of the OPA process is not yet fully exploited. The amplified spectrum obtained without any spectral filtering on the white light seed, depicted in Fig. 1.17(a) as a blue solid line, corresponds to a transform-limited pulse duration of 4.2 fs; such a broad bandwidth goes beyond the capabilities of the DCMs used in this work, which introduce large phase distortions for wavelengths longer than 720 nm. A possible strategy to extend the mirror bandwidth could come from the removal of seed rejection filter at 780 nm which is incorporated in the mirror design. Performing the filtering by other means would substantially alleviate constraints on the mirror design and result in a wider bandwidth.

Ultrabroadband OPAs, also thanks to their reliability and simplicity of operation, are becoming established tools for ultrafast spectroscopy with extreme temporal resolution, as we will see in the next chapters.

#### Chapter 2

# Two-colours pump-probe system broadly tunable over the visible and near-IR with sub-20-fs resolution

#### 2.1 Introduction

Optical parametric amplifiers driven by amplified Ti:sapphire lasers, such as those described in chapter 1, are ideal tools for generating broadly tunable, high energy femtosecond pulses; in addition, they have the capability of significantly shortening the pulse duration with respect to that of the driving pulses. In this chapter we describe an extension of the previously described femtosecond OPAs both to the higher and lower photon energy range, to be used as few-optical-cycle pulse sources for pump and probe experiments.

In paragraph 2.2 we will describe experimental OPA set-ups delivering femtosecond pulses either in the visible or in the near-IR frequency range; these OPAs, together with a Second Harmonic Generation (SHG) stage and an up-conversion stage, allow to almost entirely cover the wavelength range from 300 to 1600 nm. In paragraph 2.3 we will present a complete system composed of two synchronized laser beams enabling the user to easily perform pulse duration measurement (through auto-correlation technique), system temporal-resolution and zero-time-delay retrieval (through cross-correlation technique) and one- or two-colours pump-probe spectroscopy.

### 2.2 Generation of femtosecond pulses from the infrared to the ultraviolet wavelength region

#### 2.2.1 System layout and design considerations

We designed an experimental set-up which could enable us to easily change both the pump wavelength, in order to excite samples which absorb in the 300-nm to 1600-nm wavelength range, and the probe wavelength, in order to observe the temporal evolution of many different transitions from the visible to the NIR. We took care in conceiving a flexible system, to be able to rapidly change duration and spectra of the pulses without the need of complicated and time-consuming realignment procedures.

Broad-band, visible ultrashort pulses generated by the non-collinear Optical Parametric Amplifier (OPA) described in chapter 1 will be used, as we will show in chapters 3 and 4, in ultrafast pump-probe spectroscopy experiments, where broad-band probes are required in order to access many different spectral features of the sample molecule. At the same time, though, such experiments need an as-monochromatic-aspossible pump pulse, eventually broadly tunable, to be resonant with just one transition at a time. A trade-off between time resolution (requiring large pulse bandwidth) and spectral selectivity (requiring small frequency content) is found at ≈30-THz bandwidth, corresponding to 15–20-fs duration. For this purpose, we designed a second, narrowband, tunable OPA, to be used as a pump pulse source. In order to narrow the amplification bandwidth, we alter the phase-matching condition of the amplifying BBO crystal, thus narrowing its bandwidth acceptance.

In Fig. 2.1(a) we show the phase matching angle for  $\lambda$  = 390 nm pump wavelength, as a function of signal wavelength in BBO crystal. As we already shown in Fig. 1.14 and described in paragraph 1.4.1, for the pump/signal angle  $\alpha$  = 3.82° (blue dash-dotted line), a given crystal orientation ( $\theta \cong 32^{\circ}$ ) allows to simultaneously achieve phase matching over an ultrabroad bandwidth, extending from 500 nm to 750 nm. By changing the angle between pump and signal in the crystal to a compromised medium-bandwidth condition

 $\alpha = 2.46^{\circ}$  (black solid line), and accordingly cutting the crystal at  $\theta = 30^{\circ}$ , it is possible to amplify light only around specific wavelengths, tuned by simply tilting the crystal.

The same experimental set-up can be also employed to obtain broadband, amplified pulses in the NIR spectral range. In this case, however, the idler lays at wavelengths shorter than 780 nm and the signal, so that  $v_{gi} < v_{gs}$ . As a consequence, as we described in paragraph 1.4.1 and illustrated in Fig. 1.14, the broad-band non-collinear amplification scheme cannot be used and the larger amplification bandwidth is achieved in collinear configuration. Nonetheless, we prefer exploiting the same non-collinear geometry ( $\alpha$ =2.46°) for two reasons: (i) it's easier to spatially separate the probe beam from the pump and idler ones; (ii) it doesn't require to change the geometrical configuration when moving from the visible to the NIR OPA. As it can be seen form Fig. 2.1(b), phasematching calculations suggest that tunability is achieved from 900 nm to 1600 nm by tilting the crystal of a few degrees and correcting the delay between pump and signal. In addition, broadband amplification can be obtained around degeneracy, thus providing shorter pulses at wavelengths around 900 nm.

A schematic of the experimental apparatus we designed is drawn in figure 2.2(a). By using a total  $\approx\!200~\mu J$  pulse energy from the regeneratively-amplified mode-locked Ti:sapphire laser already described (Clark-MXR Model CPA-1), we built a spectroscopic system consisting of two independent non-collinear optical parametric amplifiers, capable of delivering ultrashort pulses from the visible (500–700 nm, see chapter 1 and paragraph 2.2.2) to the NIR (800–1600 nm, see paragraph 2.2.3). Other than the

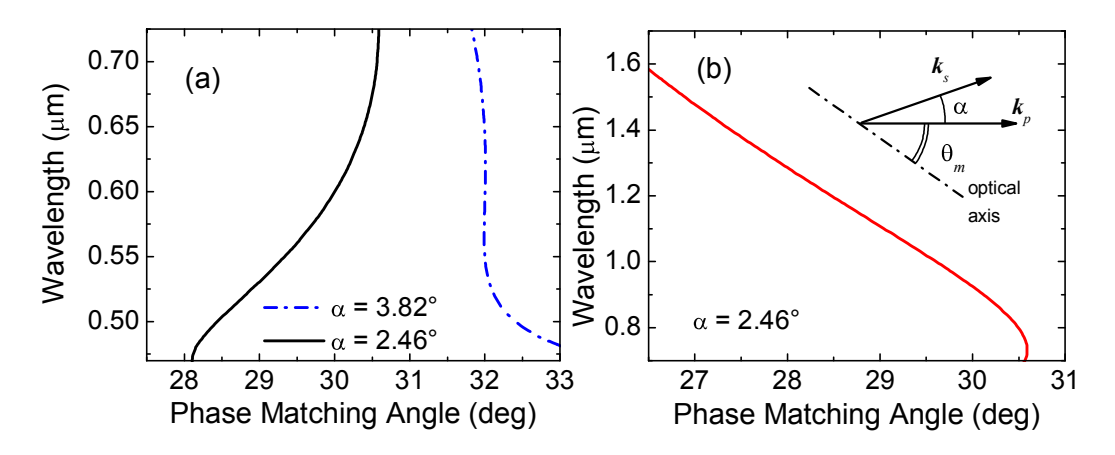


FIG 2.1. Phase-matching condition for visible (a) and Near-Infrared (b) light.

fundamental 780-nm beam, each of the two optical parametric amplifiers needs to be pumped also by some 390-nm light. This beam is generated just once in a SHG crystal (LBO, biaxial, 1-mm thickness, cut for type-I-phase-matching at  $\theta \cong 30^{\circ}$ ) and then divided into two replicas by a beam splitter, for reasons of efficiency. At the laser exit we reduce the beam diameter to  $\approx 5$  mm, so that no focussing is needed on the non-linear crystal. After blue filters (Schott BG39, 1 mm thickness) used to cut the residual FW beam, we obtain an overall SH generation efficiency of more than 20%. Blue pulses, after propagation in the SHG crystal and filters, get dispersed up to a duration of  $\approx 180$  fs and have horizontal polarisation.

Figure 2.2(b) shows the pulse compression stages and the wavelength-extension modules to the blue wavelength range (400–500 nm, achieved by frequency doubling the NIR pulses, see paragraph 2.2.4) and to the UV (320–420 nm, achieved by up-converting the visible pulses with some residual 780-nm fundamental beam, see paragraph 2.2.5). Pump and probe pulses can thus be selected among a very large variety of wavelengths and temporal durations, depending on the specific sample to be studied. The two beams accordingly chosen can have a very different path length, so that a long-range (up-to 1 meter) mechanical delay line is needed in order to synchronize the two pulses before entering the correlator, which has its own precision delay-line (see paragraph 2.3).

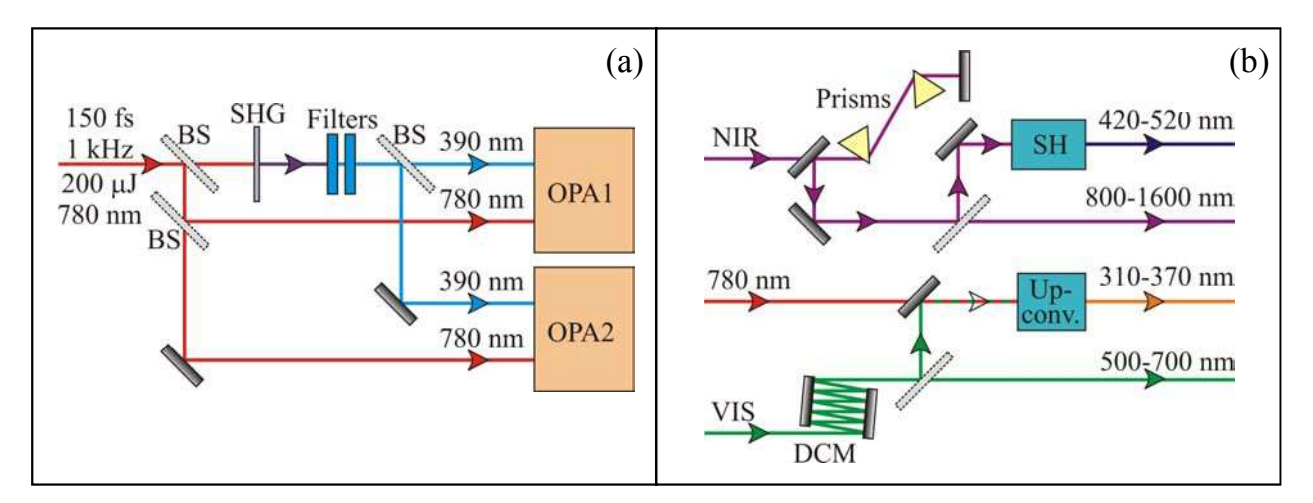


FIG 2.2. Schematic of the experimental set-up for: (a) delivering pump and signal beams to the two OPAs; (b) compressing the visible and NIR pulses from the OPAs (with Double Chirped Mirrors, *DCM*, and prisms, respectively) and extending their tunability to the blue (with a Second Harmonic stage, *SH*) and to the UV (with an up-conversion stage, *up-conv*.).

#### 2.2.2 Tunable visible non-collinear optical parametric amplifier

Narrowband tunable visible pulses can be derived from the same configuration as the one shown in chapter 1 by simply reducing the internal (external) angle between pump and signal from  $\alpha = 3.82^{\circ}$  (6.4°) to  $\alpha = 2.46^{\circ}$  (4.1°). In order to preserve the alignment of the white light and the amplified beam into the following stages, we only change the pump direction towards the crystal. Even though the tuning curves plotted in figure 2.1 suggest that the crystal should be cut at  $\theta_m = 30^{\circ}$ , reasonably good results can be obtained by simply tilting the 32°-cut BBO crystal employed for broadband amplification. In any case the radius of the superfluorescence ring imaged on a far-field screen is smaller than in the broadband case and its colours are spread into a thicker ring –red in its inner side and blue farther from the pump.

Since no additional chirp is introduced with respect to the broadband configuration, it's not necessary to change the number of reflections (10) onto the DCMs to get nearly transform-limited pulses. The polarization of the amplified pulses maintains the one of the white light, vertical as the fundamental laser beam, while their energy is up to  $1.5 \mu J$ . Some of the spectra obtained by tilting the crystal are reported in Fig. 2.3, together with

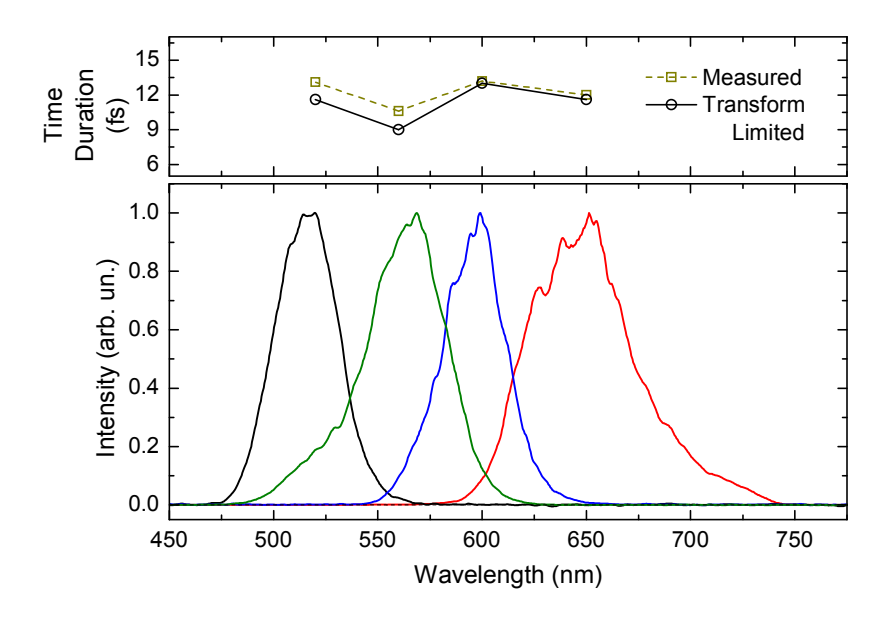


FIG 2.3. Narrow-band tunable pulse spectra (bottom panel) together with their TL and measured duration (top panel).

their transform limited duration (in the 10-fs range). As in this case we don't need extreme temporal resolution, we measured pulse duration by means of a simple non-collinear autocorrelation technique. Obtained pulse durations (also shown if Fig. 2.3) are very close to the TL and anyhow shorter than 15 fs, indicating small residual chirp in the pulses.

#### 2.2.3 Near-IR non-collinear optical parametric amplifier

The tunable visible OPA can be easily configured to generate pulses in the near-IR spectral region; the only difference lays in the stage of signal generation and filtering. In order to increase the signal spectral energy density in the IR, white light is generated in a 2-mm thick sapphire plate and then filtered with a 1-mm-thick Schott long-pass filter (RG830).

A set of the recorded spectra is given in figure 2.4 along with measured and transform-limited durations. For centre wavelengths near 900 nm, pulse compression is necessary to compensate for the chirp introduced by self-phase modulation and propagation in the sapphire plate: since no suitable Chirped Mirrors are available for the

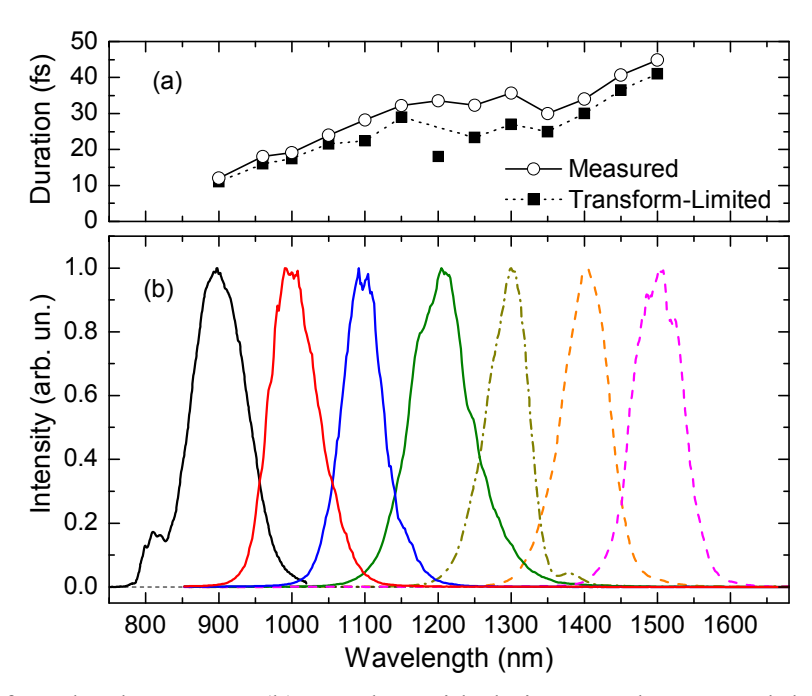


FIG 2.4. Near-infrared pulse spectra (b) together with their TL and measured duration (a).

purpose, we adopted a prism-pair compression stage. Two Fused Silica prisms were employed, cut at Brewster angle and kept at a distance of 21 cm; to prevent power losses due to Fresnel reflections on the prism surfaces, polarization is set horizontal thanks to a periscope or a broadband  $\lambda/2$  plate (CVI QWPO). From 900 nm to 1200 nm pulses from 12 fs to 20 fs can be obtained, and the compression can be adjusted so that measured pulses are only 15% longer than the transform-limited expected duration. For longer wavelengths dispersion gets negligible since GDD reduces very much, and the duration of the amplified pulses goes from 30 fs to 45 fs, approaching the transform limit also without any compression stage.

In addition, to get the maximum amplification, care should be taken in setting the initial alignment of the beams, in accordance to the effect already described in paragraph 1.4.2 and showed in Fig. 1.16: during its amplification, the IR pulse travelling in the BBO may undergo frequency duplication, which is a detrimental effect because it reduces the energy of each amplified pulse. This process arises since the IR beam runs close to the phase-matching direction for SHG, namely  $\theta = 20^{\circ}-25^{\circ}$ . The parasitic SH generation again depends on the orientation of the BBO optical axis with respect to the signal: given the initial condition  $\theta = 30^{\circ}$ , the signal can be driven either in the same half plane of the optical axis or in the opposite one. In the first case the signal forms with the optical axis an angle smaller than 30° in a quasi-phase-matching direction for SHG, and the energy of the amplified IR pulse partially transfers to its second harmonic; in the second case phase matching is hardly fulfilled, and SHG can be strongly reduced, even though not avoided. The desired geometrical arrangement of the three elements (i) optical axis, (ii) Pump and (iii) Signal is the one drawn in Fig. 1.16(b), and is exactly the one which allows to efficiently double the idler beam frequency when performing the broadband amplification in the visible [Baltuška et al., 2002b]. Also in this optimised case, the amplified fundamental IR runs collinear to a weak visible SH, which can help in a firstorder alignment of the following stages and which is easily removed by a thin, dispersion-free long-pass filter or a set of prisms. Typically, the energy of these IR pulses reaches 1 µJ.

#### 2.2.4 Generation of blue pulses

The prism-compressed, amplified pulses around 900 nm just described can be used as a source for short pulses under 500 nm, which cannot be obtained by the broadband, visible OPA illustrated in chapter 1. To generate such pulses, the horizontally polarized IR pulses are focused by a f = 50 mm mirror onto a 50- $\mu$ m-thick BBO crystal cut at  $\theta = 26^{\circ}$  for type I SHG; by suitably adjusting the prism-pair compression stage and the position of the crystal just after the focus, broadband, short pulses around 450 nm are generated thanks to an efficient frequency doubling. The vertically-polarised pulses thus generated have energy of about 250 nJ. In Fig. 2.5(b) we show some examples of measured spectra of these pulses.

Nearly-transform-limited pulses can be obtained by pre-compensating with the prism-pair on the IR path the dispersion introduced by the frequency conversion and the thin 50-µm BBO. TL durations are in the 10–15-fs range (see Fig. 2.5(a)). Direct measurement of blue-pulse duration through auto-correlation technique is not possible because no SHG crystal is available in this spectral region. Indirect estimation of pulse duration is anyway possible observing the rise time of a pump-probe trace which, in case of a sample giving way to a photo-induced signal without delay, corresponds to the

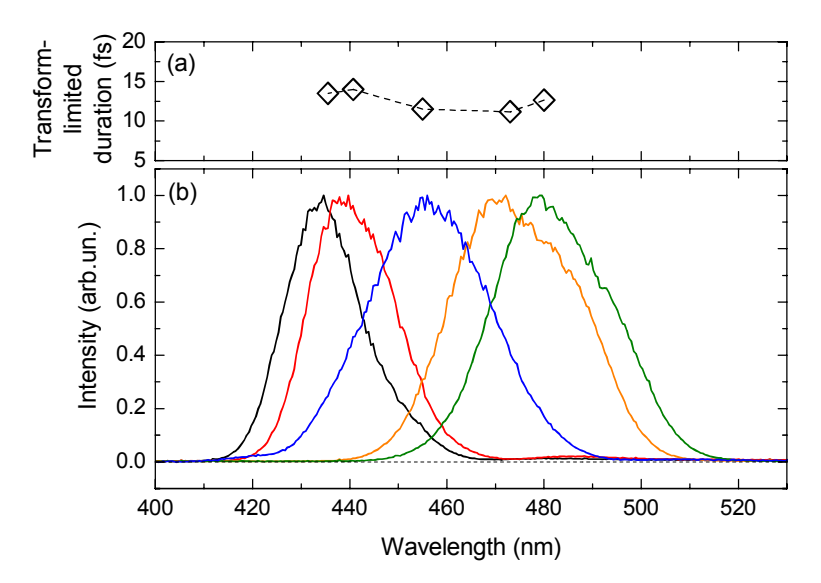


FIG 2.5. TL duration (a) and spectra (b) of blue pulses obtained by frequency doubling NIR pulses.

temporal integral of the cross-correlation between the pump and the probe pulses. Using this method we retrieved a 10–20-fs pulse duration, very close to the TL.

#### 2.2.5 Generation of UV pulses

Every time one needs light with photon energy higher than the blue pulses just described, for example for pumping those samples which have absorption transitions above 3 eV, a possible solution can be found in up-conversion of a visible narrow-band femtosecond pulse (such as those described in 2.2.2) with the fundamental  $\lambda$ =780 nm beam. The sum-frequency generation crystal used is a 50- $\mu$ m-thick BBO cut for type II phase matching (e+o $\rightarrow$ e). A very thin crystal ensures broad up-conversion bandwidth, though low efficiency is expected. In the ordinary axis is placed the visible beam delivered from the narrow-band OPA, while in the extraordinary axis is located the fundamental beam at 780 nm. The resulting up-converted ultraviolet pulse will then have extraordinary polarization (i.e. horizontal) and will preserve the bandwidth of the visible pulse.

Some of the generated pulse spectra are shown in Fig. 2.6, together with their transform-limited duration, in the 10–15-fs range. Direct measurement of UV pulse

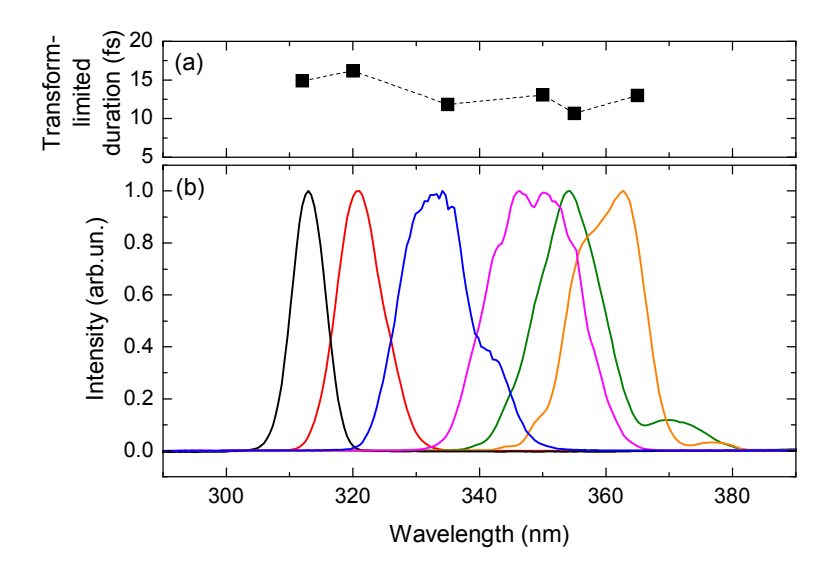


FIG 2.6. TL duration (a) and spectra (b) of UV pulses obtained by frequency up-converting visible pulses with the fundamental 780-nm beam.

duration through auto-correlation technique is not possible as already explained for blue pulses. Indirect estimation of this parameter through pump-probe experiments gave us a 15–25-fs pulsewidth.

#### 2.3 Pump-probe system

#### 2.3.1 Theory of pump-probe

Pump-probe is a powerful spectroscopic technique for the characterization of excited-state dynamics in various materials. It enables the measurement of several important material properties such as the temporal profile of excited-state population, electronic and vibrational lifetimes and coherent effects such as collective molecular oscillations. In a classical pump-probe experiment, the system is resonantly excited by a pump pulse and its subsequent evolution is monitored by the pump-induced absorption change of a delayed probe pulse. Absorption of the pump pulse causes a temporary change  $\Delta N(t)$  in the population of the absorbing electronic level, thus altering the absorption A(t) of the probe pulse by the sample. Taking into account the finite duration of the pump pulse, the temporal profile of the resulting change in absorption  $\Delta \alpha(t)$  is the convolution between the pump pulse profile  $I_{pu}(t)$  and the impulsive response of the medium A(t):

$$\Delta \alpha(t) = \int_{-\infty}^{+\infty} A(t - t') I_{pu}(t') dt'.$$
 (1)

Our final goal will be to extract A(t) from a pump-probe differential transmission trace. The measurement compares the transmission W of the probe pulse  $I_{pr}(t-\tau)$ , at a certain pump-probe delay  $\tau$ , by the sample when it has been excited by the pump pulse  $(W_{on})$  and when it has not  $(W_{off})$ :

$$W_{on}(t,\tau) = I_{pr}(t-\tau) \exp[-(\alpha + \Delta\alpha)D]$$
 (2a)

$$W_{\text{off}}(t,\tau) = I_{\text{pr}}(t-\tau)\exp(-\alpha D) \tag{2b}$$

At the first order in excitation intensity (i.e. when small population change is produced by the pump pulse) it results  $\Delta\alpha D\ll 1$ , so that the differential transmission  $\Delta W=W_{on}-W_{off}$  can be written as:

$$\Delta W(t,\tau) = I_{pr}(t-\tau)\exp(-\alpha D)\left\{\exp[-\Delta\alpha(t)D] - 1\right\} \cong -I_{pr}(t-\tau)\Delta\alpha(t)D\exp(-\alpha D). \tag{3}$$

Using a slow, integrating photodetector, the measured trace is the mean probe transmitted energy  $E_{pr}^{T}$  over a great number of periods. The resulting percentage variation in probe transmission for a certain delay  $\tau$  can thus be written as:

$$\frac{\Delta T}{T}(\tau) = \frac{\Delta E_{pr}^{T}}{E_{pr}^{T}} = \frac{\int_{-\infty}^{\infty} \Delta W(t,\tau) dt}{\int_{-\infty}^{\infty} W_{off}(t,\tau) dt} = \frac{-De^{-\alpha D} \int_{-\infty}^{\infty} I_{pr}(t-\tau) \Delta \alpha(t) dt}{-e^{-\alpha D} \int_{-\infty}^{\infty} I_{pr}(t-\tau) dt} = -\frac{D \int_{-\infty}^{\infty} I_{pr}(t-\tau) \Delta \alpha(t) dt}{E_{pr}}$$
(4)

By inserting equation (1) into (4) and applying a change of variables it results that the differential transmission change  $\Delta T/T$  is proportional to the convolution between the impulsive response of the medium A(t) and the cross-correlation between pump and probe pulses  $C(t) = I_{pr} \otimes I_{pu} = \int_{-\infty}^{\infty} I_{pr}(t') I_{pu}(t'+t) dt'$ :

$$\frac{\Delta T}{T}(\tau) \propto \int_{-\infty}^{\infty} I_{pr}(t-\tau) \int_{-\infty}^{+\infty} A(t-t') I_{pu}(t') dt' dt = \int_{-\infty}^{+\infty} A(\tau-\xi) C(\xi) d\xi = A * C \ . \tag{5}$$

In order to retrieve A(t) it is thus necessary to deconvolve the measured  $\Delta T/T$  trace with the pump-probe cross-correlation C(t) separately characterized. An experimental set-up for pump-probe, auto-correlation and cross-correlation measurements will be described in the next section. We note that this indirect procedure can lead to ambiguities in the assignment of the underlying processes, especially when observing fast population dynamics. This calls to the use of as short as possible pulses, like the ones described in this first part of the work.

In general, a pump-probe measurement can generate three different types of signals. With refer to the Fig. 2.7, let us assume that the pump pulse excites the relaxed system inducing a transition from the ground state "A" to a higher state "C". The probe pulse transmission can thus be either enhanced or reduced depending on the relationship between its photon energy and the energy spacing between the electronic and vibrational levels of the molecule under study as resumed in this scheme:

- (a) When the probe pulse is resonant with the optical transition  $C \rightarrow D$  from the pump-populated level "C" to a higher-lying level "D", then it will be absorbed by the molecule. This phenomenon reduces the transmission of the probe pulse with respect to the un-perturbed system. This signal is therefore called Photo-induced Absorption (PA) and corresponds to negative  $\Delta T/T$  signals.
- (b) When the probe pulse is resonant with the A→C transition (this is the case, for example, of a one-colour degenerate pump-probe experiment), then its transmission will be enhanced because the pump pulse has reduced the ground-state population, thus temporarily producing an increased sample transparency. This signal is therefore called Photo-Bleaching (PB) and corresponds to positive ΔT/T signals.
- (c) When the probe pulse is resonant with the C→B transition from the pump-populated level "C" to a lower-lying level "B", then it will stimulate the emission of a second photon. The resulting transmission will then be increased (ΔT/T>0) and the signal is called Stimulated Emission (SE). It is also possible to directly stimulate the C→A transition, through a process which is complementary to (b). In this case, however, the photon energies at which the SE process occur are smaller to the ones relevant to the PB signal, due to the Raman shift between absorption and emission associated with the vibrational energies of the "A" and "C" electronic levels.

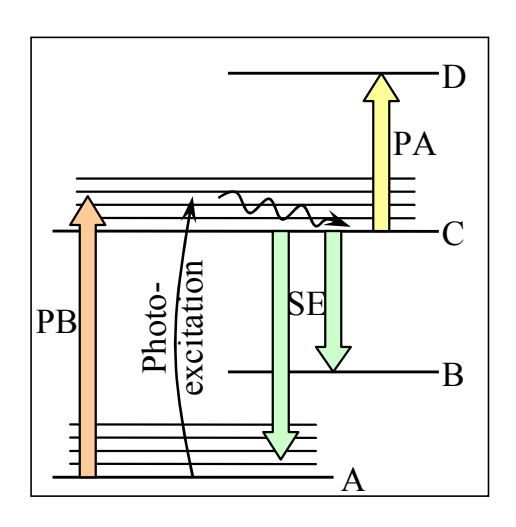


FIG 2.7. Scheme of the possible signals that a pumpprobe measurement can produce: photo-bleaching (PB), stimulated emission (SE) and photo-induced absorption (PA).

#### 2.3.2 Pump-probe experimental set-up

A schematic of the apparatus used for pump-probe experiments is shown in Fig. 2.8. This system is designed to accommodate a broad range of pump and probe wavelengths maintaining a very high temporal resolution. It is based on a balanced Michelson interferometer: beam splitters BS1 and BS2 consist of 120-μm-thick glass slides coated with Inconel (Laser Zentrum Hannover e.V., on-demand coating deposition). This coating guarantees a nearly uniform 40% reflection and 20% transmittance over a very broad bandwidth, from 300 to 2000 nm. In one arm of the interferometer is placed a delay-line, formed by two 90° mirrors M2 and M3 mounted on a precision translation stage with 0,1-μm positioning accuracy (Physik Instrumente Gmbh, model M-511.DD) resulting in a 2/3-fs timing resolution. The two pulse replicas are combined onto the BS2 beam splitter in a non-collinear geometry, so that the two beams propagate parallel to each other towards the spherical curved mirror (f = 100 mm) which focuses them onto the sample. This configuration is preferred to the use of a lens because, even though it could introduce some astigmatism in the beams, it avoids additional spectral chirp in the pulses.

By placing the mirror M4 before the sample it is possible to deviate the beams to a non-linear Sum-Frequency-Generation (SFG) crystal, thus obtaining a non-collinear auto-

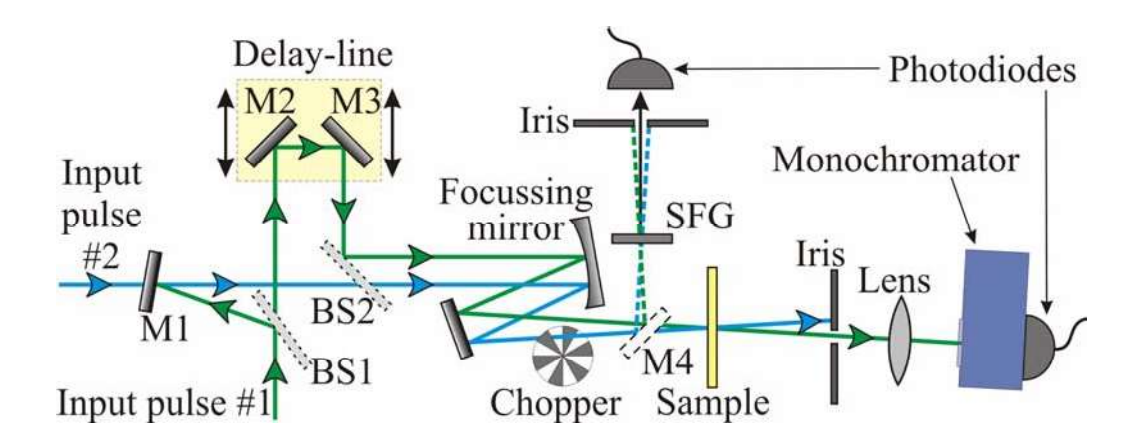


FIG 2.8. Balanced Michelson interferometer for auto-correlation (with mirror M1 and one input beam) or cross-correlation (without mirror M1 and with two input beams) measurements. By removing mirror M4, it becomes a one- or two-colours pump-probe setup. BS, beam splitters; SFG, sum-frequency generation crystal.

correlation setup capable of measuring the duration of the pulses. As SFG material we used a BBO crystal, properly cut and tilted to obtain phase matching at the desired wavelength. In order to ensure a broad spectral conversion, we employ a very thin BBO ( $L = 50 \mu m$ ), thinner than the coherent length. The resulting SFG efficiency is small but still sufficient in order to detect the up-converted pulse, properly separated from the original pulses by means of an iris. When the SH to be detected lies in the visible (i.e. when measuring the duration of the NIR pulses) we use a simple photodiode; on the other hand, when the SH to be detected lies in the ultraviolet (i.e. when measuring the duration of the visible pulses) we employ an UV-extended photomultiplier.

By removing mirror M1 and properly aligning a second input pulse deriving from a different OPA, it is possible to shift from the previously described auto-correlation setup to a cross-correlation one, enabling a two-colours pump-probe system. After the sample, the probe beam is selected by means of an iris and focussed by a lens to the 150–300- $\mu$ m aperture of a monochromator (CVI – model CM110) delivering a 5–10-nm-wide spectral line to its exit, where a photodiode is placed. To increase the sensitivity and the S/N ratio of this setup, the pump beam is modulated at  $\approx$ 500 Hz frequency by a mechanical chopper (Thorlabs MC1000) and synchronous lock-in demodulation (Stanford SR830) is applied on the probe signal, thus enabling the detection of differential transmission ( $\Delta$ T/T) signals as low as 0.1%.

When samples in solution are to be studied, we employ a home-made cell with two 200-µm fused silica windows fixed at a distance ≈200 µm (optical path) with Torr Seal epoxy resin, which is not reactive with most of the common solvents. As we must often deal with small quantities of samples, due to difficult and expensive synthetization, production or purification, in order to reduce their wasting we often use no flowing cell, thus enabling the study of sample volumes as small as 100 nl. Since the average power is quite low, in the µW range, no sample degradation is observed during the experiments. Nevertheless, we periodically check that no sample passivation, bleaching or destruction occurred by simply shifting the position of the cell in the focal plane of the pump-probe beams and we replace the solution at the beginning of each experimental run. In this case, pump-probe cross-correlation measurements for system temporal-resolution characterization and zero-time-delay withdrawal are made with a twin fused-silica window placed in front of the SHG crystal, to take into account its dispersion effect on the pulses. Typical cross-correlation FWHM measured durations are around 20–25-fs for narrowband visible  $\leftrightarrow$  broadband visible pulses,  $\approx 30$  fs for narrowband visible  $\leftrightarrow$  near-infrared pulses and  $\approx 45$  fs for ultraviolet  $\leftrightarrow$  broadband visible pulses.

Time-resolved measurements at specific probe wavelengths can be obtained by spectrally filtering, with 10-nm bandwidth interference filters, the probe beam after it passes through the sample and combining differential detection with lock-in amplification. Transmission difference spectra over the entire bandwidth of the probe pulse at specific delays are then reconstructed from the time traces. In all measurements the maximum  $\Delta T/T$  signal must not exceed 10%, thereby ensuring that saturation does not occur.

In the next chapters we will describe experimental pump-probe results on the early events of excited state dynamics in carotenoids and light-harvesting complexes, a very important class of molecules, interesting for physicists, chemists and biologists, due to their role in photosynthesis.

#### Chapter 3

## Ultrafast spectroscopy of carotenoids: detection of an intermediate excited state

#### 3.1 Introduction

Carotenoids are among the most investigated molecules in organic physics and chemistry [Isler et al., 1971]. They are ubiquitous pigments in photosynthetic systems, performing several vital functions [Frank and Cogdell, 1996]. They photo-protect the photosynthetic apparatus by dissipating the excess solar energy and quenching both triplet excited (bacterio)chlorophyll (BChl) and singlet oxygen due to their low-lying triplet state [Siefermann-Harms, 1987; Mimuro and Katoh, 1991; Koyama, 1991; Frank and Cogdell, 1996]. This is their essential role and there would be no photosynthesis in the presence of oxygen without them. They also serve as accessory light-harvesting pigments: light absorbed by donor carotenoids in the blue-green region of the spectrum is transferred to acceptor (B)Chls via singlet-singlet Energy Transfer (ET) with very high efficiency (up to ≈100%), thereby making it available to drive photosynthesis. Carotenoids also have distinct structural functions (as structure stabilization) [Lang et al., 1994] and are involved in plants in non-photochemical quenching via the xanthophyll cycle [Yamamoto et al., 1999]. Besides their role in photosynthesis, carotenoids are also widely studied as models for conjugated polymers [Pellegrin et al., 1991] and are also considered as candidates for molecular electronics applications [Harada et al., 1980].

Carotenoids [recently excellently reviewed by Polívka and Sundström, 2004] have a characteristic strong absorption in the visible region, due to the optically allowed electronic transition from their ground state  $S_0$  (of  $1^1A_g^-$  symmetry, according to the  $C_{2h}$  point group, in analogy to all-*trans*-polyenes), to their second excited singlet state  $S_2$ 

(1<sup>1</sup>B<sub>u</sub><sup>+</sup>) [Hudson and Kohler, 1972; Schulten and Karplus, 1972]. The first excited state S<sub>1</sub> (2<sup>1</sup>A<sub>g</sub><sup>-</sup>) has the same symmetry as the ground state and is therefore optically forbidden ("dark" state); it is however reached in a few hundreds of femtoseconds after photoexcitation, via an ultrafast Internal Conversion (IC) from S<sub>2</sub>, denoted IC<sub>21</sub> in the following [Shreve et. al., 1991; Kandori et al., 1994; Macpherson and Gillbro, 1998; Polli et al., 2003]. Nonradiative decay from S<sub>1</sub> to S<sub>0</sub> (indicated as IC<sub>10</sub> in the following) then occurs on a 10-ps time scale [Andersson et al., 1995a; Frank et al., 1997]. Intersystem crossing to the triplet manifold is rather inefficient but does occur in some purple bacterial antenna complexes [Gradinaru et al., 2001; Papagiannakis et al., 2002].

Most studies on the photophysics of carotenoids have used the three state model described above to interpret their results. However, previous theoretical work by Tavan and Schulten had indicated the possible existence of additional excited singlet states (e.g.  $1^{^{1}}B_{u}^{^{-}}$  and  $3^{^{1}}A_{g}^{^{-}})$  between  $S_{2}$  and  $S_{1}$  for carotenoids with more than  $\approx\!\!9$  conjugated double bonds (number of conjugated double bonds N) [Tavan and Schulten, 1986, 1987]. The existence of such states (of  $1^{1}B_{u}^{-}$  and  $3^{1}A_{g}^{-}$  symmetry) was experimentally confirmed in various all-trans-carotenoids with different techniques: mini-9- $\beta$ -carotene (N=9) [resonance-Raman excitation profiles, RREP, Sashima et al., 2000], neurosporene (N=9) [time-resolved absorption spectroscopy, TRAS, Zhang et al., 2000a; Fujii et al., 2003], spheroidene (N=10) [RREP, Sashima et al., 1999; RREP, Furuichi et al., 2002; TRAS, Fujii et al., 2003], β-carotene (N=11) [RREP, Sashima et al., 2000; time-resolved Raman spectroscopy, Yoshizawa et al., 2001], lycopene (N=11) [RREP, Sashima et al., 2000; RREP, Furuichi et al., 2002; TRAS, Fujii et al., 2003], anhydrorhodovibrin (N=12) [Fluorescence Spectroscopy, FS, and TRAS, Fujii et al., 2001, 2003; RREP, Furuichi et al., 2002], spirilloxanthin (N=13) [FS and TRAS, Fujii et al., 2001, 2003; RREP, Furuichi et al., 2002; TRAS, Nishimura et al., 2004]. The IC<sub>21</sub> dynamics in all-trans-β-carotene was also recently studied by Kukura et al. using time-resolved stimulated Raman spectroscopy [Kukura et al., 2004]: while the authors explained their results without an intermediate excited state, their temporal resolution, set by a 115 fs instrument response, was not sufficient to observe the very fast  $S_2$ - $S_x$  transition.

Given the very fast timescale of  $IC_{21}$  processes, its full characterization challenges the  $\approx 100$ -fs temporal resolution of standard pump-probe systems; in particular the need of deconvolving the instrumental response from the measured dynamics can lead to ambiguities in the assignment of the underlying processes. The recent availability of pulses with 10-20 fs duration, tuneable throughout the visible and Near-InfraRed (NIR), as we showed in chapters 1 and 2, allows probing the early events of energy relaxation in carotenoids with unprecedented temporal resolution. Here, we exploit this improved temporal resolution to directly monitor the dynamical resolution of the intermediate  $S_x$  state.

In paragraph 3.2 we will present experimental results on  $\beta$ -carotene and lycopene, two carotenoids with N=11, demonstrating how with femtosecond pump-probe spectroscopy it is possible to detect the presence of the  $S_x$  intermediate state. In paragraph 3.3 we will extend our study to carotenoids with different conjugation length (N=5 to 15) and we will show how the presence of the intermediate state in the long carotenoids can explain the dependence of their internal conversion rate  $IC_{21}$  on N.

### 3.2 Early events of energy relaxation in $\beta$ -carotene and lycopene

We studied two carotenoids, all-*trans*- $\beta$ -carotene and lycopene, in cyclohexane solution at room temperature. Their chemical structure, steady-state absorption and pump pulse spectra are shown in Fig. 3.1 and 3.2. Both molecules were excited by the 15-fs blue pulses centred at 510 nm for  $\beta$ -carotene and 530 nm for lycopene, resonant with the zero-phonon line of the  $S_0 \rightarrow S_2$  transition, generated by the tunable visible OPA described in paragraph 2.2.2. The temporal evolution of differential transmission was probed in the visible spectral range (500–700 nm) using the sub-10-fs pulses derived from the broadband OPA described in chapter 1 and in the near-IR range (820-1020 nm) using 12-fs pulses derived from the NOPA described in paragraph 2.2.3. With respect to previously reported experiments [Cerullo et al., 2001], we have deliberately decreased

the pump pulse bandwidth, thus slightly worsening the temporal resolution, for three reasons: (i) to increase spectral selectivity; (ii) to reduce artifacts around zero time delay; (iii) to avoid the excitation of coherent oscillations superimposed on the population dynamics.  $\beta$ -carotene was purchased from Sigma and used without further purification. Lycopene was extracted and purified from tomato paste. Its purity was confirmed by silica gel thin layer chromatography and absorption spectroscopy.

m5 (
$$N$$
=5)

Neurosporene ( $N$ =9)

Lycopene ( $N$ =11)

 $\beta$ -carotene ( $N$ =11)

M13 ( $N$ =13)

M15 ( $N$ =15)

FIG 3.1. Chemical structures of the carotenoids studied.

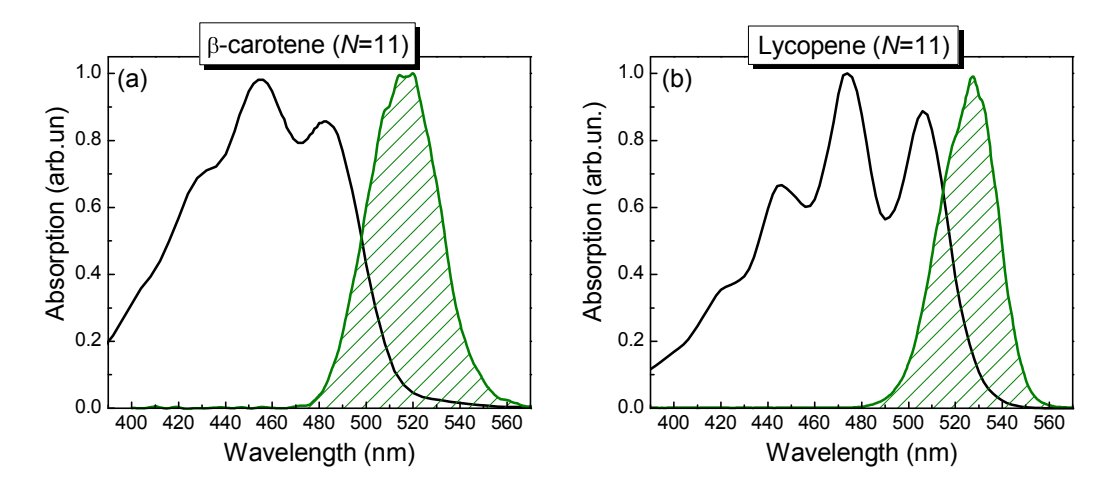


FIG 3.2. Steady-state absorption spectrum (black line) and pump pulse spectrum (green dashed area) of  $\beta$ -carotene (a) and lycopene (b).

#### 3.2.1 Ultrafast internal conversion in β-carotene

Figure 3.3 shows differential transmission spectra in all-*trans*- $\beta$ -carotene at three different time delays after photoexcitation. Following the pump pulse we observe the prompt appearance of a broad Photoinduced Absorption (PA) band, extending from 600 to 950 nm: we call this band PA<sub>2</sub>. The band decays very quickly and is replaced, within  $\approx 50$  fs, by another band (PA<sub>x</sub>) peaking at 980 nm; PA<sub>x</sub> decays on the 100-fs timescale with a kinetic matching the formation of a new band (PA<sub>1</sub>) peaking at 565 nm. The PA<sub>1</sub> band is a well known feature of carotenoids [Shreve et al., 1991; Cerullo et al., 2001] and is assigned to S<sub>1</sub> $\rightarrow$ S<sub>n</sub> absorption, thus providing a spectral signature of the internal conversion process. The PA<sub>x</sub> band was also previously observed [Yoshizawa et al., 2001; Zhang et al., 2001b] and attributed to transient absorption from the S<sub>2</sub> state; the PA<sub>2</sub> band is reported here for the first time. These data are at variance with those expected in the classical three-level picture of carotenoid singlet states as described above and clearly indicate the presence of an extra state between S<sub>2</sub> and S<sub>1</sub>. We assign PA<sub>2</sub> and PA<sub>x</sub> to

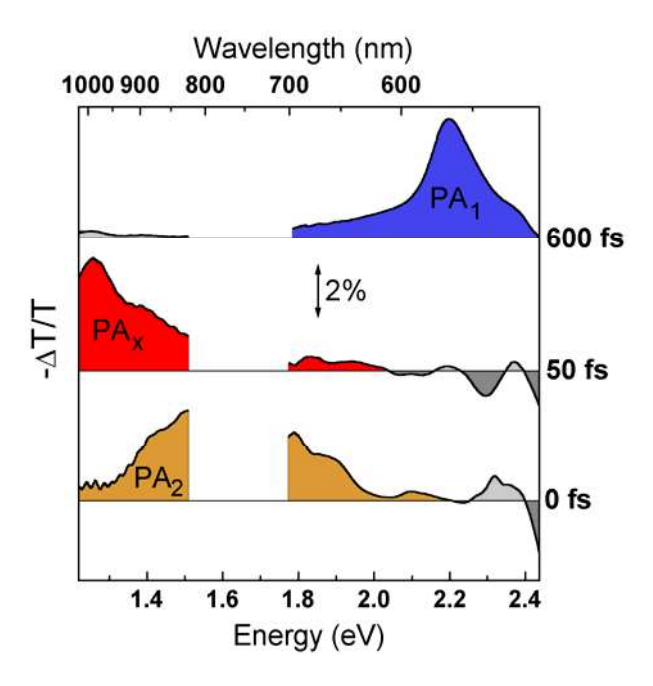


FIG 3.3. Differential transmission spectra in all-*trans* β-carotene in cyclohexane solution at different time delays after photoexcitation by a 15-fs pulse resonant with the  $S_0$ – $S_2$  transition. A sub-10-fs visible pulse probes the 500- to 710-nm wavelength region, whereas a 12-fs near-infrared pulse probes the 820- to 1020-nm region.

transient absorption from the  $S_2$  and  $S_x$  states, respectively; the very rapid decay of  $PA_2$  and the corresponding rise of  $PA_x$  highlight the initial  $S_2 \rightarrow S_x$  conversion process. The detailed evolution of this NIR band, showing the rapid decrease of the  $PA_2$  signal and formation of the  $PA_x$  one is shown in Fig. 3.4. The subsequent decay of  $PA_x$  and rise of  $PA_1$  correspond to the  $S_x \rightarrow S_1$  conversion.

This photoexcitation scenario is confirmed by differential transmission dynamics at different probe wavelengths, shown in Fig. 3.5. Since each wavelength presents the overlap of several absorption features, their interpretation is not straightforward and will be given in detail in the following. At the wavelength of 850 nm (Fig. 3.5(c)) we see an instantaneously rising signal, due the PA<sub>2</sub> band, which decays within 50 fs; at longer times, we observe a tail of the PA<sub>x</sub> band, disappearing within  $\approx$ 400 fs. At the wavelength of 980 nm (Fig. 3.5(d)) we see the delayed PA<sub>x</sub> absorption, with a risetime matching the PA<sub>2</sub> decay and a subsequent decay, over the timescale of a few hundreds of femtoseconds, to form PA<sub>1</sub>. The PA<sub>1</sub> band is best monitored at the wavelength of 560 nm (Fig. 3.5(a)); note that it does not rise instantaneously after photoexcitation, but is rather

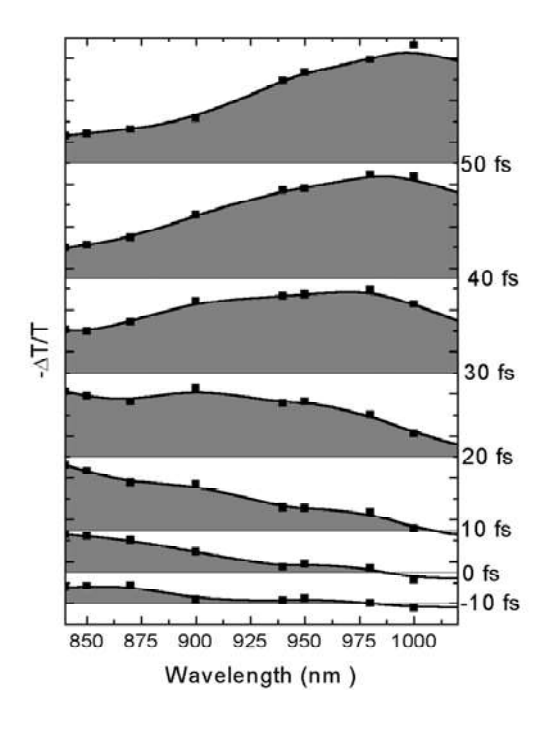


FIG 3.4. Detailed evolution of the differential transmission spectra in the NIR wavelength range of all-*trans*  $\beta$ -carotene in cyclohexane solution at different time delays after photoexcitation.

delayed by  $\approx 50$  fs, in agreement with our kinetic model. At the wavelength of 650 nm (Fig. 3.5(b)) we observe, again, at early times a signature of the PA<sub>2</sub> band followed by the slow rise of PA<sub>1</sub>. Figure 3.5(e) shows the initial kinetics of PA<sub>2</sub> and PA<sub>x</sub>. On this expanded timescale, the delay in the formation of PA<sub>x</sub> relative to PA<sub>2</sub> is clearly seen. The measured pump-probe cross-correlation (grey area in Fig. 3.5(e)) illustrates that this delay is well resolved.

#### 3.2.2 Data analysis

The experimental data were fitted (red solid lines in Fig. 3.5) using a 4-level rate equations model, assuming instantaneous population of  $S_2$  and energy relaxation first to  $S_x$  (with rate  $k_{2x}$ ) and then to  $S_1$  (with rate  $k_{x1}$ ), which in turn relaxes to the ground state  $S_0$  (with rate  $k_{10}$ ). The rate equation model is of the form:

$$\frac{dN_2}{dt} = -k_{2x}N_2; \frac{dN_x}{dt} = k_{2x}N_2 - k_{x1}N_x; \frac{dN_1}{dt} = k_{x1}N_x - k_{10}N_1,$$

where  $N_i$  (i=1,x,2) is the population of the  $S_i$  state and  $k_{ij}$  is the internal conversion rate between the  $S_i$  and  $S_j$  states. The differential transmission signal at a certain time t and at

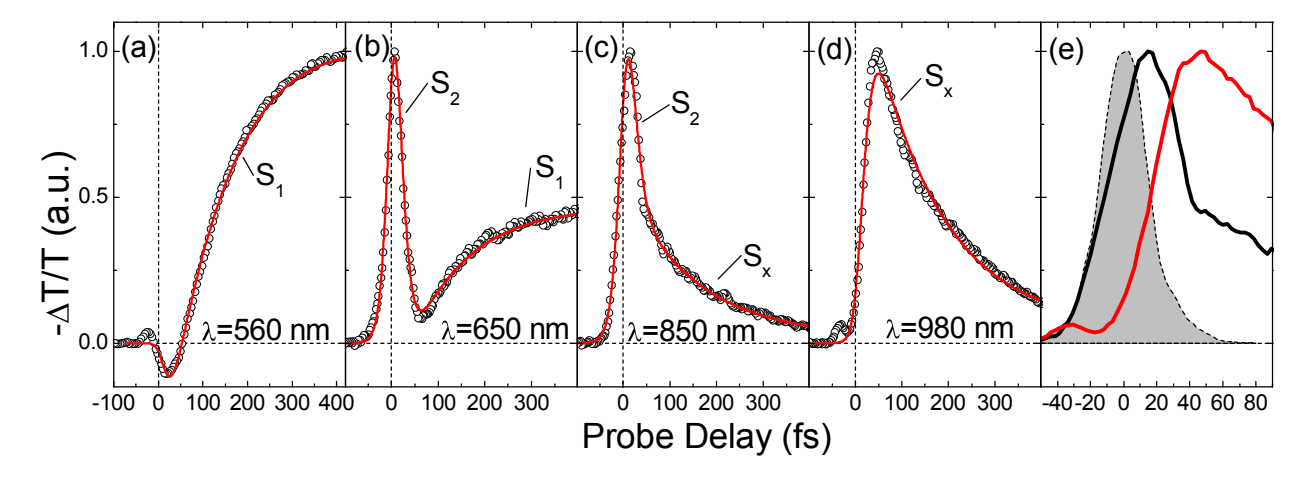


FIG 3.5. (a-d) Circles show differential transmission dynamics in all-trans β-carotene at different probe wavelengths after photoexcitation with a 15-fs pulse resonant with the  $S_0$ – $S_2$  transition. Red solid lines are fits obtained using the four-state model described in the text and convoluting the system response with the pump-probe cross-correlation function. (e) Rise times of the signals at 850 nm (black solid line) and 980 nm (red dotted line), together with a pump-probe cross-correlation (grey area).

 $a \quad frequency \quad \omega \quad will \quad then \quad be: \quad \frac{\Delta T}{T} \big(t,\omega \big) = -d \sum_{i=0}^n \big(\sigma_{i1}(\omega) N_1(t) + \sigma_{ix}(\omega) N_x(t) + \sigma_{i2}(\omega) N_2(t) \big),$ 

where d is the sample thickness and  $\sigma_{ij}$  the cross-section (in cm<sup>2</sup>), containing both the dipole moment of the  $S_i$ - $S_j$  transition and its line-shape, and the summation is extended to all the possible states that can be reached with the probe beam. In order to take into account the finite instrumental response time, the differential transmission signal was finally convoluted with the pump-probe cross-correlation, separately measured as described in chapter 2.

This procedure allowed us to extract the time constants  $\tau_{2x} = 10\pm 2$  fs for the  $S_2 \rightarrow S_x$  conversion process and  $\tau_{x1} = 150$  fs for the  $S_x \rightarrow S_1$  conversion process. Note that use of rate equations should be considered as a first order approximation to describe the extremely fast  $S_2 \rightarrow S_x$  conversion process.

#### 3.2.3 Ultrafast internal conversion in lycopene

In order to be sure that our observations are applicable to carotenoids other than  $\beta$ -carotene, we extended our experiments to include lycopene, another carotenoid with N=11. Differential transmission dynamics at relevant wavelengths are reported in Fig. 3.6. These data can also be explained by introducing an intermediate state; a three-level model is unable to explain the delay in the formation of  $S_x$  absorption (980 nm trace) and in the onset of the exponential rise of  $S_1$  absorption (560 nm trace). Exponential fits (solid lines in Fig. 3.6) give  $\tau_{2x} = 9\pm 2$  fs and  $\tau_{x1} = 90$  fs for lycopene.

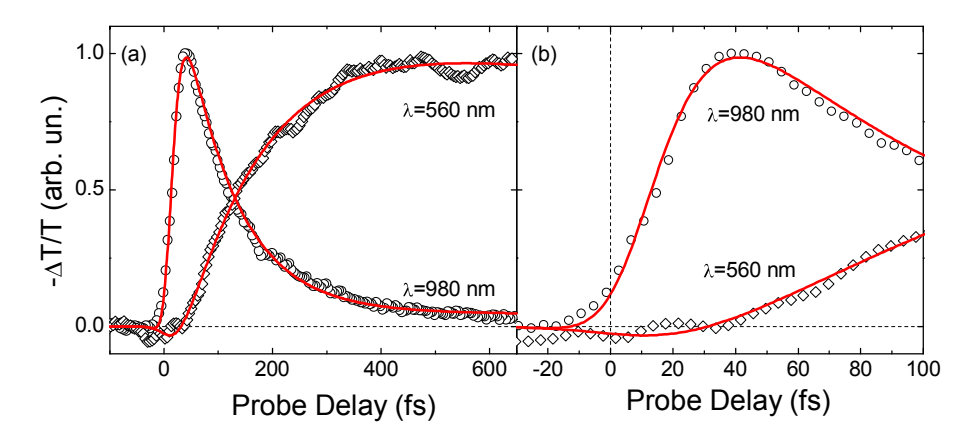


FIG 3.6. (a) Circles show differential transmission dynamics in lycopene at 560 nm and 980 nm. (b) Same as (a) on an expanded timescale, to show the rise time of the signals.

#### 3.2.4 The S<sub>x</sub> intermediate state revealed

We will now put our observations in the context of previous studies on excited state dynamics of carotenoids. The internal conversion of the excited singlet states in carotenoids has been studied by fluorescence up-conversion to follow the  $S_2$  to  $S_1$ transition [Kandori et al., 1994; Macpherson et al., 2001]. Typically the decay of the fluorescence signal from S2 kinetically matches the risetime of S1, monitored by the appearance of the  $S_1 \rightarrow S_n$  absorption. This was interpreted as strong evidence for the classical three-level model depicted in Fig. 3.7(a). However theoretical work by Tavan and Schulten [Tavan and Schulten, 1986, 1987] on long polyenes had previously calculated the energy levels of a number of so-called "covalent states" lying below the first excited ionic state (S<sub>2</sub>). For the backbone lengths relevant to our study, their calculation predicted the presence of an additional low-lying excited singlet state, the S<sub>x</sub> state, between S<sub>2</sub> and S<sub>1</sub>, resulting in the four-level scheme for excited state relaxation depicted in Fig. 3.7(b). The first experimental suggestion that this state does exist was provided by Koyama et al. [Sashima et al., 1999, 2000]. Using resonance Raman spectroscopy, this group located what they designated a  $1^{1}B_{u}^{-}$  state between  $S_{2}$  and  $S_{1}$ . This evidence was supported by time-resolved studies. Zhang et al., 2000, studying excited state dynamics of all-trans-neurosporene in the near infrared, needed to assume a four-level model to fit, by a singular-value decomposition algorithm, the experimental data; Yoshizawa et al., 2001, studying the vibrational relaxation of  $S_1$  of  $\beta$ -carotene by femtosecond time-resolved Raman spectroscopy, also required an additional state

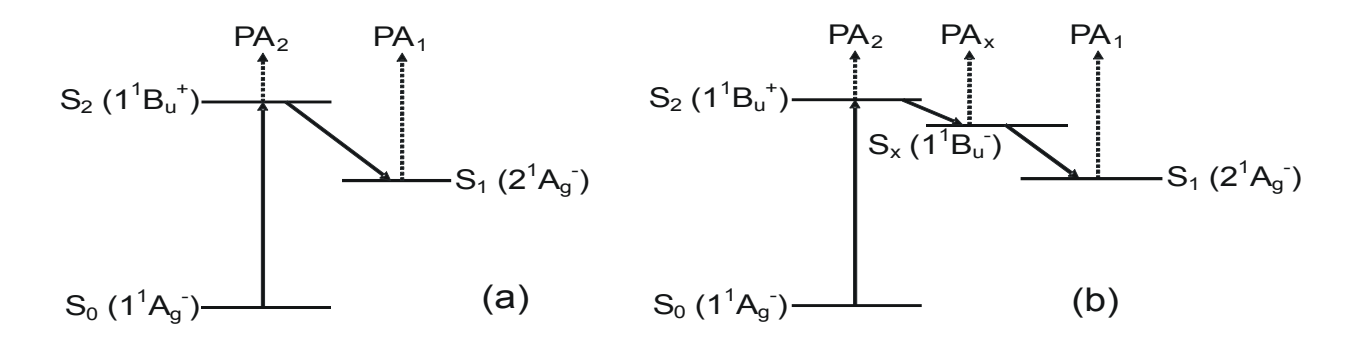


FIG 3.7. Scheme of the three-state model (a) and the four-state model (b) used to describe excited-state dynamics of carotenoids.

between  $S_2$  and  $S_1$  to fit their results. The time resolution used in these experiments ( $\approx 150$  fs) did not allow this proposed intervening state to be directly observed.

With our enhanced temporal resolution, we have unequivocally resolved this intermediate state both in β-carotene and lycopene. We must now consider whether it is indeed a distinct electronic state or some relaxed form of S<sub>2</sub>. For the following reasons we favour the idea that this is a distinct electronic state. Our excitation pulse overlaps only the low-energy side of the carotenoids absorption band, thus enabling selective excitation of the zero-phonon line of the  $S_0 \rightarrow S_2$  transition. Therefore we expect only rather small vibrational relaxation to be possible. The large shift in the position of the transient differential transmission spectra of PA2 and PAx (Fig. 3.3 and Fig. 3.4) is incompatible with the expected small vibrational relaxation. In addition, vibrational relaxation would be expected to shift the PA<sub>2</sub> band to the blue, as is indeed observed for the PA<sub>1</sub> band [Yoshizawa et al., 2001; Cerullo et al., 2001], and not to the red. In order to explain the red shift of PA<sub>x</sub> with respect to PA<sub>2</sub>, a full spectroscopic characterization of the S<sub>2</sub> and S<sub>x</sub> states, as well as the higher lying excited states, is required. A possible explanation could be that optical transitions starting from the two states reach different regions of the higher lying state potential energy surface. Due to strong energy dispersion of this surface, this would result in large difference of the vertical transition energy.

We note that the  $S_2 \rightarrow S_x$  internal conversion process takes place on an extremely fast timescale, comparable to the periods of nuclear vibrations coupled to the optical transition, which are in the 20-fs range [Cerullo et al., 2001; Koyama and Fujii, 1999]; therefore the adiabatic approximation, commonly used to describe excited state dynamics, fails and the reaction should be described as proceeding along a diabatic pathway linking the  $S_2$  and  $S_x$  potential energy surfaces [Wang et al., 1994]. A full molecular dynamics simulation, rather than the simple rate equation model used in this work, would be required to satisfactorily describe this process.

Tavan and Schulten's calculations predicted that this intermediate state should be non-emissive. Our data provide evidence that also the  $S_x$  state in  $\beta$ -carotene is emissive (see trace at 560 nm in Fig. 3.5(b) and differential spectrum at 50-fs delay in Fig. 3.3, showing stimulated emission). This reconciles our data with the previous fluorescence

up-conversion experiments and explains why they failed to identify the intermediate state, detecting an overlap of the fluorescence signals from  $S_2$  and  $S_x$ . How can we explain the predictions of Tavan and Schulten that this new state should be non-emissive? Clearly their calculations invoked strict selection rules based on perfect  $C_{2h}$  symmetry and non-interacting states. The  $S_x$  state could be activated by vibronic coupling with the  $S_2$  state, due to their small energy difference. Another possibility, which we consider more likely, is that departure from the planar configuration, consequent to conformational rearrangement in the excited state following photoexcitation, may relax the spatial selection rules and thus activate emission from  $S_x$ . This argument is supported by the surprisingly high fluorescence emission from  $1^1B_u^-$  that has been observed in lycopene (N=11) and other long-chain carotenoids (N=12 and 13) [Fujii et al, 2001], much higher that the one from  $2^1A_g^-$ .

# 3.3 Conjugation length dependence of internal conversion in carotenoids

Several studies have addressed the dependence of excited state dynamics in carotenoids on conjugation length [Andersson et al., 1995a; Chynwat and Frank, 1995; Frank et al., 1997, 2002; Akimoto et al., 2000]. The IC<sub>10</sub> process was found to be described accurately by the energy gap law for radiationless transitions in large organic molecules [Englman and Jortner, 1970; Andersson and Gillbro, 1995b], assuming a transition rate of the form  $k \div exp(-\beta \Delta E)$ , where  $\Delta E$  is the energy gap between the levels and  $\beta$  a coefficient related to the vibrational frequency coupled to the electronic levels. In particular, the  $S_0$ – $S_1$  gap shrinks for increasing conjugation length, leading to an increase of the IC<sub>10</sub> rate.

The situation is not so clear for the  $IC_{21}$  process which, taking place on an ultrafast timescale, is more difficult to characterize; its rate was determined indirectly from quantum yield measurements [Andersson et al., 1995a; Chynwat and Frank, 1995; Frank et al., 1997, 2002] and directly by monitoring the  $S_2$  lifetime with fluorescence up-

conversion [Akimoto et al., 2000]. Results indicate a minimum of the IC<sub>21</sub> rate around N=9 [Akimoto et al., 2000]. This is in contradiction with theoretical and experimental observations of  $\Delta E_{21}$  energy gap increase with N [Tavan and Schulten, 1986, 1987; Furuichi et al., 2002; Fujii et al., 2003]. The reason for this peculiar conjugation length dependence is still unclear. A proposed explanation is the possible increase in the density of vibrational "accepting" modes in longer carotenoids, which could counteract the widening of the  $S_2$ - $S_1$  energy gap.

Another mechanism that could account for this dependence is the presence, with the longer carotenoids (N>9), of additional excited states with energy intermediate between  $S_2$  and  $S_1$ ; these states could then bridge the energy gap between  $S_2$  and  $S_1$  making  $IC_{21}$  a multistep process. The existence of such states (of  $1^1B_u^-$  and  $3^1A_g^-$  symmetry) was predicted theoretically by Tavan and Schulten in all-trans polyenes [Tavan and Schulten, 1986, 1987] and experimentally confirmed in various all-trans-carotenoids, as we showed in paragraph 3.2 for all-trans-β-carotene and lycopene. In this paragraph, we present a full characterization of the IC<sub>21</sub> dynamics in a series of carotenoids with conjugation length N=5, 9, 13, 15. The use of the specially developed spectroscopic system described in chapters 1 and 2 allowed us to simultaneously probe the dynamics of S<sub>2</sub> and S<sub>1</sub> states and thus to obtain a complete picture of the IC<sub>21</sub> process. In the carotenoids with  $N \ge 9$  we observe the presence of an intermediate state mediating the IC<sub>21</sub> process, while for the carotenoid with N=5 the three-level model is capable of satisfactorily describing the process. The intermediate state makes the IC21 dynamics in the longer carotenoids a two-step process and explains the observed non-monotonic behaviour of its rate upon N.

## 3.3.1 Ultrafast internal conversion in long carotenoids

We studied neurosporene (N=9) and three  $\beta$ -carotene analogues, M13 (N=13), M15 (N=15) and m5 (N=5), where "M" and "m" stand for Macro- $\beta$ -carotene and mini- $\beta$ -carotene, respectively. Chemical structures, steady-state absorption and pump pulse spectra are shown in Figs. 3.1, 3.8 and 3.11(a), respectively. Sample preparation protocols are described elsewhere. Briefly, neurosporene was extracted and purified from

membranes of *Rhodobacter sphaeroides* strain G1C [Cogdell et al., 1983]. m5, M13 and M15 molecules were synthesized, respectively, by a reductive dimerization of  $\beta$ -ionone, C23-ketone and C25-aldehyde catalyzed by a low-valence titanium compound [Yoshizawa et al., 2001]. The present results, combined with the previous ones on carotenoids with *N*=11 presented in paragraph 3.2, allow to obtain a complete picture of the conjugation length dependence of IC<sub>21</sub> dynamics.

Figure 3.9 (circles) shows  $\Delta T/T$  dynamics of M15 (a), M13 (b), and neurosporene (c) in cyclohexane solution in the visible and NIR wavelength regions. Pump central wavelengths are 560 nm, 530 nm and 500 nm (see Fig. 3.8), respectively, tuned to the red  $S_0 \rightarrow S_2$  absorption edge, in order to minimize vibronic relaxation effects. The probe wavelengths correspond to the peaks of three photoinduced absorption (PA) bands, each one of which shows different dynamics. First, a PA band is seen in the NIR, which we call PA<sub>2</sub>, rising instantaneously and decaying within  $\approx 30-100$  fs, depending on the carotenoid (upper traces in Fig. 3.9). Second, a signal, which we call PA<sub>x</sub>, is formed after a delay of  $\approx 30-100$  fs and decays within a few hundreds fs (middle traces in Fig. 3.9). The PA<sub>2</sub> and PA<sub>x</sub> bands show spectral overlap in some of the traces. Finally, in the visible (lower traces in Fig. 3.9), the slow build-up of a third PA band is seen, that we call PA<sub>1</sub>. The formation of this band is completed within a few hundred fs, i.e. on the same time scale as the decay of the PA<sub>x</sub> signal observed in the NIR. In addition, in the

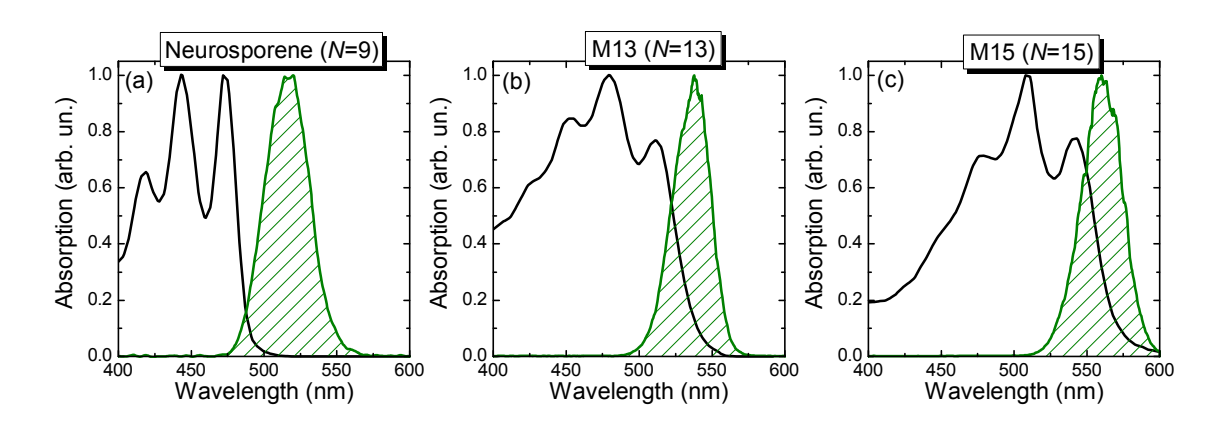


FIG 3.8. Steady-state absorption spectrum (black line) and pump pulse spectrum (green dashed area) of neurosporene (a), M13 (b) and M15 (c).

visible a positive  $\Delta T/T$  signal is seen at early times, which is assigned to Stimulated Emission (SE) because of the negligible ground-state absorption at the probing wavelengths. The PA<sub>1</sub> signals decay on the ps timescale as shown in Fig. 3.12(a).

To verify that the extremely rapid dynamics observed around time zero were not due to artefacts caused by the solvent or pump-probe coherent interaction, we performed measurements on pure cyclohexane, under the same experimental conditions. At all wavelengths we only observed a very small contribution, with the derivative-like shape characteristic of cross-phase modulation.

This picture is supported by  $\Delta T/T$  spectra at different time delays; here we report the results for M15, shown in Fig. 3.10. At 0-fs time delay we observed in the NIR the instantaneously rising PA<sub>2</sub> band, peaking at wavelengths longer than 1000 nm; in the visible Photo-Bleaching (PB) of ground-state absorption and an SE band to the red of the absorption edge were recorded. After  $\approx 30$  fs, the PA<sub>2</sub> band has decayed nearly completely and a new band (PA<sub>x</sub>) appears around 850–900 nm, which decays within a few hundreds fs. The presence of an isosbestic point around 930 nm indicates that PA<sub>x</sub> cannot be a blue-shifted replica of the PA<sub>2</sub> band. The PA<sub>x</sub> band decays with kinetics

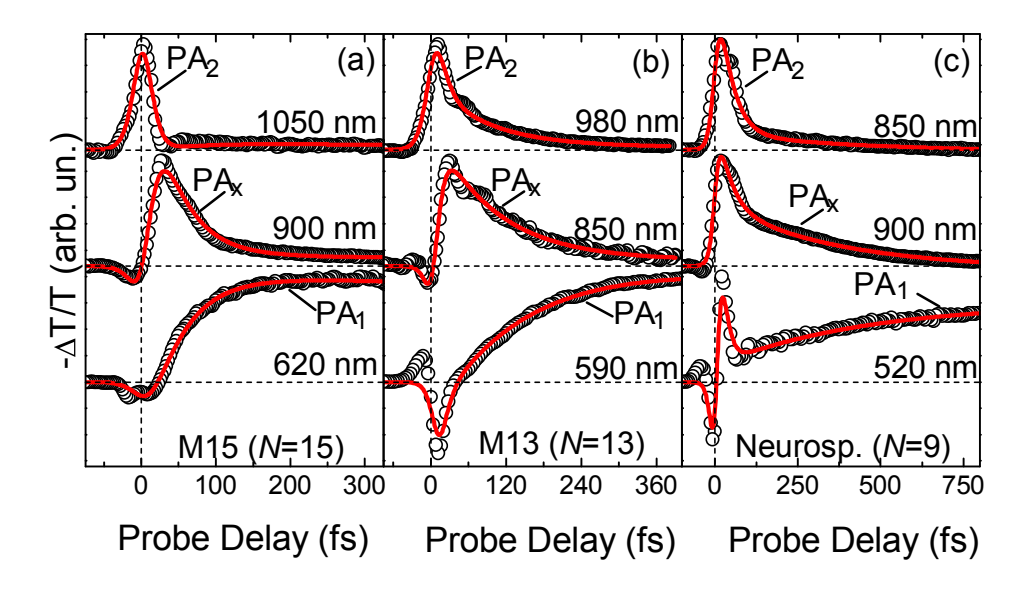


FIG 3.9. Circles show differential transmission dynamics in M15 (a), M13 (b) and neurosporene (c) at different probe wavelengths after photoexcitation with a 15-fs pulse resonant with the  $S_0$ – $S_2$  transition. Solid lines are fits obtained using the four-state model described in the text and convoluting the system response with the pump-probe cross-correlation function.

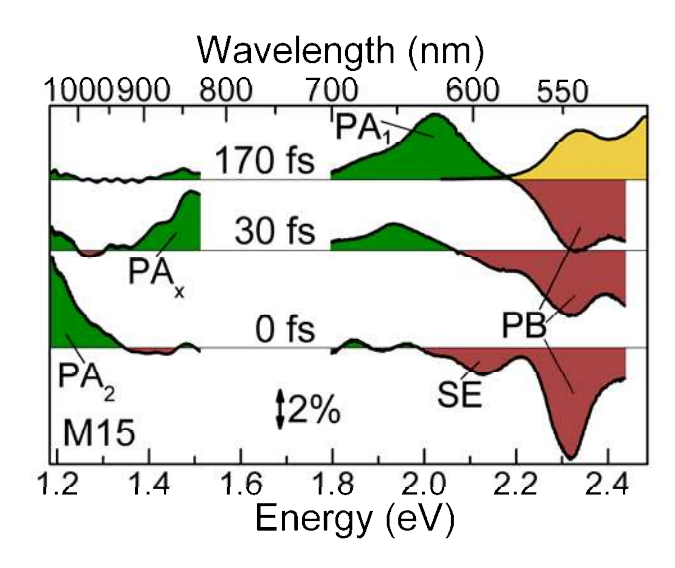


FIG 3.10. Differential transmission spectra of M15 in cyclohexane solution at different time delays in the visible and NIR range. Brown negative areas correspond to photo-bleaching (PB) or stimulated emission (SE). Green positive areas are photo-induced absorption (PA) signals. Yellow area in the top-right corner of the figure is M15 absorption spectrum.

matching those for the formation of the  $PA_1$  band, which peaks at 620 nm and is complete after  $\approx 200$  fs.

The results presented so far reflect the same IC behaviour for all the carotenoids studied. The PA<sub>1</sub> band is well known and it is assigned to the S<sub>1</sub> $\rightarrow$ S<sub>n</sub> transition [Shreve et al., 1991]. Recent measurements on carotenoids observed a short-lived PA band in the NIR and assigned it to S<sub>2</sub> [Yoshizawa et al., 2001; Zhang et al., 2001b]. The improved temporal resolution used in this study enables us to distinguish two features in the NIR spectra: first, a very short-lived absorption (PA<sub>2</sub>); then, a delayed band (PA<sub>x</sub>) originating from PA<sub>2</sub> and decaying to PA<sub>1</sub>. We assign PA<sub>2</sub> to a transition from S<sub>2</sub> to a higher excited state and PA<sub>x</sub> to a transition from an intermediate state S<sub>x</sub>. These data therefore show that an intermediate state is involved in the S<sub>2</sub> $\rightarrow$ S<sub>1</sub> IC<sub>21</sub> process in the carotenoids studied so far. After photo-excitation, an initial fast evolution from S<sub>2</sub> to the intermediate state S<sub>x</sub> takes place in  $\approx$ 30–100 fs, depending on the carotenoid; then, energy flows from S<sub>x</sub> to S<sub>1</sub> in a few hundreds fs. These findings extend our previous results on carotenoids with N=11 described in paragraph 3.2.

The experimental data were fitted (solid lines in Fig. 3.9) using a 4-level rate equations model. Table 1 reports the obtained rates. Note that in neurosporene at 520 nm,

Carotenoid	N	k <sub>21</sub> <sup>-1</sup> (fs)		k <sub>10</sub> <sup>-1</sup> (ps)
		$k_{2x}^{-1}$ (fs)	$k_{x1}^{-1}$ (fs)	
m5	5	$45 \pm 5$		2000
Neurosporene	9	$20 \pm 5$	400	20.2
β-carotene	11	$10 \pm 2$	150	9.8
M13	13	$7 \pm 3$	105	2.8
M15	15	<5	$42 \pm 5$	1.1

TABLE 3.1. Rate constants corresponding to the  $S_2 \rightarrow S_x$ ,  $S_x \rightarrow S_1$  and  $S_1 \rightarrow S_0$  relaxation processes for the carotenoids studied. For m5 we considered the rate constant  $k_{21}$  for the direct  $S_2 \rightarrow S_1$  IC<sub>21</sub> process.

around time zero, there is an artefact given by coherent coupling of the pulses, due to spectral overlap of pump and probe; we took into account this feature in the fit, adding a signal proportional to the cross-correlation between pump and probe pulses. Note also that for the longer carotenoids the  $k_{2x}$  rate is so high that it challenges even the temporal resolution of our setup and cannot be determined with high accuracy; nevertheless, a very fast initial energy relaxation process is absolutely required and a three-level model is unable to fit the data.

#### 3.3.2 Ultrafast internal conversion in a short carotenoid

To further investigate the conjugation length dependence of IC<sub>21</sub>, we performed pump-probe experiments on m5, a short  $\beta$ -carotene analogue with N=5, in cyclohexane solution (see Fig. 3.1 for the chemical structure). Due to the short conjugation length, both cw absorption (see Fig. 3.11(a)) and PA bands are blue-shifted with respect to the carotenoids studied so far. We pumped m5 with UV pulses (centered at  $\approx$ 330 nm) (see Fig. 3.11(a)) delivered by the up-conversion stage described in paragraph 2.2.5 and probed the PA<sub>2</sub> band with visible pulses.  $-\Delta T/T$  dynamics at 640 nm wavelength, corresponding to the peak of the PA<sub>2</sub> band, is plotted in Fig. 3.11(b) as circles. We

observed a signal rising with the pump pulse and decaying within  $\approx$ 200 fs to a long-lived plateau, decaying on the nanosecond timescale as shown in Fig. 3.12(a). The same behaviour was observed throughout the visible. Because of its instantaneous risetime, the fast decaying signal has to be assigned to PA<sub>2</sub>, while the long-living plateau is assigned to PA<sub>1</sub>. This is in good agreement with previous measurements on carotenoids with the same conjugation length, reporting <50 fs fluorescence lifetime [Akimoto et al., 2000] and >1 ns S<sub>1</sub> lifetime [Andersson et al., 1995a]. For this carotenoid, no additional intermediate level is needed in order to explain the population dynamics. Fits using a standard three-level scheme (solid line in Fig. 3.11(b)) give us the rate constants for the formation and decay of the S<sub>1</sub> state (see Table 3.1).

Figure 3.12(b) shows the  $S_1 \rightarrow S_0$  IC<sub>21</sub> transition rates, determined by monitoring the decay of the PA<sub>1</sub> band (Fig. 3.12(a)). It clearly shows that the relaxation rates  $k_{10}$  scale as 1/(2N+1), according to the energy gap law and the  $E \propto 1/(2N+1)$  energy scaling law characteristic of linear  $\pi$ -conjugated systems.

Figure 3.12(c) shows the dependence of the  $S_1$  risetime (defined as the time required to form 90% of its population) on the  $\Delta E_{21}$  energy gap between the  $1^1B_u^+$  and  $2^1A_g^-$  electronic levels, as determined by Furuichi et al., 2002. The  $S_1$  risetime shows a strongly non-monotonic dependence on conjugation length, first increasing from  $\approx 160$  fs (N=5) to  $\approx 780$  fs (N=9) and then decreasing again to  $\approx 140$  fs (N=15). This confirms previous results based on fluorescence up-conversion [Akimoto et al., 2000].

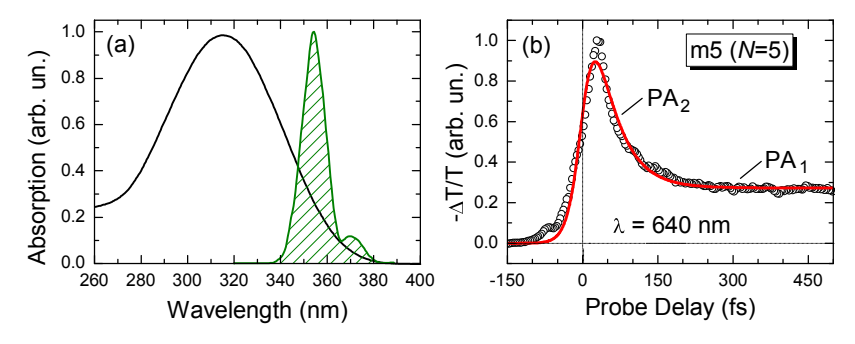


FIG 3.11. (a) Steady-state absorption spectrum (black line) and pump pulse spectrum (green dashed area) of m5. (b) Circles show differential transmission dynamics in m5 at 640 nm probe wavelength. Solid line is a fit obtained using a simple three-state model.

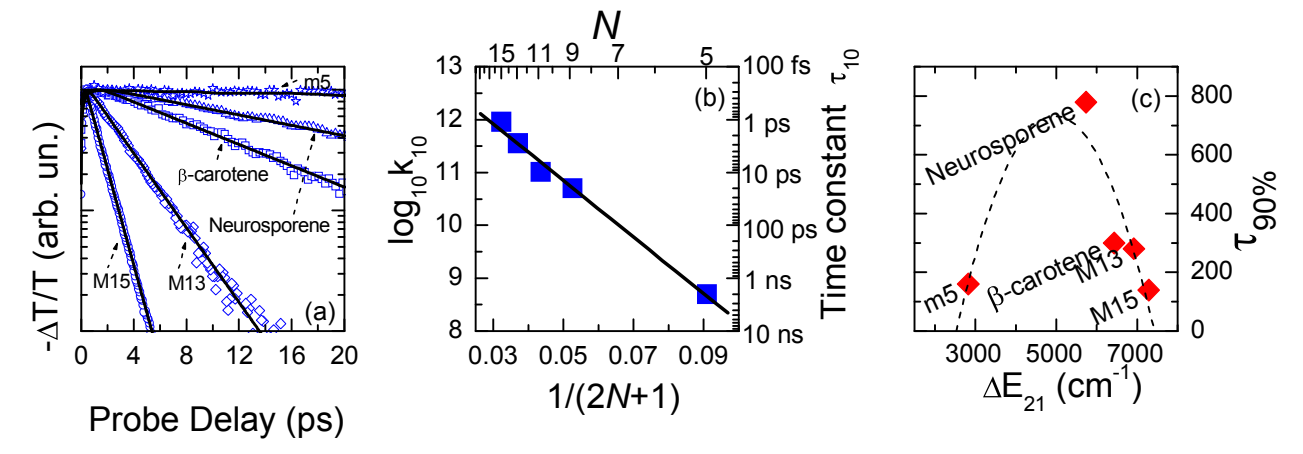


FIG 3.12. (a) Data points show differential transmission dynamics in different carotenoids on a long timescale and logarithmic vertical axis, while solid lines are exponential fits. The obtained IC<sub>10</sub> rate constants are plotted in (b) as a function of conjugation length. (c) Rise time  $\tau_{90\%}$  of S<sub>1</sub> (red diamonds) for the IC<sub>21</sub> process as a function of the  $\Delta E_{21}$  energy gap between the  $1^1B_u^+$  and  $2^1A_g^-$  electronic levels. The dashed line is a guide to the eye.

#### 3.4 Discussion and conclusions

Our experiments allow us to draw the following conclusions: (i) for a short chain carotenoid (N=5) a three-level model is sufficient to describe the  $IC_{21}$  process, while for longer chains (N≥9) an intermediate state is involved in the process; this observation is in agreement with theoretical predictions on energy level structure in carotenoids [Tavan and Schulten, 1986, 1987]. (ii) The overall  $IC_{21}$  rate dependence on chain length changes slope around N=9 (see Fig. 3.10(b)). Combining these observations, we propose that the presence of the intermediate  $S_x$  state, falling within the  $S_2$ - $S_1$  energy gap for the longer carotenoids, makes  $IC_{21}$  a two-step process. The  $S_x$  state observed in our experiments could be the  $1^1B_u$  for neurosporene, while for the longer carotenoids it could be either the  $3^1A_g$  or the  $1^1B_u$  or a mixture of both. The exact spectroscopic assignment of this state requires further investigations. However, it is expected to play a significant role in the energy transfer processes occurring in the early steps of photosynthesis.

In conclusion, we have investigated, with sub-20-fs temporal resolution, the excited state dynamics of six different carotenoids, with conjugation length ranging from N=5 to

N=15. While for N=5 the traditional three-level model is adequate to explain the IC<sub>21</sub> dynamics, for  $N\ge 9$  an intermediate state  $S_x$ , lying between  $S_2$  and  $S_1$ , is needed. Thanks to our improved temporal resolution, we are able to resolve for the first time the extremely fast  $S_2 \rightarrow S_x$  conversion process. The presence of the intermediate state makes IC<sub>21</sub> a two-step process. These results strengthen the need of a 4-level scheme for excited state dynamics in carotenoids and demonstrate its generality.

# Chapter 4

# **Energy Transfer from Carotenoids to Bacterio-Chlorophylls in LH2 complexes**

#### 4.1 Introduction

Purple photosynthetic bacteria are anaerobic prokaryotes which use carotenoids and bacteriochlorophylls (BChls) as their main photosynthetic pigments [Cogdell et al., 1999]. Peripheral Light-Harvesting (LH2) complexes from purple bacteria are excellent model pigment-protein complexes for investigating the basic mechanisms of photosynthetic light harvesting, because their structure is known with high resolution [McDermott et al., 1995; Koepke et al., 1996] and because, unlike in plants and algae, the spectral features of the different pigments are well separated [Cogdell et al., 1999]. For these reasons, over the past decade there has been a great deal of interest in trying to understand the detailed mechanisms involved in carotenoid to chlorophyll singlet-singlet Energy Transfer (ET) reaction [Damjanović et al., 1999; Ritz et al., 2000].

Figure 4.1 shows a schematic of the membrane of a purple photosynthetic bacterium. The first step of photosynthesis is light absorption by the pigments (carotenoids and bacterio-chlorophylls) that are present in the central (LH1) and peripheral (LH2) light-harvesting complexes. Through a cascading effect, absorbed energy is transferred from high- to low-photon-energy absorbing species towards the reaction centre, where charge separation occurs. Some enzymes (cytochromes and quinones) facilitate electron and proton pumping through the membrane. At the end of the photosynthetic chain, ATP is synthesized from ADP in the ATPase.

In this chapter we will deal with the photosynthetic unit, which is the first actor in photosynthesis. It is composed by several LH2 complexes, in a number that depends on

the environment in which the bacterium grows, like temperature and mean luminous intensity, and that can reach 10 units. These structures surround an LH1 complex, larger than LH2, having in its core a reaction centre where electron pumping across the membrane occurs. An example of a photosynthetic unit from *Rhodospirillum molischianum* is shown in Fig. 4.2.

A prototypical purple bacterium is *Rhodospeudomonas acidophila* (*R. acidophila*). Its LH2 complexes are shown in Fig. 4.3 and have a ring structure, consisting of nine

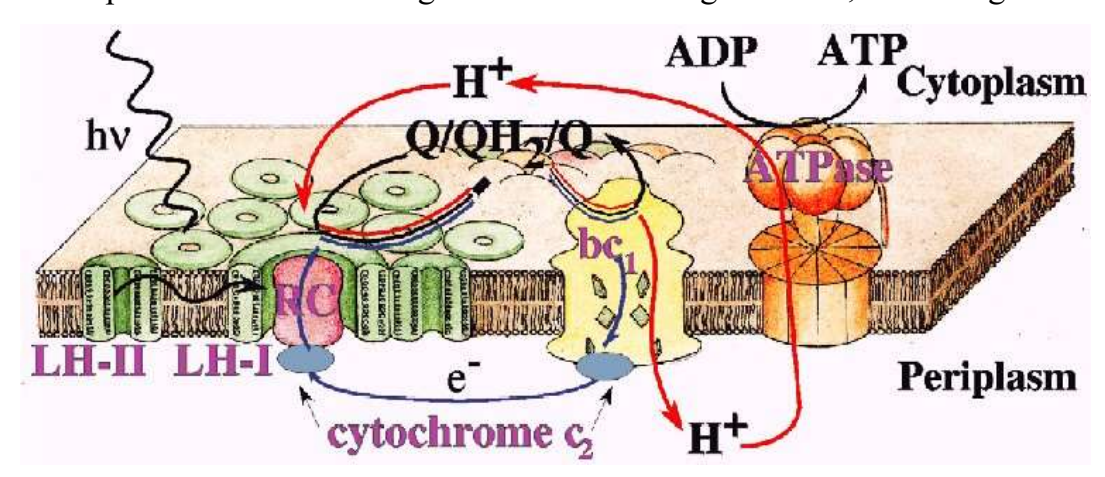


FIG. 4.1. Photosynthetic apparatus of a purple bacteria membrane. Light absorbed by the pigments present in the peripheral LH1 and LH2 complexes (*green*) induce an energy transfer process towards the reaction center (RC, *red*), where charge separation occurs. Cytochromes c<sub>2</sub> and Quinones (Q) facilitate electron and proton pumping through the membrane, which in turn provoke synthesis of ATP from ADP in the ATPase (*orange*).

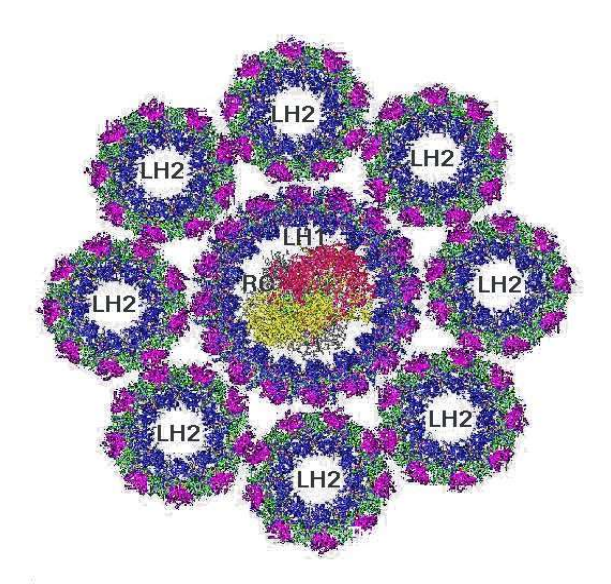


FIG. 4.2. Photosynthetic unit of a purple bacterium, reconstructed thanks to spectrographic and stereochemical data.

monomeric units, each formed by a pair of αβ–apoproteins (cyan and green spiral structures in Fig. 4.3(a) and (b)) which bind, non-covalently, three molecules of BChla and one or two molecules of the carotenoid rhodopin glucoside [McDermott et al., 1995, Papiz et al., 2003]. BChls molecules are organized into two groups, commonly denoted BChl 800 and BChl 850, referring to the position of their low-lying absorption bands. There are 9 BChl 800's (yellow molecules in Fig. 4.3(c) and (d)) which form a ring on the cytoplasmic side of the complex, while there are 18 BChl 850's (purple molecules in Fig. 4.3(c) and (d)) which form a tightly coupled ring near the periplasmic side of the complex. The well-resolved carotenoids (red chain in Fig. 4.3(d)) have an extended S-shape, *all-trans* [Robert and Lutz, 1985] conformation and span the entire depth of the complex, coming into van der Waals contact with both groups of Bchls. In LH2 complexes of *Chromatium purpuratum* (*C. purpuratum*) the absorbing carotenoid is okenone and the BChls absorb at ≈830 nm, while no structure information is yet available.

The BChls have two absorption bands relevant to the ET process: the  $Q_y$  band around 800–850 nm and the  $Q_x$  band around 590 nm. ET to the  $Q_y$  (denoted ET<sub>1</sub> in the following)

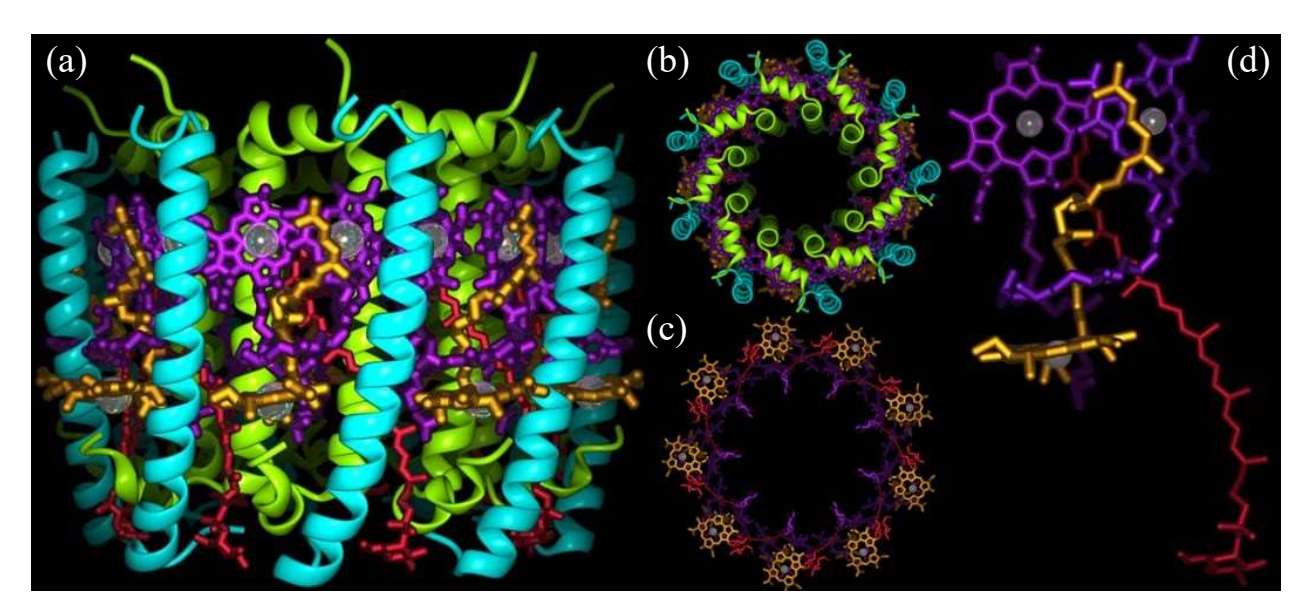


FIG. 4.3. LH2 complex from *R. Acidophila* bacterium. (a) Side view, showing in cyan and green the helixes of the apoproteins; (b) top view from the peripasmatic surface of the membrane; (c) top view from the cytoplasmatic surface of the membrane of the only LH2 pigments; (d) side view of a single pigment unit composed by a carotenoid (in red), two B-850 (in purple) and one B800 (in yellow) bacterio-chlorophylls.

can occur from the carotenoid S<sub>1</sub> state when it is higher in energy, which happens for short carotenoids (typically N≤10) [Zhang et al., 2000b]. On the other hand, the S<sub>2</sub> state of carotenoids can transfer excitation energy to the Qx band (denoted ET2 channel in the following). Given the one to two orders of magnitude shorter lifetime of the S2 carotenoid state as compared to the S<sub>1</sub>, one would expect ET<sub>1</sub> to be the dominant channel; however it has been demonstrated, by fluorescence up-conversion measurements [Ricci et al, 1996; Krueger et al., 1998a; Macpherson et al., 2001] and transient absorption measurements [Macpherson et al., 2001; Papagiannakis et al., 2002], that ET<sub>2</sub> can be active or even predominant in some purple bacteria. The ET<sub>2</sub> process is dominated by the Förster-type mechanism [Damjanović et al., 1999], while the contribution of the electron-exchange (Dexter) energy-transfer mechanism is negligible. However, full Coulombic interaction is usually used in theoretical models. Although the forbidden nature of the S<sub>0</sub>-S<sub>1</sub> transition initially suggested that the Dexter mechanism was responsible for the ET<sub>1</sub> process [Cogdell and Frank, 1987], more detailed calculations [Damjanović et al., 1999; Krueger et al., 1998b] later showed that it is dominated by higher-order Coulombic and polarization interactions.

Given the very fast timescale of both  $IC_{21}$  and  $ET_2$  processes, their full characterization challenges the  $\approx 100$ -fs temporal resolution of standard pump-probe systems; in particular the need of deconvolving the instrumental response from the measured dynamics can lead to ambiguities in the assignment of the underlying processes. The recent availability of pulses with 10–20-fs duration tunable throughout the visible, as we showed in chapters 1 and 2, allows one to probe the early events of energy relaxation in carotenoids with unprecedented temporal resolution. In this chapter we describe experimental results on the early steps of excited state dynamics of two carotenoids, okenone and rhodopin glucoside, in solution and inside the LH2 complex of two purple bacteria, *C. purpuratum* and *R. acidophila*, respectively. Exploiting the improved temporal resolution, we can follow the details of the  $IC_{21}$  process; by comparing its dynamics inside and outside the LH2 complex, we are able to directly evaluate the efficiency of the  $ET_2$  process. By subsequently studying the  $IC_{10}$  process we can also evaluate the role of  $ET_1$ .

In chapter 3 we have shown that in several carotenoids  $IC_{21}$  is a two-step process involving an intermediate  $S_x$  state ( $1^1B_{u}^-$  state). The initial  $S_2 \rightarrow S_x$  conversion takes place within 30–100 fs and is best observed in the near IR where the Photo-induced Absorption (PA) bands of  $S_2$  and  $S_x$  are located; in the LH2 complexes these bands overlap with the Photo-Bleaching (PB) and PA bands of BChl. This spectral congestion of signals coming from different species makes it very hard to detect the presence of an intermediate state. Therefore, in this study, similarly to what already done by Zhang et al. [Zhang et al., 2001b], we will refer to the  $S_2$  state as a superposition of the  $1^1B_u^+$  and  $1^1B_u^-$  states. For this reason, the model used for the fitting procedures used throughout this chapter will differ from the one described in section 3.2.2 by the fact that it will take into account only three electronic levels of carotenoids ( $S_2$ ,  $S_1$  and  $S_0$ ) with the  $\tau_{21}$  and  $\tau_{10}$  internal conversion time constants describing  $IC_{21}$  and  $IC_{10}$  internal conversion processes.

## 4.2 Experimental Results

# 4.2.1 Sample preparation

Okenone, rhodopin glucoside and the LH2 complexes (*C. purpuratum* and *R. acidophila*) were isolated and purified as previously described [Macpherson et al., 2001; Cogdell and Hawthornthwaite, 1991; Cogdell et al., 1990]. Their integrity and purity were checked spectrophotometrically and by thin layer chromatography on silica gel plates.

## 4.2.2 Ultrafast dynamics of okenone in solution

The goal of this study was to obtain the carotenoid-to-BChl ET rates from the direct comparison of early dynamics of IC in carotenoids in solution and inside the LH2 complex. For a meaningful comparison, it is essential to choose the solvent that best mimics the protein environment. To this purpose we performed a preliminary extensive study of the carotenoid okenone in various solvents. It is well known that the energy of the  $S_0$ – $S_2$  transition in carotenoids depends on the refractive index n of the solvent and it shifts almost linearly with its polarizability R=( $n^2$ -1)/( $n^2$ +2) [Macpherson and Gillbro, 1998], both for

polar and nonpolar solvents. Figure 4.4 shows steady-state absorption of LH2 complex from *C. Purpuratum* and its carotenoid (okenone) in various solvents: acetone (R=0.219), cyclohexane (R=0.256), benzyl alcohol (R=0.314) and carbon disulfide ( $CS_2$ , R=0.354). Carotenoid absorption extends in the visible region from  $\approx$ 400 nm to  $\approx$ 600 nm; BChl  $Q_y$  absorption has two peaks in the NIR region at 800 nm and 830 nm, while BChl  $Q_x$  band is partially visible around 590 nm. As expected, a clear trend in the position of the  $S_2$  state energy was seen in okenone in solution: the transition peak moved from  $\approx$ 486 nm to  $\approx$ 520 nm going from low to high polarizability solvents. Best superposition with the carotenoid absorption inside the LH2 complex was found for  $CS_2$ .

Another important parameter which should be taken into account for choosing the right solvent is its polarity  $P=(\epsilon-1)/(\epsilon+2)$ . In particular, while for standard  $\pi$ -conjugated carotenoids the polarity of the solvent has only a small effect on their excited states, carbonyl carotenoids, having a conjugation extension to a C=O terminal group, exhibit solvent-dependent relaxation kinetics [Bautista et al., 1999, Frank et al., 2000]. It has been previously observed in peridinin carbonyl carotenoid, for example, that S<sub>1</sub> lifetime in polar and hydrogen bonding solvents is much shorter than in nonpolar ones. The rapid decrease of S<sub>1</sub> lifetime with increasing polarity has been explained in terms of either a

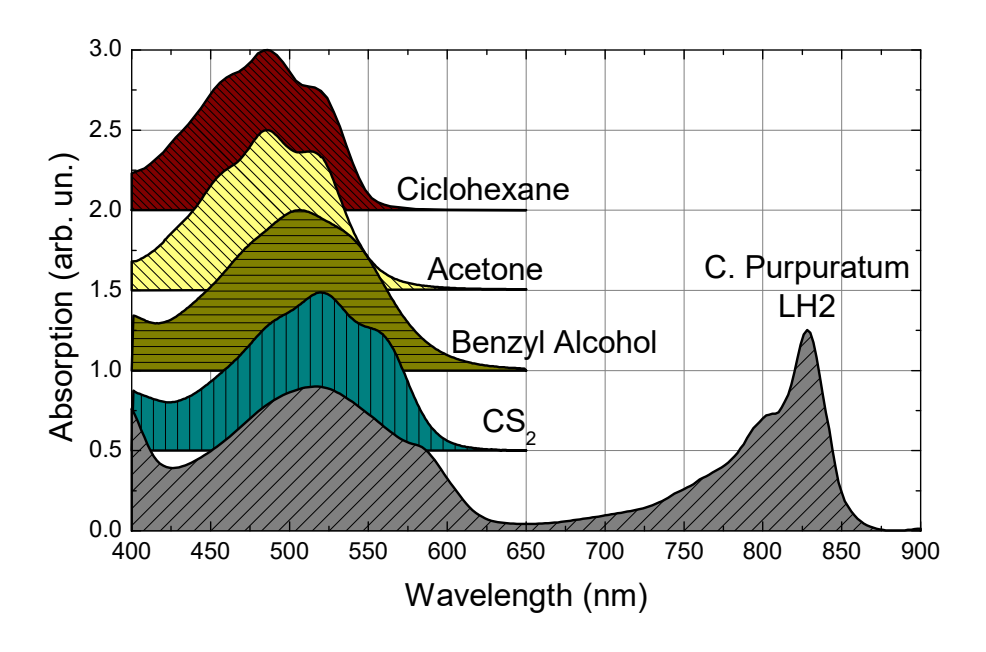


FIG. 4.4. Steady-state absorption spectra of LH2 complex of *C. purpuratum* and of okenone in acetone, benzyl alcohol, CS<sub>2</sub> and cyclohexane solution.

conformational change from cis to all-*trans* [Shima et al., 2003] or an increase in the intramolecular charge transfer (ICT) character, strongly coupled to the S<sub>1</sub> state [Zigmantas et al., 2003].

Fig. 4.5 shows - $\Delta$ T/T spectra of okenone in various solvents for 500 fs pump-probe delay. A broad PA band in the visible is observed (PA<sub>1</sub> band), peaking at 590–650 nm, depending on the solvent. The PA<sub>1</sub> band is a well known feature of carotenoids, assigned to the S<sub>1</sub> $\rightarrow$ S<sub>n</sub> absorption and thus providing a signature of population of the dark S<sub>1</sub> state. The transmission increase on the short wavelength side of the spectra is due to Photo-Bleaching (PB) of the ground state. Pump-probe dynamics at the wavelength corresponding to the peak of the PA<sub>1</sub> band are plotted in Fig. 4.6 over short and long timescales. Formation and decay of this band occur in  $\approx$ 500 fs and  $\approx$ 20 ps, respectively. This signal reveals the sequential steps of the IC<sub>21</sub> and IC<sub>10</sub> processes. Exponential fits using the 3-level model previously described have also been plotted in Fig. 4.6 with indication of the extracted time constants  $\tau_{21}$  and  $\tau_{10}$  for the IC<sub>21</sub> and IC<sub>10</sub> processes.

When moving from nonpolar (cyclohexane, P=0.254, and CS<sub>2</sub>, P=0.354) to polar (benzyl alcohol, P=0.801, and acetone, P=0.868) solvents, the okenone S<sub>1</sub> lifetime remains nearly unchanged (4.2–4.65 ps, see Fig. 4.6(b)). This result follows the trend found for other carbonyl carotenoids [Zigmantas et al., 2004], indicating less dependence of IC<sub>10</sub> dynamics on solvent polarity when increasing the number of conjugated double bonds (N). While for peridinin (N=7) S<sub>1</sub> lifetime has a one-order-of-magnitude change moving from polar to nonpolar solvents, in spheroidenone (N=10) it does not depend on solvent polarity. Okenone, having 11 conjugated double bonds (10 on the linear backbone and 1 located at a terminal ring, see Fig. 4.5 for the chemical structure), has the same behavior. The reason could be found in its small S<sub>0</sub>–S<sub>1</sub> energy gap, that makes the S<sub>0</sub>–S<sub>1</sub> coupling strong enough, even in nonpolar solvents, to give an S<sub>1</sub> lifetime which is almost equal to non-carbonyl linear carotenoids with 11 C=C bonds:  $\approx$ 4 ps in lycopene [Fujii et al., 2003; Polli et al., 2003],  $\approx$ 4.5 ps in rhodopin glucoside [Macpherson et al., 2001].

Let us now consider  $S_2$  lifetime (Fig. 4.6(a)). The results are in good agreement with previous studies on  $\beta$ -carotene [Macpherson and Gillbro, 1998]: in nonpolar solvents there is a significant dependence of  $IC_{21}$  rate on polarity ( $\tau_{21} = 130$  fs in cyclohexane and 95 fs

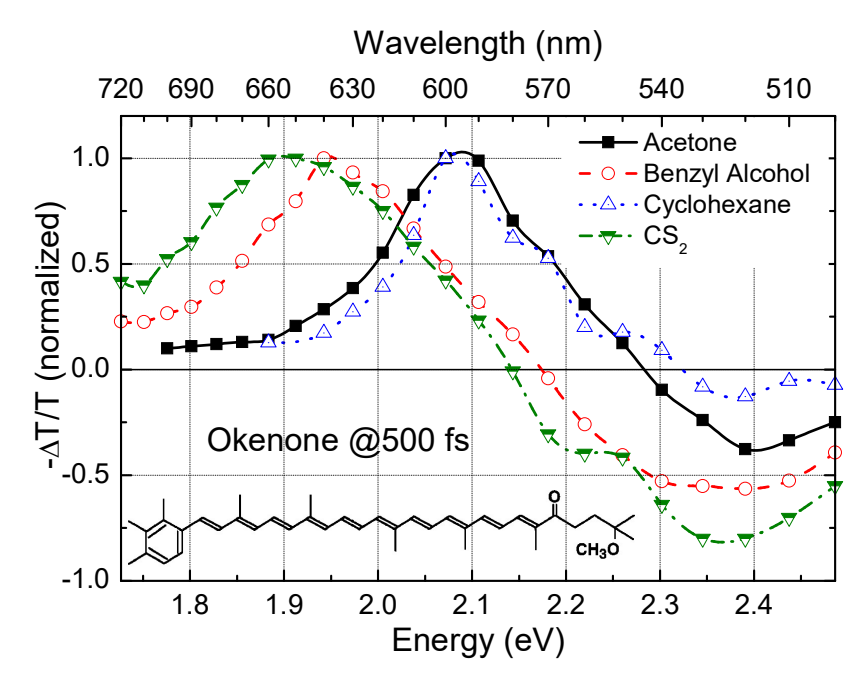


FIG. 4.5. Chemical structure and transient absorption spectra of okenone in different solvents at ≈500 fs probe delay.

in CS<sub>2</sub>), while in polar ones there is a much weaker change ( $\tau_{21}$  = 110 fs in acetone and 100 fs in benzyl alcohol).

All the previous results can be put together into a consistent picture. We can conclude for okenone that solvent polarity does not considerably affect  $S_1$  energy, so that  $IC_{10}$  process occurs within the same timescale; on the other hand, solvent polarizability can shift the  $S_2$  energy. Due to these considerations, the best solvent to reproduce the *in vivo* environment for okenone is  $CS_2$  and it will be used in the following study, as already done by another group [Andersson et al., 1996].

 $\Delta T/T$  spectra of okenone in CS<sub>2</sub> at different delays following photo-excitation are shown in Fig. 4.7. The rapid formation and subsequent decay of the PA<sub>1</sub> band peaking at 650 nm can be observed in detail. The increased transmission present on the short wavelength side of the spectra is due a superposition of PB of the ground state (530–580 nm) and, for probe delays up to  $\approx 100$  fs, stimulated emission (SE) from the S<sub>2</sub> state (580–630 nm).

To better time-resolve the  $IC_{21}$  and  $IC_{10}$  processes, we plot in Fig. 4.8 (thin lines) the  $\Delta T/T$  dynamics at selected probe wavelengths. Exponential fits at the absorption peak (650

nm, plotted in Fig. 4.8 as thick lines) enable us to extract the time constants for the IC<sub>21</sub> and IC<sub>10</sub> decay processes of  $\tau_{21}$ =95 fs and  $\tau_{10}$ =4.2 ps, respectively. Note that this is the first accurate measurement of  $\tau_{21}$  in okenone and that the value of  $\tau_{10}$  obtained in our experiments significantly differs from 8 ps found by Andersson et al., 1996.

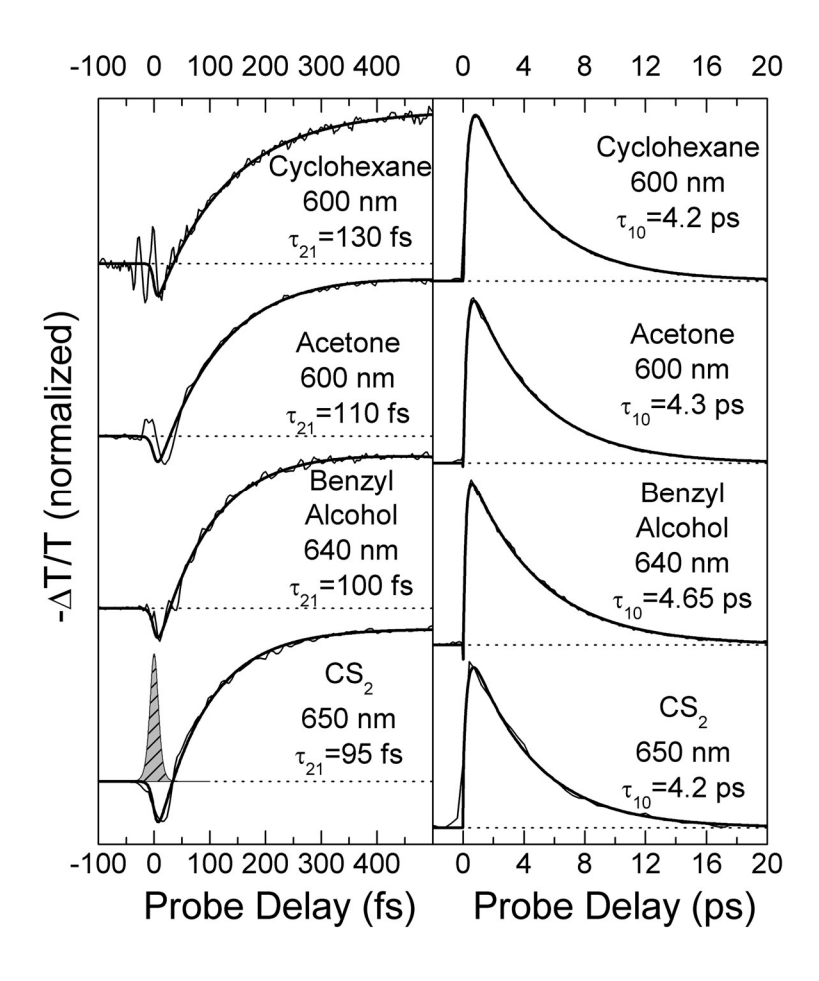


FIG. 4.6. Differential transmission dynamics (thin solid lines) of okenone in different solvents, at the probe wavelength corresponding to the peak of the PA<sub>1</sub> band. Thick solid lines are fits obtained using the model described in the text. Extracted time constants for the  $S_2 \rightarrow S_1$  and  $S_1 \rightarrow S_0$  IC processes are also indicated. Pump-probe cross-correlation is shown as dashed area.

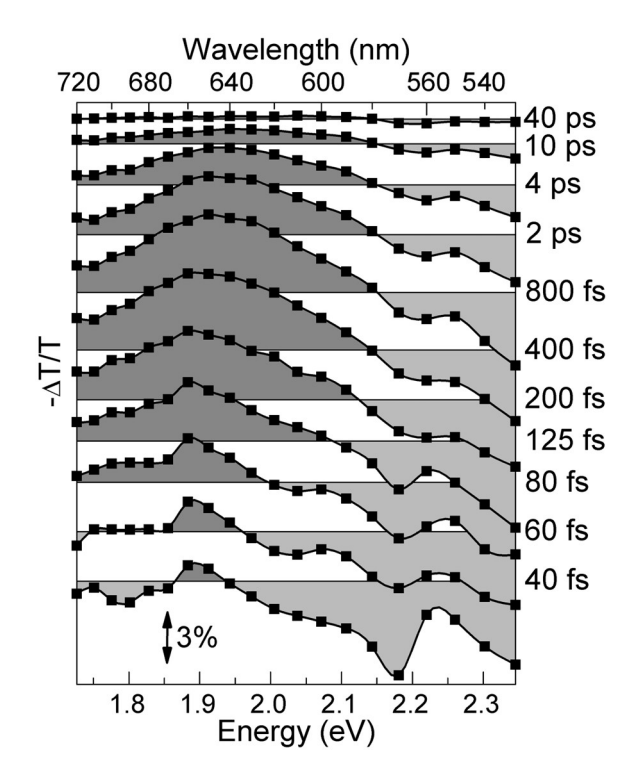


FIG. 4.7. Transient absorption spectra of okenone in CS<sub>2</sub> solution at different selected pump-probe delays.

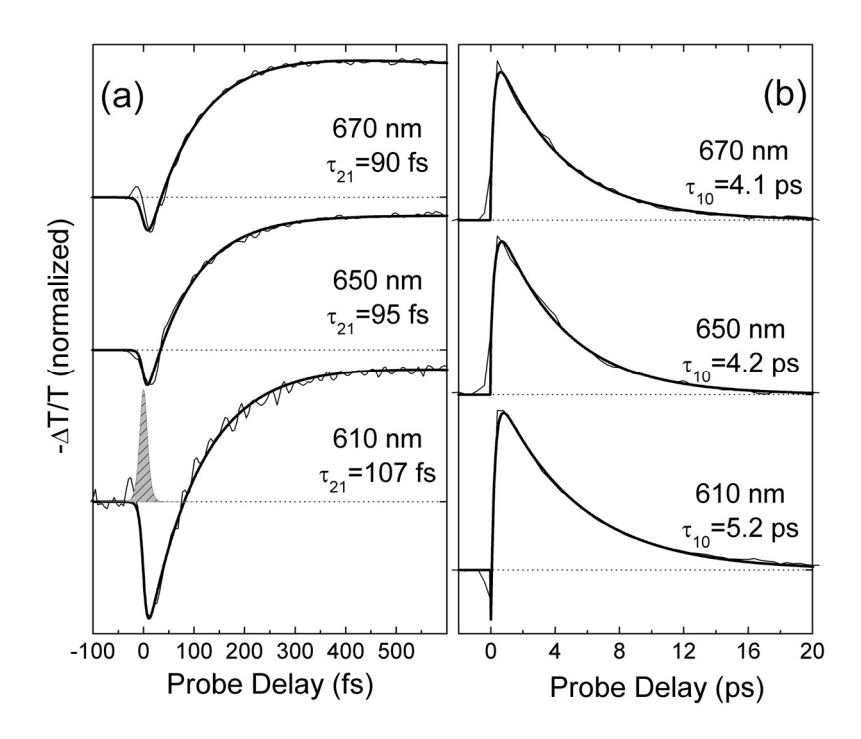


FIG. 4.8. Differential transmission dynamics (thin solid lines) of okenone in CS<sub>2</sub> solution, at different selected probe wavelengths. Thick solid lines are fits obtained using the model described in the text. Extracted time constants for the  $S_2 \rightarrow S_1$  and  $S_1 \rightarrow S_0$  IC processes are also indicated. Pump-probe cross-correlation is shown as dashed area.

There is however a significant wavelength dependence of the dynamics of the build-up and decay of PA<sub>1</sub>: faster at the red side ( $\tau_{21}$ =90 fs and  $\tau_{10}$ =4.1 ps at 670 nm) and slower at the blue edge ( $\tau_{21}$ =107 fs and  $\tau_{10}$ =5.2 ps at 610 nm). The same behaviour is seen in the PA<sub>1</sub> spectra, which change in shape during the IC processes. Figure 4.9 shows the evolution of the  $\Delta T/T$  spectra at different delays, which have been normalized in order to clearly reveal this feature. A blue shift in time is observed: the PA<sub>1</sub> peak moves from 660 nm at 200 fs delay to 640 nm at 8 ps delay, with a simultaneous ≈10 nm blue shift of the isosbestic point. This evolution can be attributed to different phenomena: (i) intra-band vibrational cooling associated to dissipation of the excess energy (≈5000 cm<sup>-1</sup>) initially deposited in S<sub>1</sub>, typically occurring on the ≈0.5 ps time scale [Cerullo et al., 2001; Billsten et al., 2002; Wohlleben et al., 2003; Lanzani et al., 2004]; (ii) vibrational energy redistribution in the hot ground state, typically occurring on the 5–15 ps time scale [Yoshizawa et al., 2001], which creates a photo-induced, red-shifted replica of the steady-state absorption; (iii)

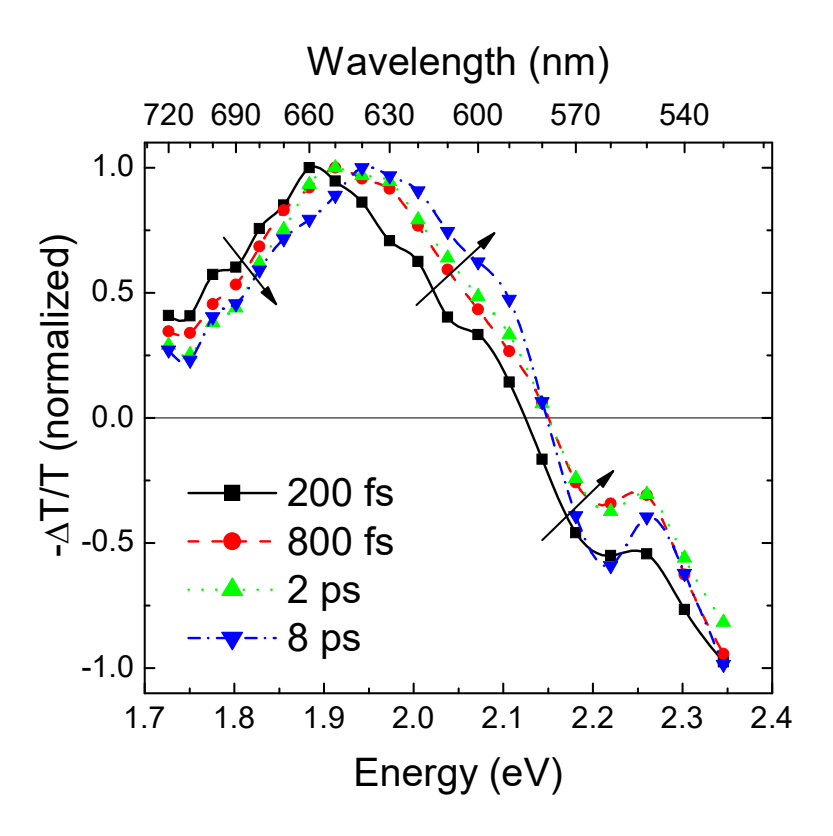


FIG. 4.9. Normalized transient absorption spectra of okenone in CS<sub>2</sub> solution at different selected pump-probe delays.

conformational relaxation from a twisted configuration –created by the photo-excitation—to the all-*trans* form during either the  $IC_{21}$  [de Weerd et al., 2002] or the  $IC_{10}$  process [Polívka et al., 2001].

# 4.2.3 Ultrafast dynamics of okenone inside the LH2 complex of *C. purpuratum*

Figure 4.10 shows the  $\Delta T/T$  spectra of the LH2 complex of bacterium *C. purpuratum*, upon resonant photoexcitation of the okenone chromophore. The visible pump pulses also weakly excite the  $Q_x$  band of the BChls. Again we observe the formation of the PA<sub>1</sub> band (reflecting the IC<sub>21</sub> process) and its subsequent decay (reflecting IC<sub>10</sub>). The increased transmission seen at the blue side (580–500 nm) is due to PB and SE. Within the protein environment, the PA<sub>1</sub> band of the carotenoid peaks at 620 nm, i.e.  $\approx$ 20 nm red-shifted with respect to the solution. We observe a faster risetime of the PA<sub>1</sub> band, which is essentially completed within 300 fs. Relaxation of S<sub>1</sub> back to the ground state also occurs on a slightly

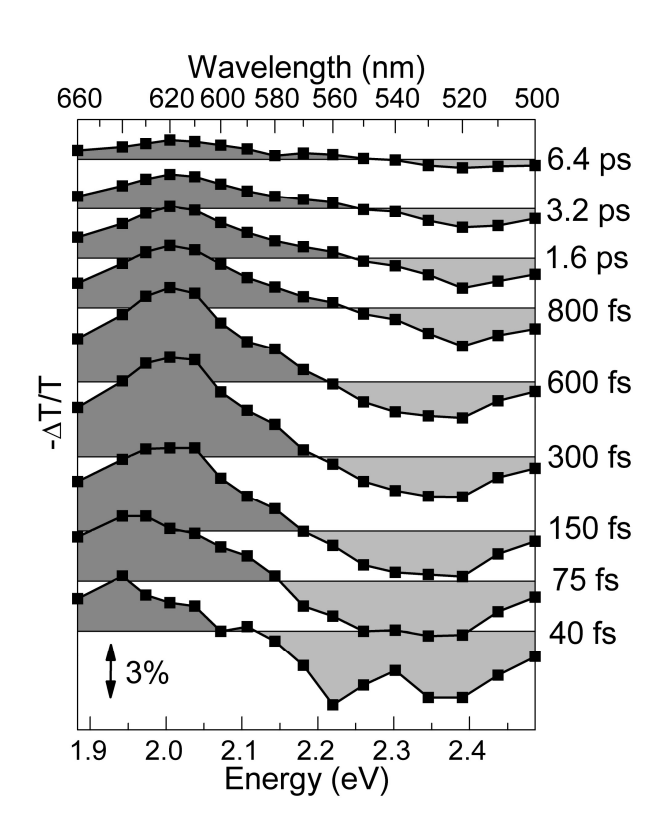


FIG. 4.10. Transient absorption spectra of LH2 complex from *C. purpuratum* at different selected pump-probe delays.

faster timescale compared to the carotenoid in solution. The faster PA<sub>1</sub> buildup and decay is confirmed by following the detailed kinetics at selected probe wavelengths (see Fig. 4.11). In this case, exponential fitting at the PA<sub>1</sub> peak gives IC<sub>21</sub> and IC<sub>10</sub> time constants of  $\tau_{21}$ =85 fs and  $\tau_{10}$ =3.8 ps. We also observe a blue-shift of the PA<sub>1</sub> band on the picosecond timescale as already seen in solution. Note that the fast decay component of S<sub>1</sub> ( $\tau_{10}$  =400–500 fs) previously reported [Andersson et al., 1996] is not present in our measurements.

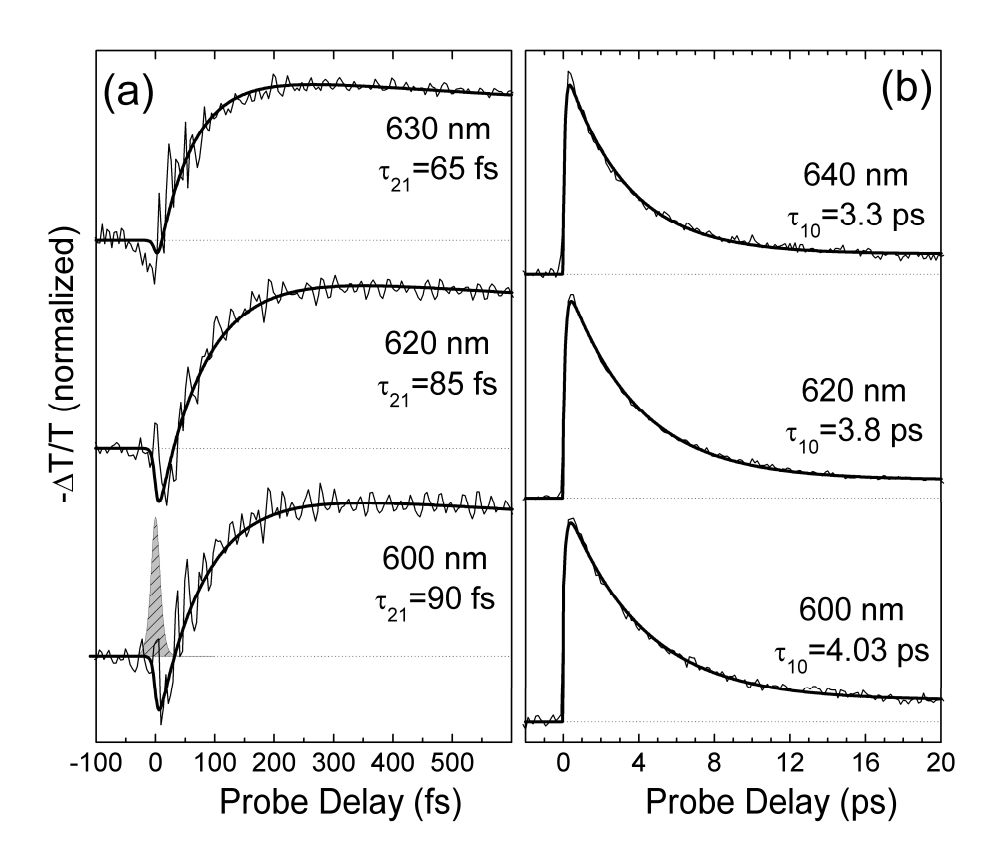


FIG. 4.11. Differential transmission dynamics (thin solid lines) of LH2 complex from C. purpuratum, at different selected probe wavelengths. Thick solid lines are fits obtained using the model described in the text. Extracted time constants for the  $S_2 \rightarrow S_1$  and  $S_1 \rightarrow S_0$  IC processes are also indicated. Pump-probe cross-correlation is shown as dashed area.

#### 4.2.4 Ultrafast dynamics of rhodopin glucoside in solution

Ultrafast dynamics of the LH2 system of *R. acidophila*, together with its carotenoid rhodopin glucoside, has already been studied by several groups [Macpherson et al., 2001; Wohlleben et al., 2003; Rondonuwu et al., 2004]. Our results partially confirm those findings, but also provide some new insights into the early events of its energy relaxation.

Fig. 4.12 shows steady-state absorption spectra of rhodopin glucoside and LH2 complex from R. acidophila. BChl has the  $Q_x$  absorption band at  $\approx 590$  nm and the two  $Q_y$  peaks at 800 nm and 850 nm. Carotenoid absorption is in the green-blue region and has a marked vibronic structure, with the 0–0 transition peaking at  $\approx 524$  nm in the LH2 complex. Absorption of rhodopin glucoside in benzyl alcohol and acetone solution is also presented in Fig. 4.12, showing the 0–0 line at 510 and 530 nm, respectively. It can be seen that benzyl alcohol mimics well the protein environment both for the absorption peak and its vibronic structure.

 $-\Delta T/T$  spectra of rhodopin glucoside at the probe delay corresponding to the maximum signal from  $S_1$  ( $\approx 600$  fs) are shown if Fig. 4.13. PB of the ground state matches steady-state absorption of the carotenoid: it extends up to 520 nm when dissolved in

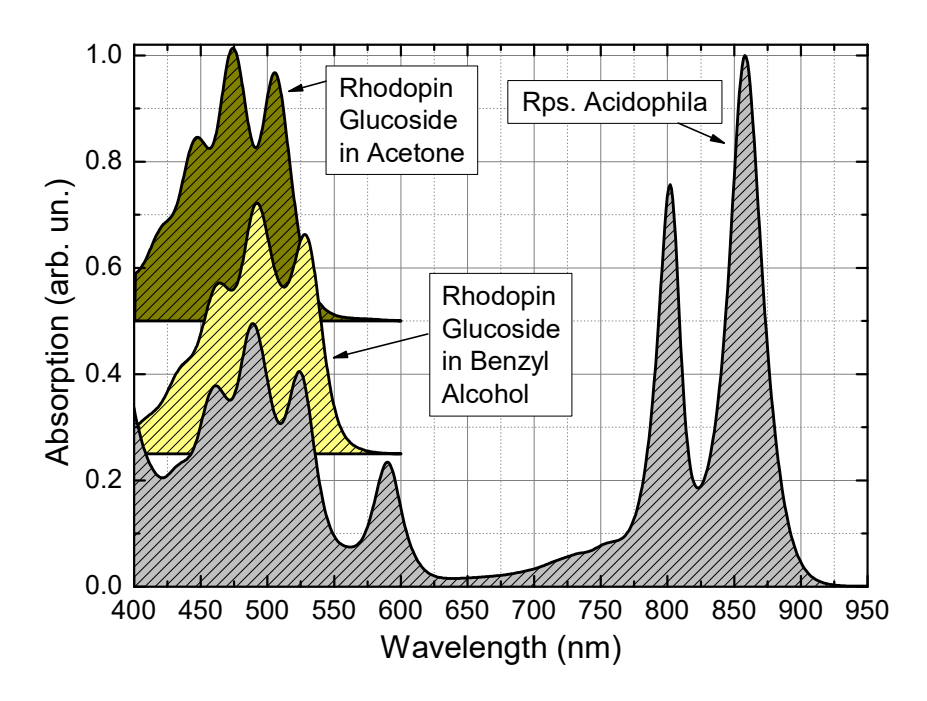


FIG. 4.12. Steady-state absorption spectra of rhodopin glucoside in acetone and benzyl alcohol solution and of LH2 complex of *R. acidophila*.

acetone and 540 nm in benzyl alcohol. The broad PA<sub>1</sub> band in the visible peaks at 560 nm in acetone and 590 nm in benzyl alcohol. Pump-probe dynamics at these wavelengths are shown in Fig. 4.14. Both formation (Fig. 4.14(a)) and decay (Fig. 4.14(b)) of the PA<sub>1</sub> signal occur faster in acetone than in benzyl alcohol. S<sub>1</sub> decay in acetone is even faster than for LH2 (see later).

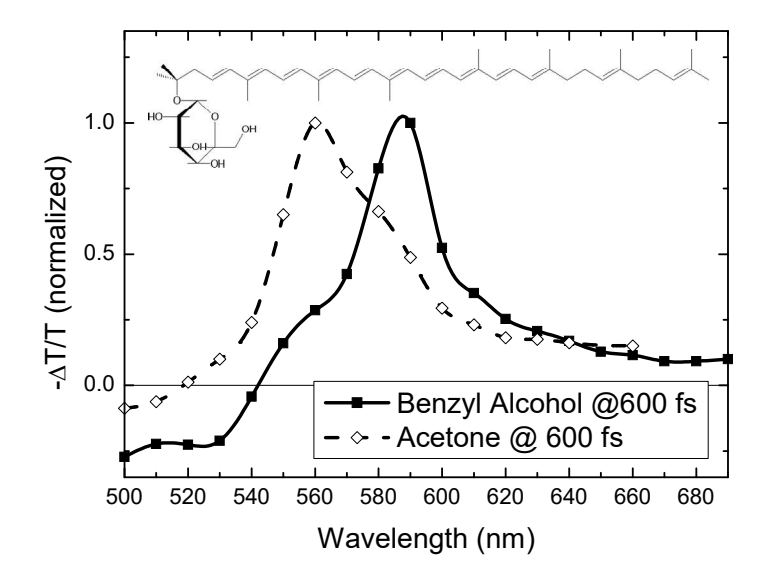


FIG. 4.13. Chemical structure and transient absorption spectra of rhodopin glucoside in acetone and benzyl alcohol solution at ≈600 fs probe delay.

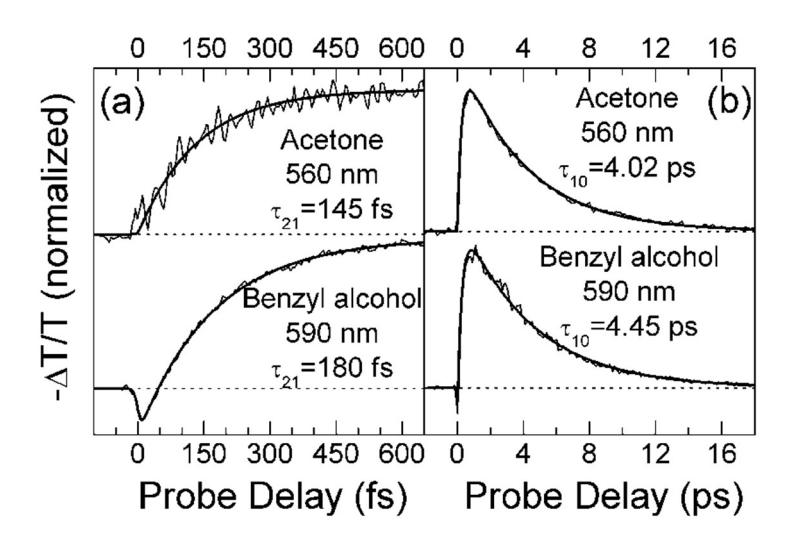


FIG. 4.14. Differential transmission dynamics (thin solid lines) of rhodopin glucoside in different solvents, at the probe wavelength corresponding to the peak of the PA<sub>1</sub> band. Thick solid lines are fits obtained using the model described in the text. Extracted time constants for the  $S_2 \rightarrow S_1$  and  $S_1 \rightarrow S_0$  IC processes are also indicated.

-ΔT/T spectra of rhodopin glucoside in benzyl alcohol are shown in Fig. 4.15 for different delays following photo-excitation. Once again, we clearly time-resolve formation and decay of the PA<sub>1</sub> band peaking at 590 nm. At early probe delays, a broad SE from S<sub>2</sub> appears throughout the visible region, rapidly giving way to the formation of the PA<sub>1</sub> band, completed in  $\approx$ 600 fs. Ground-state PB shows up in the green-blue region ( $\lambda$ <540 nm). Exponential fits of the measured pump-probe time trace (Fig. 4.16) at the absorption peak ( $\lambda$ =590 nm) provide the following time constants for the IC<sub>21</sub> and IC<sub>10</sub> processes:  $\tau$ <sub>21</sub>=180 fs and  $\tau$ <sub>21</sub>=4.3 ps.

Blue-shift in time of the PA<sub>1</sub> band and of the isosbestic point, previously observed in okenone, is also present in rhodopin glucoside, as evident both in the time evolution of the spectra (Fig. 4.15) and in the wavelength dependence of the dynamics. Figure 4.16, in fact, shows faster IC dynamics at the red edge of the PA<sub>1</sub> band (600 nm:  $\tau_{21}$ =125 fs and  $\tau_{21}$ =4.2 ps) than at the blue edge (580 nm:  $\tau_{21}$ =200 fs and  $\tau_{21}$ =4.5 ps).

Our results are in fairly good agreement with those reported by Macpherson et al., 2001, who found a lifetime of the  $S_2$  state, determined by fluorescence up-conversion, of  $124\pm8$  fs, and a lifetime of the  $S_1$  state of  $4.8\pm0.2$  ps.

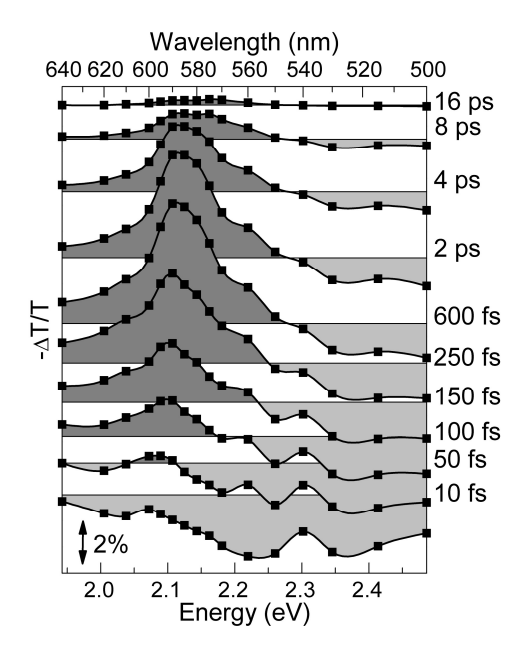


FIG. 4.15. Transient absorption spectra of rhodopin glucoside in benzyl alcohol solution at different selected pump-probe delays.

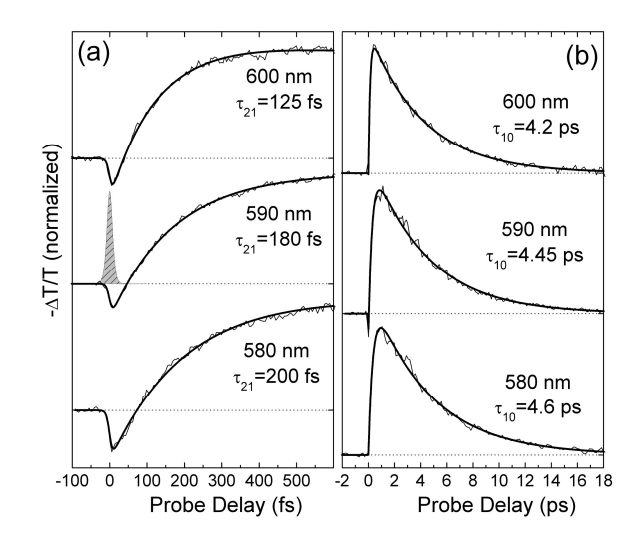


FIG. 4.16. Differential transmission dynamics (thin solid lines) of rhodopin glucoside in benzyl alcohol solution, at different selected probe wavelengths. Thick solid lines are fits obtained using the model described in the text. Extracted time constants for the  $S_2 \rightarrow S_1$  and  $S_1 \rightarrow S_0$  IC processes are also indicated. Pump-probe cross-correlation is shown as dashed area.

# 4.2.5 Ultrafast dynamics of rhodopin glucoside inside the LH2 complex of R. acidophila

Fig 4.17 shows a sequence of - $\Delta$ T/T spectra of the LH2 complex of bacterium *R. acidophila*, upon resonant photoexcitation of the rhodopin glucoside chromophore. Also in this case the visible pump pulses weakly excite the Q<sub>x</sub> band of the BChls. At early pump-probe delays we observe a broad SE band from S<sub>2</sub> which rapidly gives way to the buildup of the PA<sub>1</sub> band, while PB is left over below ≈540 nm. Within the protein environment, the PA<sub>1</sub> band is blue-shifted by less than 10 nm with respect to the solution. PB of the BChl Q<sub>x</sub> absorption burns a hole in the PA<sub>1</sub> band that is observable around 590 nm. We observe a much faster risetime of the PA<sub>1</sub> band, which is essentially completed within 250 fs, with a subsequent slightly quicker relaxation of S<sub>1</sub> back to the ground state as compared to the carotenoid in solution. The faster PA<sub>1</sub> build-up and decay are confirmed by following the detailed kinetics at selected probe wavelengths, plotted in Fig. 4.18. In this case, exponential fitting gives  $\tau_{21} = 77$  fs and  $\tau_{10} = 4.1$  ps. However, a small residual signal was still present after 40 ps, due to the triplet  $1^3$ Bu<sup>-</sup> state of the carotenoid, which has been previously observed in the 530–570 nm region [Wohlleben et al., 2003; Rondonuwu et al.,

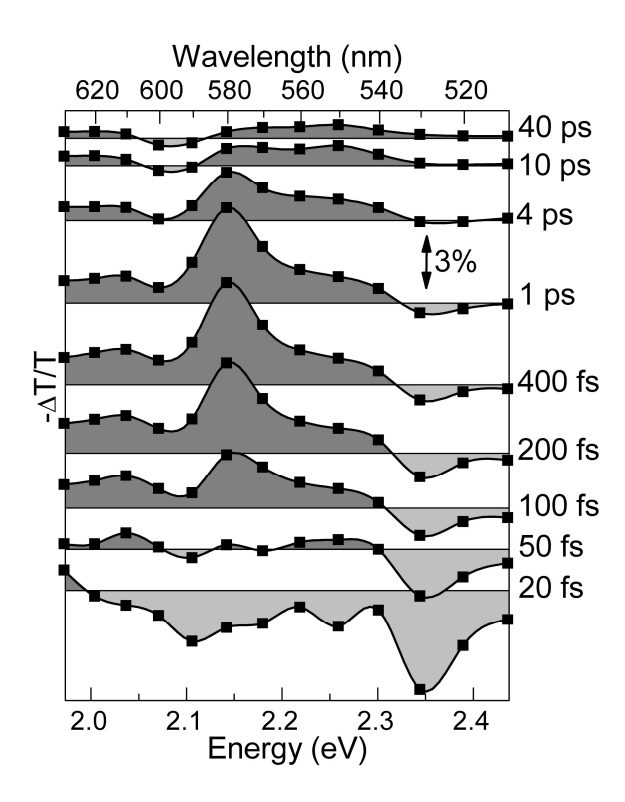


FIG. 4.17. Transient absorption spectra of the LH2 complex of *R. acidophila* at different selected pump-probe delays.

2004]. Fast intersystem crossing to triplet states on the picosecond timescale is a recently discovered relaxation pathway for carotenoids bound to LH complexes [Gradinaru et al., 2001; Papagiannakis et al., 2002].

Note that we observe slightly less pronounced wavelength dependence of  $PA_1$  buildup dynamics in the LH2 complex as compared to the carotenoid in solution, probably due to the speedup of the process. The usual wavelength dependence of  $S_1$  relaxation (slower decay in the blue than in the red) is retained also in the LH2 complex.

Note that our data are in good agreement with the results by Macpherson et al., 2001, reporting an  $S_2$  lifetime of the carotenoid in the LH2 complex, measured by fluorescence upconversion, of  $57\pm2$  fs. On the other hand, Rondonuwu et al., 2004, using pump-probe spectroscopy with 160 fs instrumental response width, proposed a quite different relaxation pathway for the LH2 complex of R. acidophila. This involves initial energy relaxation to the  $1^1B_u^-$  state with time constant of  $\approx 80$  fs and subsequent delayed formation of the  $S_1$  state, with a time constant of  $\approx 400$  fs. Our measurements do not present evidence of this delayed formation of the  $S_1$  state.

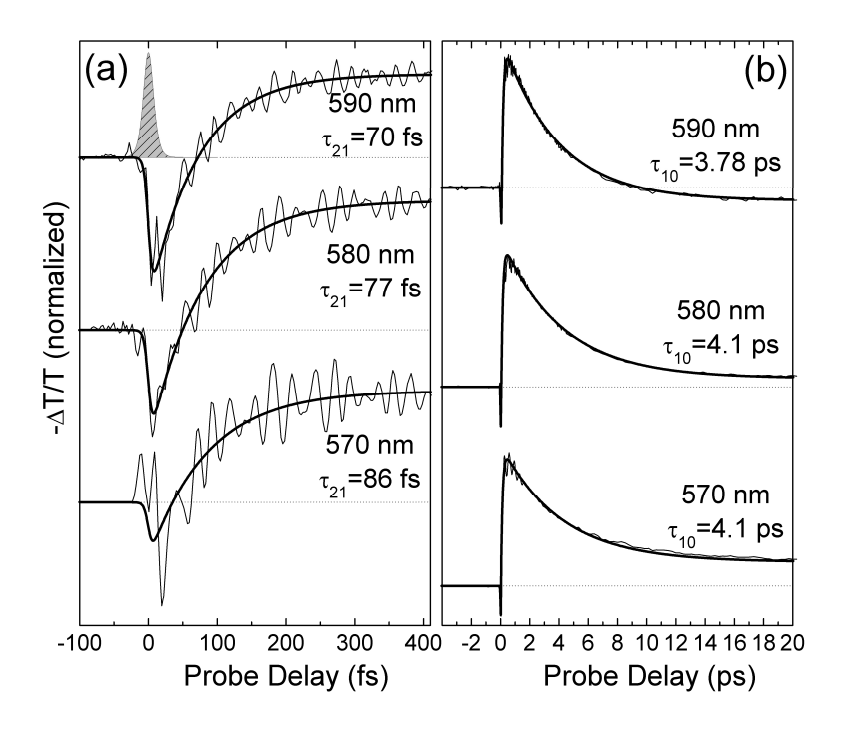


FIG. 1.18. Differential transmission dynamics (thin solid lines) of the LH2 complex of R. acidophila, at different selected probe wavelengths. Thick solid lines are fits obtained using the model described in the text. Extracted time constants for the  $S_2 \rightarrow S_1$  and  $S_1 \rightarrow S_0$  IC processes are also indicated. Pump-probe cross-correlation is shown as dashed area.

#### 4.3 Discussion and conclusions

## 4.3.1 Carotenoid-to-BChl energy transfer

The shortening of  $S_2$  and  $S_1$  lifetimes of okenone and rhodopin glucoside in their corresponding LH2 complexes is due to the opening of a new relaxation channel, in addition to internal conversion  $IC_{21}$  and  $IC_{10}$ : energy transfer  $ET_2$  and  $ET_1$  to the BChls (see Fig. 4.19). In order to estimate these rates, we must compare  $S_2$  and  $S_1$  lifetimes of carotenoids in solution and inside LH2 complex. While, in solution,  $S_2$  and  $S_1$  electronic states decay with internal conversion rates  $k_{21}$  and  $k_{10}$ , respectively, inside the LH2 complex the overall deactivation rates become  $(k_{21}+k_{ET2})$  and  $(k_{10}+k_{ET1})$ , respectively. The resulting rate equations governing the process are then:

$$\begin{split} \frac{dN_2}{dt} &= -k_{21}N_2 - k_{ET2}N_2 = -(k_{21} + k_{ET2})N_2 \quad \Rightarrow \quad N_2(t) = N_{20} \exp[-(k_{21} + k_{ET2})t]; \\ \frac{dN_1}{dt} &= k_{21}N_2 - k_{10}N_1 - k_{ET1}N_1. \end{split}$$

Let us now show that, in the simple case of  $(k_{10}+k_{ET1}) \ll k_{21}$  (i.e. when  $S_1$  lifetime is much higher than  $S_2$  lifetime), the  $S_1$  formation time is governed by the overall  $(k_{21}+k_{ET2})$  rate constant. In this case, we can write:

$$\frac{dN_1}{dt} = k_{21}N_2 - k_{10}N_1 - k_{ET1}N_1 \cong k_{21}N_2 \implies$$

$$\Rightarrow N_1(t) = k_{21}\int_{-\infty}^t N_2(t') = \frac{k_{21}N_{20}}{k_{21}k_{ET2}} exp[-(k_{21} + k_{ET2})t]$$

In conclusion, by monitoring the  $S_1$  formation time of carotenoids inside the LH2 complex (by means of the  $PA_1$  signal, see Fig. 4.19) it is possible to derive the factor ( $k_{21}+k_{ET2}$ ). By subtracting the  $k_{21}$  rate constant measured in the carotenoid in solution one obtains the  $k_{ET2}$  and, finally, the energy transfer efficiency  $\eta_{ET2} = \frac{k_{ET2}}{k_{ET2} + k_{IC21}}$ . The same procedure is used

for analysing the competition between  $IC_{10}$  and  $ET_1$  deactivation channels, by monitoring the decay of the  $PA_1$  signal.

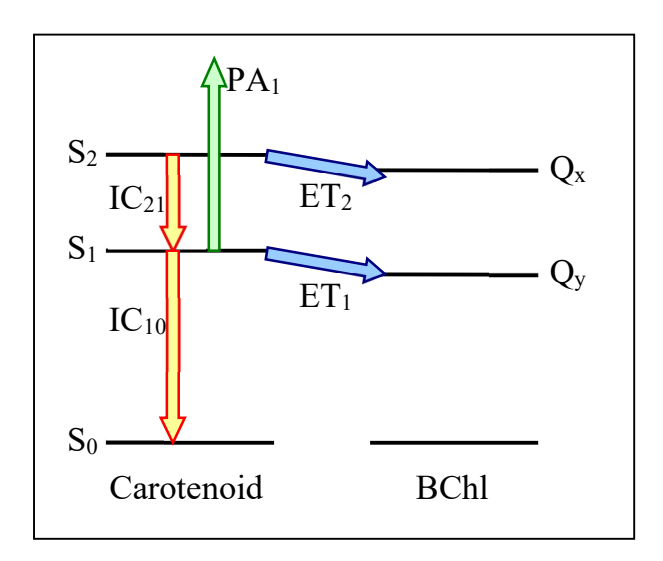


FIG. 4.19. Schematic of the carotenoid and BChl electronic levels relevant for this study, with indication of the possible pathways for population decay: internal conversion (IC<sub>21</sub> and IC<sub>10</sub>) or energy transfer (ET<sub>2</sub> and ET<sub>1</sub>). Population dynamics are monitored by recording the temporal profile of the photo-induced absorption from  $S_1$  (PA<sub>1</sub>).

As we showed, formation and decay of the  $PA_1$  band is wavelength-dependent, so that we cannot directly use the exponential time constants extracted from the pump-probe traces. For this reason, we calculated  $-\Delta T/T$  spectra-integrated time constants, reflecting the real population/depopulation dynamics of excited-states in carotenoids, regardless of their internal evolution due to vibrational-energy redistribution or conformational rearrangement.

For okenone, the results are as follows: (i) internal conversion in CS<sub>2</sub> solution from S<sub>2</sub> to S<sub>1</sub> states occurs with rate  $k_{IC21} = (105 \text{ fs})^{-1}$ , while from S<sub>1</sub> back to S<sub>0</sub> with rate  $k_{IC10} = (4.4 \text{ ps})^{-1}$ ; (ii) S<sub>2</sub> decay of okenone in LH2 complex of *C. Purpuratum* is governed by the overall deactivation rate  $k_{IC21}+k_{ET2}=(85 \text{ fs})^{-1}$ , which takes into account also the energy transfer pathway ET2 from carotenoid S<sub>2</sub> state to BChl Q<sub>x</sub> state; (iii) S<sub>1</sub> decay rate of okenone in LH2 complex is  $k_{IC10}+k_{ET1}=(3.8 \text{ ps})^{-1}$ , which takes into account also the ET1 pathway from carotenoid S<sub>1</sub> to BChl Q<sub>y</sub> state. Assuming that  $k_{IC21}$  and  $k_{IC10}$  in protein environment are the same as in solution, we can evaluate  $k_{ET2} \cong (446 \text{ fs})^{-1}$  and  $k_{ET1} \cong (27.9 \text{ ps})^{-1}$  and calculate an energy transfer efficiency  $\eta_{ET2} = \frac{k_{ET2}}{k_{ET2} + k_{IC21}} = 19\%$  from the S<sub>2</sub> state and  $\eta_{ET1} = \frac{k_{ET1}}{k_{ET1} + k_{IC10}} = 13.6\%$  from the S<sub>1</sub> state of okenone, i.e. an overall ET efficiency of

 $\eta^{\text{okenone}} = 32.6\%$ . Note that the rate of ET2 channel is here measured for the first time, while the ET1 channel is found to be much less efficient than in previous studies [Andersson et al., 1996].

Considering rhodopin glucoside, we obtained (using the same notation as for okenone):  $k_{IC21} = (150 \text{ fs})^{-1}$ ,  $k_{ET2} = (131 \text{ fs})^{-1}$ ,  $k_{IC10} = (4.5 \text{ ps})^{-1}$ ,  $k_{ET1} = (46 \text{ ps})^{-1}$ , with an equivalent ET efficiency of  $\eta_{ET2} = 53\%$ ,  $\eta_{ET1} = 8.9\%$ , thus resulting in  $\eta^{RG} = 68.9\%$ . These results are in good agreement with those obtained using fluorescence up-conversion with 140-200 fs time resolution ( $\eta_{ET2} = 51-56\%$ ,  $\eta_{ET1} = 5\pm2\%$ , Macpherson et al., 2001) and transient absorption with 70-110 fs time resolution ( $\eta_{ET2} = 42\pm7\%$ ,  $\eta_{ET1} = 4\pm3\%$  and  $\eta_{ETS*} = 7\pm3\%$  from an additional S\* state, Wohlleben et el., 2003) and 160 fs time resolution ( $\eta_{ET2} = 50\%$ ,  $\eta_{ET1} = 4\%$ , Rondonuwu et al., 2004). It is worth noting that the  $S_2 \rightarrow Q_x$  energy-transfer efficiency is not an easy parameter to extract, also because it could

depend on other parameters, such as intensity, envelope and phase of the exciting pulses [Herek et al., 2002].

#### 4.3.2 Coherent oscillations analysis

The dynamics in Figs. 4.7(a), 4.10(a), 4.14(a) and 4.16(a), have a superimposed oscillatory pattern, which has been assigned to collective vibrational coherence initiated in the ensemble of photo-excited molecules by the ultrashort pump pulse [Cerullo 1999, Lanzani 2003]. The oscillations are slowly damped and persist on a timescale longer than 1 ps. Fourier analysis of the signals, after subtraction of the slowly varying component, is shown in Fig. 4.20(a) for okenone (solid line) and *C. Purpuratum* (dash/dotted line), and in Fig. 4.20(b) for rhodopin glucoside (solid line) and *R. acidophila* (dash/dotted line). To demonstrate the accuracy of this analysis, in the inset of Fig. 4.20(a) we plotted a fit (solid line) obtained by simply adding two sinusoidal functions at these extracted frequencies (with appropriate amplitudes and phases): a very good agreement is found with the oscillatory component superimposed on the temporal trace (dashed line).

Several coupled modes are present, the strongest being at ≈1155 cm<sup>-1</sup> and ≈1510 cm<sup>-1</sup>. By comparing them to the frequencies obtained for various carotenoids by resonance-Raman profiles [Fujii et al., 1998; Robert, 1999], we have assigned them to a<sub>g</sub>-type C–C and C=C symmetric stretching modes of the conjugated backbone. Around 1000 cm<sup>-1</sup> another smaller feature is visible in some of the pump-probe traces, corresponding to the overlap of methyl in-plane rocking and C–H out-of-plane wagging Raman lines [Robert, 1999]. No evident difference in the oscillation frequencies is seen for the carotenoids in solution and inside the LH2 environment.

It now remains to be clarified on which electronic state the observed vibrational wavepacket is moving. Excitation by an ultrashort pulse can create a vibrational wavepacket in the excited electronic state ( $S_2$  in our case) but also in the ground state ( $S_0$ ), due to a mechanism known as resonant impulsive stimulated Raman scattering [Pollard et al., 1990]. In addition, the internal conversion process to  $S_1$  could take place coherently, i.e. preserving the phase of the collective nuclear motion in the final state [Wang et al., 1994]. In our case, due to the short lifetime of the  $S_2$  state, the long-lasting oscillations

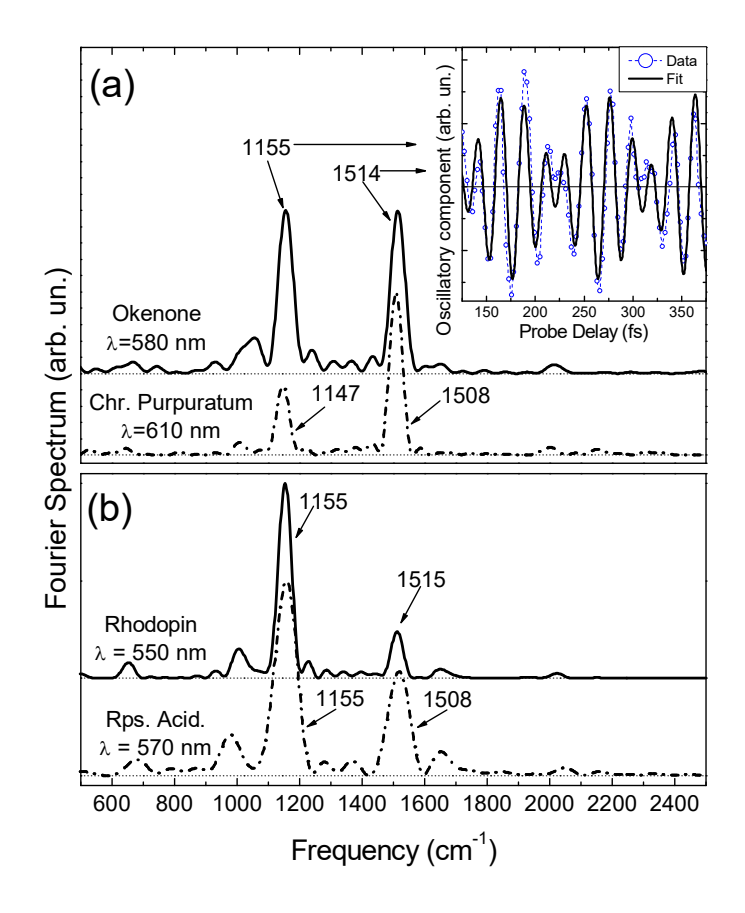


FIG. 4.20. Fourier transform of oscillatory component of  $\Delta T/T$  signal in okenone and LH2 of *C. purpuratum* (a), rhodopin glucoside and LH2 of *R. acidophila* (b). Inset shows the oscillatory component superimposed on the temporal trace of okenone at 580 nm together with a fit based on the frequencies extracted from the Fourier analysis.

[Wang et al., 1994]. In our case, due to the short lifetime of the have  $S_2$  state, the long-lasting oscillations have to be assigned to either the  $S_0$  or the  $S_1$  state. Since our measured frequencies match very well those measured with ground state Raman scattering [Robert, 1999] and the frequencies coupled to  $S_1$  are known to be different from those coupled to  $S_0$  [Hashimoto et al., 1991], we assign the observed vibrational wavepacket to the ground state.

## 4.3.3 Conclusions

In conclusion, we have presented pump-probe measurements, using sub-10-fs pulses, on carotenoids both in solution and inside the LH2 complex of two different light-harvesting purple bacteria. Our data provide a picture, with the highest possible temporal resolution, of the internal conversion process and allow to time-resolve the energy transfer process to the bacterio-chlorophylls. This kinetic data, together with the available structural information on the spatial arrangement of the chromophores within the LH2 complex, laid the foundation for the detailed understanding of the mechanisms of energy transfer involved in this fundamental, early reaction in photosynthesis.

- Akhmanov, S.A., V.A. Vysloukh, and A.S. Chirkin. *Optics of Femtosecond Laser Pulses* (American Institute of Physics, New York, 1992).
- Akhmanov, A.G., S.A. Akhmanov, R.V. Khoklov, A.I. Kovrigin, A.S. Piskarkas, and A.P. Sukhorukow. 1968. Parametric interactions in optics and tunable light oscillators. *IEEE J. Quantum Electron*. QE-4:828–831
- Akimoto, S., I. Yamazaki, S. Takaichi, and M. Mimuro. Excitation relaxation dynamics of linear carotenoids. J. Lumin. 87–89:797–799
- Alfano, R.R., ed., *The Supercontinuum Laser Source* (Springer-Verlag, New York, 1989)Backus, S., C. Durfee, M.M. Murnane, and H.C. Kapteyn. 1998. High power ultrafast lasers. *Rev. Sci. Instr.* 69:1207–1223
- Andersson, P. O., S. M. Bachilo, R.-L. Chen, and T. Gillbro. 1995a. Solvent and Temperature Effects on Dual Fluorescence in a Series of Carotenes. Energy Gap Dependence of the Internal Conversion Rate. *J. Phys. Chem.* 99:16199–16209
- Andersson, P. O., and T. Gillbro. 1995b. Photophysics and dynamics of the lowest excited singlet state in long substituted polyenes with implications to the very long-chain limit. *J. Chem. Phys.* 103:2509–2519
- Andersson, P. O., R. J. Cogdell, and T. Gillbro. 1996. Femtosecond dynamics of carotenoid-to-bacteriochlorophyll *a* energy transfer in light-harvesting antenna complexes from the purple bacterium *Chromatium Purpuratum*. *Chem. Phys.* 210:195–217
- Baltuška, A., T. Fuji, and T. Kobayashi. 2002a. Visible pulse compression to 4fs by optical parametric amplification and programmable dispersion control. *Opt. Lett.* 27:306–308
- Baltuška, A., T. Fuji, and T. Kobayashi. 2002b. Self-referencing of the carrier-envelope slip in a 6-fs visible parametric amplifier. *Opt. Lett.* 27:1241–1243
- Baumgartner, R.A., and R.L. Byer. 1979. Optical parametric amplification. *IEEE J. Quantum Electron.* 15:432–444

- Bautista, J. A., R. E. Connors, B. Bangar Raju, R. G. Hiller, F. P. Sharples, D. Gosztola, M. R. Wasielewski, and H. A. Frank. 1999. Excited State Properties of Peridinin: Observation of a Solvent Dependence of the Lowest Excited Singlet State Lifetime and Spectral Behavior Unique among Carotenoids. *J. Phys. Chem. B*. 103:8751–8758
- Billsten, H. H., D. Zigmantas, V. Sundström, and T. Polívka. 2002. Dynamics of vibrational relaxation in the S1 state of carotenoids having 11 conjugated C=C bonds. *Chem. Phys. Lett.* 355:465–470
- Borsutzky, A., R. Brünger, Ch. Huang, and R. Wallenstein. 1991. Harmonic and sum-frequency generation of pulsed laser radiation in BBO, LBO, and KD\*P. *Appl. Phys. B* 52:55–62
- Boyd, R. Nonlinear Optics (Academic, New York, 1992).
- Brabec, T., and F. Krausz. 2000. Intense few-cycle laser fields: frontiers of nonlinear optics. *Rev. Mod. Phys.* 72:545–591
- Byer, R.L., and R.L. Herbst. 1977. in *Nonlinear Infrared Generation*, Y. R. Shen, ed. (Springer-Verlag, Berlin). p. 96.
- Cerullo, G., M. Nisoli, and S. De Silvestri. 1997. Generation of 11 fs pulses tunable across the visible by optical parametric amplification. *Appl. Phys. Lett.* 71:3616–3618
- Cerullo, G., M. Nisoli, S. Stagira, and S. De Silvestri. 1998. Sub-8-fs pulses from an ultrabroadband optical parametric amplifier in the visible. *Opt. Lett.* 16:1283–1285
- Cerullo, G., M. Nisoli, S. Stagira, S. De Silvestri, G. Tempea, F. Krausz, and K. Ferencz. 1999. Mirror-dispersion-controlledsub-10-fs optical parametric amplifier in the visible. *Opt. Lett.* 24:1529–1531
- Cerullo, G., M. Nisoli, S. Stagira, S. De Silvestri, G. Tempea, F. Krausz, and K. Ferencz. 2000. Mirror-dispersion-controlled OPA: a compact tool for sub-10-fs spectroscopy in the visible. *Appl. Phys. B* 70:S253–S259
- Cerullo, G., G. Lanzani, M. Zavelani-Rossi, and S. De Silvestri. 2001. Early events of energy relaxation in all-*trans*-β-carotene following sub-10 fs optical-pulse excitation. *Phys. Rev. B.* 63:R241104 (1–4)

- Cerullo, G., D. Polli, G. Lanzani, S. De Silvestri, H. Hashimoto, and R. J. Cogdell. 2002. Photosynthetic Light Harvesting by Carotenoids: Detection of an Intermediate Excited State. *Science* 298:2395–2398
- Cerullo, G., and S. De Silvestri. 2003. Ultrafast optical parametric amplifiers. *Rev. Sci. Instrum.* 74:1–18
- Chen, C., Y. Wu, A. Jiang, B. Wu, G. You, R. Li, and S. Lin. 1989. New nonlinear-optical crystal: LiB<sub>3</sub>O<sub>5</sub>. *J. Opt. Soc. Am. B* 6:616–621
- Chynwat, V., and H. A. Frank. 1995. The application of the energy gap law to the S1 energies and dynamics of carotenoids. *Chem. Phys.* 194:237–244
- Cogdell, R. J., E. J. Land, and T. G. Truscott. 1983. The triplet extinction coefficients of some bacterial carotenoids *Photochem. Photobiol.* 38:723–725
- Cogdell, R. J., and H. A. Frank. 1987. "How carotenoids function in photosynthetic bacteria". *Biochim. Biophys. Acta* 895:63–79
- Cogdell, R. J., A. M. Hawthornthwaite, M. B. Evans, L. A. Ferguson, C. Kerfeld, J. P. Thornber, F. van Mourik, and R. van Grondelle. 1990. Isolation and characterisation of an unusual antenna complex from the marine purple sulphur photosynthetic bacterium *Chromatium purpuratum* BW5500. *Biochim. Biophys. Acta.* 1019:239-244
- Cogdell, R.J., and A. M. Hawthornthwaite. 1991 Bacteriochlorophyll-binding protein. *In* CRC Handbook on 'the Chlorophylls'. H. Scheer, editor. CBC Press, Boca Raton, Florida. pp 493–528
- Cogdell, R. J., N. W. Isaacs, T. D. Howard, K. McLuskey, N. J. Freser, and S. M. Prince. 1999. How Photosynthetic Bacteria Harvest Solar Energy. *J. Bacteriol.* 181:3869–3879
- Damjanović, A., T. Ritz, and K. Schulten. 1999. Energy transfer between carotenoids and bacteriochlorophylls in light-harvesting complex II of purple bacteria *Phys. Rev. E* 59:3293–3311
- Danielius, R., A. Piskarskas, P. Di Trapani, A. Andreoni, C. Solcia, and P. Foggi. 1996. Matching of group velocities by spatial walk-off in collinear three-wave interaction with tilted pulses. *Opt. Lett.* 21:973–975

- de Weerd, F. L., I. H. M. van Stokkum, and R. van Grondelle. 2002. Subpicosecond dynamics in the excited state absorption of all-*trans*-β-Carotene. *Chem. Phys. Lett.* 354:38–43
- Di Trapani, P., A. Andreoni, C. Solcia, G. P. Banfi, R. Danielius, A. Piskarskas, and P. Foggi. 1997. Powerful sub-100-fs pulses broadly tunable in the visible from a blue-pumped parametric generator and amplifier. *J. Opt. Soc. Am. B* 14:1245–1248
- Dmitriev, V.G., G.G. Gurzadyan, and D.N. Nikogosyan. *Handbook of Nonlinear Optical Crystals* (Springer Verlag, Berlin, 1991).
- Dorrer, C., B. de Beauvoir, C. Le Blanc, S. Ranc, J.-P. Rousseau, P. Rousseau, J.-P. Chambaret, and F. Salin. 1999. Single-shot real-timecharacterization of chirped-pulse amplificationsystems by spectral phase interferometry for direct electric-fieldreconstruction. *Opt. Lett.* 24:1644–1646
- Driscoll, T.J., G.M. Gale, F. Hache. 1994. Ti:sapphire second-harmonic-pumped visible range femtosecond optical parametric oscillator. *Opt. Comm.* 110:638–644
- Eimerl, D., L. Davis, S. Velsko, E.K. Graham, and A. Zalkin. 1987. Optical, mechanical, and thermal properties of barium borate. *J. Appl. Phys.* 62:1968–1983
- Elsaesser, T., S. Mukamel, M.M. Murnane, N.F. Scherer (eds.) *Ultrafast Phenomena XII*, Springer Verlag Series in Chemical Physics, Vol. 66, Berlin, 2001
- Fork, R.L., B.I. Greene and C.V. Shank. 1981. Generation of optical pulses shorter than 0.1 psec by colliding pulse mode locking. *Appl. Phys. Lett.* 38:671–672
- Fork, R.L., C.V. Shank, C. Hirlimann, R. Yen, and W.J. Tomlinson. 1983. Femtosecond white-light continuum pulses. *Opt. Lett.* 8:1–3
- Frank, H. A., and R. J. Cogdell. 1996. Carotenoids in photosynthesis. *Photochem. Photobiol.* 63:257–264
- Frank, H. A., R. Z. B. Desamero, V. Chynwat, R. Gebhard, I. van der Hoef, F. J. Jansen, J. Lugtenburg, D. Gosztola, M. R. Wasielewski. 1997. Spectroscopic properties of spheroidene analogs having different extents of pi-electron conjugation. *J. Phys. Chem. A* 101:149–157

- Frank, H. A., J. A. Bautista, J. Josue, Z. Pendon, R. G. Hiller, F. P. Sharples, D. Gosztola, and M. R. Wasielewski. 2000. Effect of the Solvent Environment on the Spectroscopic Properties and Dynamics of the Lowest Excited States of Carotenoids. *J. Phys. Chem. B* 104:4569–4577
- Frank, H. A., J. S. Josue, J. A. Bautista, I. van der Hoef, F. J. Jansen, J. Lugtenburg, G. Wiederrecht, and R. L. Christensen. 2002. Spectroscopic and Photochemical Properties of Open-Chain Carotenoids. *J. Phys. Chem. B* 106:2083–2092
- Fujii, R., C.-H. Chen, T. Mizoguchi, and Y. Koyama. 1998. <sup>1</sup>H NMR, electronic-absorption and resonance-Raman spectra of isomeric okenone as compared with those of isomeric β-carotene, canthaxanthin, β-apo-8'-carotenal and spheroidene. *Spectrochim. Acta A* 54:727–743
- Fujii, R., T. Ishikawa, Y. Koyama, M. Taguchi, Y. Isobe, H. Nagae, and Y. Watanabe. 2001. Fluorescence Spectroscopy of All-*trans*-anhydrorhodovibrin and Spirilloxanthin: Detection of the 1B<sub>u</sub>-Fluorescence. *J. Phys. Chem. A* 105:5348-5355
- Fujii, R., T. Inaba, Y. Watanabe, Y. Koyama, and J.-P Zhang. 2003. Two different pathways of internal conversion in carotenoids depending on the length of the conjugated chain. *Chem. Phys. Lett.* 369:165–172
- Furuichi, K., T. Sashima, and Y. Koyama. 2002. The first detection of the  $3A_g^-$  state in carotenoids using resonance-Raman excitation profiles. *Chem. Phys. Lett.* 356:547–555
- Gaeta, A.L. 2000. Catastrophic Collapse of Ultrashort Pulses. *Phys. Rev. Lett.* 84:3582–3585
- Gale, G. M., M. Cavallari, T. J. Driscoll, and F. Hache. 1995. Sub-20-fs tunable pulses in the visible from an 82-MHz optical parametric oscillator. *Opt. Lett.* 20:1562–1564
- Gale, G. M., M. Cavallari, and F. Hache. 1998a. Femtosecond visible optical parametric oscillator. *J. Opt. Soc. Am. B* 15:702–714
- Gale, G. M., F. Hache, and M. Cavallari. 1998b. Broad-Bandwidth Parametric Amplification in the Visible: Femtosecond Experiments and Simulations. IEEE J. Sel. Top. Quantum Electron. 4:224–229

- Gallmann, L., D. H. Sutter, N. Matuschek, G. Steinmeyer, U. Keller, C. Iaconis, and I. A. Walmsley. 1999. Characterization of sub-6-fs optical pulses with spectral phase interferometry for direct electric-field reconstruction. *Opt. Lett.* 24:1314–1316
- Giordamaine, J.A., and R.C. Miller. 1965. Tunable Coherent Parametric Oscillation in LiNbO<sub>3</sub> at Optical Frequencies. *Phys. Rev. Lett.* 14:973–976
- Gradinaru, C. C., J. T. M. Kennis, E. Papagiannakis, I. H. M. van Stokkum, R. J. Cogdell, G. R. Fleming, R. A. Niederman, and R. van Grondelle. 2001. An unusual pathway of excitation energy deactivation in carotenoids: Singlet-to-triplet conversion on an ultrafast timescale in a photosynthetic antenna. *Proc. Nat. Acad. Sci.* 98: 2364–2369
- Greenfield, S. R., and M. R. Wasielewski. 1995. Near-transform-limited visible and near-IR femtosecond pulses from optical parametric amplification using Type II beta -barium borate. *Opt. Lett.* 20:1394–1396
- Harada, I., Y. Furukawa, M. Tasumi, H. Shirakawa, and S. Ikeda. 1980. Spectroscopic studies on doped polyacetylene and β-carotene. *J. Chem. Phys.* 73:4746–4757
- Harris, S.E., M.K. Oshman, and R.L. Byer. 1967. Observation of Tunable Optical Parametric Fluorescence. *Phys. Rev. Lett.* 18:732–734
- Hashimoto, H., Y. Koyama, Y. Hirata, and N. Mataga. 1991. S<sub>1</sub> and T<sub>1</sub> Species of β-Carotene Generated by Direct Photoexcitation from the All-Trans, 9-Cis, 13-Cis, and 15-Cis Isomers As Revealed by Picosecond Transient Absorption and Transient Raman Spectroscopies. *J. Phys. Chem.* 95:3072–3076
- Hebling, J., E. J. Mayer, J. Kuhl, and R. Szipocs. 1995. Chirped-mirror dispersion-compensated femtosecond optical parametric oscillator. *Opt. Lett.* 20:919–921
- Herek, J. L., W. Wohlleben, R. J. Cogdell, D. Zeidler, and M. Motzkus. 2002. Quantum control of energy flow in light harvesting. *Nature* 417:533–535
- Hudson, B. S., and B. E. Kohler. A low-lying weak transition in the polyene α,ω-diphenyloctatetraene. *Chem. Phys. Lett.* 14:299–304
- Iaconis, C., and A. Walmsley. 1998. Spectral phase interferometryfor direct electric-field reconstruction of ultrashort optical pulses. *Opt. Lett.* 23:792–794

- Iaconis, C., and I.A. Walmsley. 1999. Self-referencing spectral interferometry for measuring ultrashort optical pulses. *IEEE J. Quantum Electron*. QE-35:501-509
- Isler, O., H. Gutmann, and U. Solms. 1971. Carotenoids. Published by Birkhäuser-Verlag, Basel, Stuttgart.
- Kandori, H., H. Sasabe, and M. J. Mimuro. 1994. Direct determination of a lifetime of the S<sub>2</sub> state of β-carotene by femtosecond time-resolved fluorescence spectroscopy. J. Am. Chem. Soc. 116:2671–2672
- Kane, D.J., and R. Trebino. 1993. Characterization of arbitrary femtosecond pulses using frequency-resolved optical gating. *IEEE J. Quantum Electron*. QE-29:571–579
- Kärtner, F. X., N. Matuschek, T. Schibli, U. Keller, H. A. Haus, C. Heine, R. Morf, V. Scheuer, M. Tilsch, and T. Tschudi. 1997. Design and fabrication of double-chirped mirrors. *Opt. Lett.* 22:831–833
- Kobayashi, T., and A. Shirakawa. 2000. Tunable visible and near-infrared pulse generator in a 5 fs regime. *Appl. Phys. B* 70:S239–S246
- Kobayashi, T., T. Okada, T. Kobayashi, K. A. Nelson, and S. De Silvestri (eds.). 2005. *Ultrafast Phenomena XIV*, Springer Verlag Series in Chemical Physics, Vol. 79, Berlin, ISBN: 3-540-24110-8
- Koechner, W. Solid-State Laser Engineering, IV Edition (Springer Verlag, Berlin, 1996).
- Koepke, J., X. Hu, C. Muenke, K. Schulten, and H. Michel. 1996. The crystal structure of the light-harvesting complex II (B800-850) from Rhodospirillum molischianum. *Structure* 4:581–597
- Koyama, Y. 1991. Structures and function of carotenoids in photosynthetic systems. *J. Photochem. Photobiol. B* 9:265–280
- Koyama, Y., and R. Fujii. 1999. *Cis-Trans* Carotenoids in Photosynthesis: Configurations, Excited-State Properties and Physiological Functions. In Photochemistry of Carotenoids. H. A. Frank, A. J. Young, G. Britton, and R. J. Cogdell, editors. Kluwer Academic Publishers, Dordrecht, The Netherlands. 161–188

- Krueger, B. P., G. D. Scholes, R. Jimenez, and G. R. Fleming. 1998a. Electronic Excitation Transfer from Carotenoid to Bacteriochlorophyll in the Purple Bacterium *Rhodopseudomonas acidophila. J. Phys. Chem. B* 102:2284–2292
- Krueger, B. P., G. D. Scholes, and G. R. Fleming. 1998b. Calculation of Couplings and Energy-Transfer Pathways between the Pigments of LH2 by the ab Initio Transition Density Cube Method . *J. Phys. Chem. B* 102:5378–5386
- Kukura, P., D.W. McCamant, and R.A. Mathies. 2004. Femtosecond Time-Resolved Stimulated Raman Spectroscopy of the S2 (1B<sub>u</sub><sup>+</sup>) Excited State of β-Carotene. *J. Phys. Chem. A* 108:5921–5925
- Lang, H.P., and C. N. Hunter. 1994. The relationship between carotenoids biosynthesis and the assembly of the light-harvesting LH2 complex in Rhodobacter sphaeroides *Biochem. J.* 298:197–205
- Lanzani, G., G. Cerullo, C. Brabec, and N. S. Sariciftci. 2003. Time Domain Investigation of the Intrachain Vibrational Dynamics of a Prototypical Light-Emitting Conjugated Polymer. *Phys. Rev. Lett.* 90:047402 (1–4)
- Lanzani, G., G. Cerullo, D. Polli, A. Gambetta, M. Zavelani-Rossi, and C. Gadermaier. 2004. Photophysics of conjugated polymers: the contribution of ultrafast spectroscopy. *Phys. Stat. Sol. (a)* 201:1116–1131
- Lin, S., Z. Sun, B. Wu, and C. Chen. 1990. The nonlinear optical characteristics of a LiB<sub>3</sub>O<sub>5</sub> crystal. *J. Appl. Phys.* 67:634–638
- Macpherson, A. N., and T. Gillbro. 1998. Solvent Dependence of the Ultrafast S<sub>2</sub>-S<sub>1</sub> Internal Conversion Rate of β-Carotene. *J. Phys. Chem. A* 102:5049–5058
- Macpherson, A. N., J. B. Arellano, N. J. Fraser, R. J. Cogdell, and T. Gillbro. 2001. Efficient Energy Transfer from the Carotenoid S<sub>2</sub> State in a Photosynthetic Light-Harvesting Complex. *Biophys. J.* 80:923–930
- McDermott, G., S. M. Prince, A. A. Freer, A. M. Hawthornethwaite-Lawless, M. Z. Papiz, R. J. Cogdell, N. W. Isaacs. 1995. Crystal structure of an integral membrane light harvesting complex from photosynthetic bacteria. *Nature*. 374:517–521
- Mimuro, M., and T. Katoh. 1991. Carotenoids in photosynthesis-absorption, transfer and dissipation of light energy. *Pure Appl Chem* 63:123-130

- Naganuma, K., Kazuo Mogi, and Hajime Yamada. 1990. Group-delay measurement using the Fourier transform of an interferometric cross correlation generated by white light. *Opt. Lett.* 15:393–395
- Nishimura, K., F. S. Rondonuwu, R. Fujii, J. Akahane, Y. Koyama, T. Kobayashi. 2004. Sequential singlet internal conversion of  $1B_u^+ \rightarrow 3A_g^- \rightarrow 1B_u^- \rightarrow 2A_g^- \rightarrow (1A_g^- \text{ground})$  in all-*trans*-spirilloxanthin revealed by two-dimensional sub-5-fs spectroscopy. *Chem. Phys. Lett.* 392:68–73
- Nisoli, M., S. De Silvestri, V. Magni, O. Svelto, R. Danielius, A. Piskarskas, G. Valiulis, and A. Varanavicius. 1994. Highly efficient parametric conversion of femtosecond Ti:sapphire laser pulses at 1 kHz. *Opt. Lett.* 19: 1973–1975
- Nisoli, M., S. De Silvestri, O. Svelto, R. Szipcs, K. Ferencz, Ch. Spielmann, S. Sartania, and F. Krausz. 1997. Compression of high-energy laser pulses below 5 fs. *Opt. Lett.* 22:522–524
- Norris, T.B. 1992. Femtosecond pulse amplification at 250 kHz with a Ti:sapphire regenerative amplifier and application to continuum generation. *Opt. Lett.* 17:1009–1011
- Papagiannakis, E., J. T. M. Kennis, I. H. M. van Stokkum, R. J. Cogdell, and R. van Grondelle. 2002. An alternative carotenoid-to-bacteriochlorophyll energy transfer pathway in photosynthetic light harvesting. *Proc. Nat. Acad. Sci.* 99:6017–6022
- Papiz, M. Z., S. M. Prince, T. Howard, R. J. Cogdell, and N. W. Isaacs. 2003. The structure and thermal motion of the B800-850 LH2 complex from Rps. acidophila at 2.0A resolution and 100K: new structural features and functionally relevant motions. *J. Mol. Biol.* 326:1523–1538
- Paye, J. 1992. The chronocyclic representation of ultrashort light pulses. *IEEE J. Quant. Electr.* 28:2262–2273
- Pellegrin, E., J. Fink, and S. L. Drechsler. 1991. Momentum-dependent excitations in β-carotene, a finite-size system between molecules and polymers. *Phys. Rev. Lett.* 66:2022–2025

- Petrov, V., and F. Noack. 1995. Frequency upconversion of tunable femtosecond pulses by parametric amplification and sum-frequency generation in a single nonlinear crystal. *Opt. Lett.* 20: 2171–2173
- Polívka, T., D. Zigmantas, H. A. Frank, J. A. Bautista, J. L. Herek, Y. Koyama, R. Fujii, V. Sundström. 2001. Near-Infrared Time-Resolved Study of the S<sub>1</sub> State Dynamics of the Carotenoid Spheroidene. *J. Phys. Chem. B* 105:1072–1080
- Polívka, T., and V. Sundström. 2004. Ultrafast Dynamics of Carotenoid Excited States—From Solution to Natural and Artificial Systems. *Chem. Rev.* 104: 2021–2071
- Pollard, W. T., H. L. Fragnito, J. -Y. Bigot, C. V. Shank, and R. A. Mathies. 1990. Quantum-mechanical theory for 6 fs dynamic absorption spectroscopy and its application to nile blue. *Chem. Phys. Lett.* 168:239–245
- Polli, D., G. Cerullo, G. Lanzani, S. De Silvestri, H. Hashimoto, and R. J. Cogdell. 2003. Excited-state dynamics of carotenoids with different conjugation length. *Synth. Met.* 139:893–896
- Polli, D., G. Cerullo, G. Lanzani, S. De Silvestri, K. Yanagi, H. Hashimoto, and R. J. Cogdell. 2004. Conjugation Length Dependence of Internal Conversion in Carotenoids: Role of the Intermediate State. *Phys. Rev. Lett* 93:163002
- Reed, M.K., M. K. Steiner-Shepard, and D. K. Negus. 1994. Widely tunable femtosecond optical parametric amplifier at 250 kHz with a Ti:sapphire regenerative amplifier. *Opt. Lett.* 19:1855–1857
- Reed, M. K., M. S. Armas, M. K. Steiner-Shepard, D. K. Negus. 1995. 30-fs pulses tunable across the visible with a 100-kHz Ti:sapphire regenerative amplifier. *Opt. Lett.* 20:605–607
- Ricci, M., S. E. Bradforth, R. Jimenez, G. R. Fleming. 1996. Internal conversion and energy transfer dynamics of spheroidene in solution and in the LH-1 and LH-2 light-harvesting complexes. *Chem. Phys. Lett.* 259:381–390
- Riedle, E., M. Beutter, S. Lochbrunner, J. Piel, S. Schenkl, S. Spörlein, and W. Zinth. 2000. Generation of 10 to 50 fs pulses tunable through all of the visible and the NIR. *Appl. Phys. B* 71:457–465

- Ritz, T., A. Damjanović, K. Schulten, J.-P. Zhang, and Y. Koyama. 2000. Efficient light harvesting through carotenoids. *Photosynth. Res.* 66:125–144
- Robert, B., and M. Lutz. 1985. Structure of antenna complexes of several Rhodospirillaceae from their resonance Raman spectra. *Biochim. Biophys. Acta* 807:10–23
- Robert, B. 1999. The Electronic Structure, Stereochemistry and Resonance Raman Spectroscopy of Carotenoids. In Photochemistry of Carotenoids. H. A. Frank, A. J. Young, G. Britton, and R. J. Cogdell, editors. Kluwer Academic Publishers, Dordrecht, The Netherlands. 189–222
- Rondonuwu, F. S., K. Yokoyama, R. Fujii, Y. Koyama, R. J. Cogdell, and Y. Watanabe. 2004. The role of the 1<sup>1</sup>B<sub>u</sub><sup>-</sup> state in carotenoid-to-bacteriochlorophyll singlet-energy transfer in the LH2 antenna complexes from *Rhodobacter sphaeroides* G1C, *Rhodobacter sphaeroides* 2.4.1, *Rhodospirillum molischianum* and *Rhodopseudomonas acidophila. Chem. Phys. Lett.* 390:314–322
- Sashima, T., H. Nagae, M. Kuki, and Y. Koyama. 1999. A new singlet-excited state of all-*trans*-spheroidene as detected by resonance-Raman excitation profiles. *Chem. Phys. Lett.* 299:187–194
- Sashima T., Y. Koyama, T. Yamada, and H. Hashimoto. 2000. The  ${}^{1}B_{u}^{+}$ ,  ${}^{1}B_{u}^{-}$ , and  ${}^{2}A_{g}^{-}$  Energies of Crystalline Lycopene, β-Carotene, and Mini-9-β-carotene as Determined by Resonance-Raman Excitation Profiles: Dependence of the  ${}^{1}B_{u}^{-}$  State Energy on the Conjugation Length. *J. Phys. Chem. B* 104:5011-5019
- Schulten, K., and M. Karplus. 1972. On the origin of a low-lying forbidden transition in polyenes and related molecules. *Chem. Phys. Lett.* 14:305–309
- Seifert, F., V. Petrov, and F. Noack. 1994. Sub-100-fs optical parametric generator pumped by a high-repetition-rate Ti:sapphire regenerative amplifier system. *Opt. Lett.* 19:837–839
- Shen, Y.R. The Principles of Nonlinear Optics (John Wiley & Sons, New York, 1984).
- Shima, S., R. P. Ilagan, N. Gillespie, B. J. Sommer, R. G. Hiller, F. P. Sharples, H. A. Frank, and R. R. Birge. 2003. Two-Photon and Fluorescence Spectroscopy and the Effect of Environment on the Photochemical Properties of Peridinin in Solution and

- in the Peridinin-Chlorophyll-Protein from Amphidinium carterae. *J. Phys. Chem. A* 107:8052–8066
- Shirakawa, A., and T. Kobayashi. 1998a. Noncollinearly phase-matched femtosecond optical parametric amplification with a 2000 cm<sup>-1</sup> bandwidth *Appl. Phys. Lett.* 72:147–149
- Shirakawa, A., and T. Kobayashi. 1998b. Noncollinear Phase- and Group-Velocity Matching of Optical Parametric Amplifier for Ultrashort Pulse Generation. *IEICE Trans. Electron.* E81-C:246-253
- Shirakawa, A., I. Sakane, and T. Kobayashi. Pulse-front-matched optical parametric amplification for sub-10-fs pulse generation tunable in the visible and near infrared. 1998c. *Opt. Lett.* 23:1292–1294
- Shirakawa, A., I. Sakane, M. Takasaka, and T. Kobayashi. 1999. Sub-5-fs visible pulse generation by pulse-front-matched noncollinear optical parametric amplification. *Appl. Phys. Lett.* 74:2268–2270
- Shreve, A. P., J. K. Trautman, T. G. Owens, and A. C. Albrecht. 1991. Determination of the S<sub>2</sub> lifetime of β–carotene. *Chem. Phys. Lett.* 178, 89–96
- Shuman, T. M., I. A. Walmsley, L. J. Waxer, M. E. Anderson, C. Iaconis, and J. Bromage. 1999. Real-time SPIDER: ultrashort pulse characterization at 20 Hz. *Opt. Expr.* 5:134–143
- Siefermann-Harms, D. 1987. The light harvesting protective functions of carotenoids in photosynthetic membranes. *Physiol. Plant.* 69:561–568
- Spence, D. E., P. N. Kean, and W. Sibbett. 60-fsec pulse generation from a self-mode-locked Ti:sapphire laser. *Opt. Lett.* 16:42-44
- Steinmeyer, G., D.H. Sutter, L. Gallmann, N. Matuschek, and U. Keller. 1999. Frontiers in Ultrashort Pulse Generation: Pushing the Limits in Linear and Nonlinear Optics. *Science* 286:1507–1512
- Stingl, a., C. Spielmann, F. Krausz, R. Szipocs. 1994. Generation of 11-fs pulses from a Ti:sapphire laser without the use of prisms. *Opt. Lett.* 19:204–206

- Stingl., A., M. Lenzner, C. Spielmann, F. Krausz, and R. Szipocs. 1995. Sub-10-fs mirror-dispersion-controlled Ti:sapphire laser. *Opt. Lett.* 20:602–604
- Strickland, D., and G. Mourou. 1985. Compression of amplified chirped optical pulses. *Opt. Commun.* 56:219–221
- Szipöcs, R., K. Ferencz, C. Spielmann, and F. Krausz. 1994. Chirped multilayer coatings for broadband dispersion control in femtosecond lasers. *Opt. Lett.* 19:201–203
- Takeda, M., H. Ina, and S. Kobayashi. 1982. Fourier-transform method of fringe-pattern analysis for computer-based topography and interferometry. J. Opt. Soc. Am. 72: 156
- Tavan, P., and K. Schulten. 1986. The low-lying electronic excitations in long polyenes: A PPP-MRD-CI study. *J. Chem. Phys.* 85:6602–6609
- Tavan, P., and K. Schulten. 1987. Electronic excitations in finite and infinite polyenes. *Phys. Rev. B.* 36:4337–4358
- Trebino, R., K. W. DeLong, D. N. Fittinghoff, J. N. Sweetser, M. A. Krumbügel, B. A. Richman, and Daniel J. Kane. 1997. Measuring ultrashort laser pulses in the time-frequency domain using frequency-resolved optical gating. *Rev. Sci. Instrum*. 68:3277–3295
- Wang, Q., L. Peteanu, R. W. Schoenlein, C. V. Shank, and R. Mathies. 1994. Vibrationally coherent photochemistry in the femtosecond primary event of vision. *Science* 266:422-424
- Wilhelm, T., J. Piel, and E. Riedle. 1997. Sub-20-fs pulses tunable across the visible from a blue-pumped single-pass noncollinear parametric converter. *Opt. Lett.* 22:1494–1496
- Wohlleben, W., T. Buckup, J. L. Herek, R. J. Cogdell, and M. Motzkus. 2003. Multichannel Carotenoid Deactivation in Photosynthetic Light Harvesting as Identified by an Evolutionary Target Analysis. *Biophys. J.* 85:442–450
- Yakovlev, V. V., B. Kohler, and K. R. Wilson. 1994. Broadly tunable 30-fs pulses produced by optical parametric amplification. *Opt. Lett.* 19:2000–2002

- Yamamoto, H. Y., R. C. Bugos, and A. D. Hieber. 1999. In *The Photochemistry of Carotenoids*, eds. Frank, H. A., A. J. Young, G. Britton, and R. J. Cogdell. Kluwer Academic Press, The Netherlands, pp. 295–325
- Yeremenko, S., A. Baltuška, M.S. Pshenichnikov, and D.A. Wiersma. 2000. The criterion of pulse reconstruction quality based on Wigner representation. *Appl. Phys. B* 70:S109–S117
- Yoshizawa, M., H. Aoki, H. Hashimoto. 2001. Vibrational relaxation of the 2A<sub>g</sub><sup>-</sup> excited state in all-*trans*-β-carotene obtained by femtosecond time-resolved Raman spectroscopy. Phys. Rev. B. 63:180301(1–4)
- Zavelani-Rossi, M., G. Cerullo, S. De Silvestri, L. Gallmann, N. Matuschek, G. Steinmeyer, and U. Keller. 2001. Pulse compression over a 170-THz bandwidth in the visible by use of only chirped mirrors. *Opt. Lett.* 26:1155–1157
- Zavelani-Rossi, M., D. Polli, G. Cerullo, S. De Silvestri, L. Gallmann, G. Steinmeyer, U. Keller. 2002. Few-optical-cycle laser pulses by OPA: broadband chirped mirror compression and SPIDER characterization. *Appl. Phys. B* 74: S245–S251
- Zewail, A. H. 2000. Femtochemistry: Atomic-Scale Dynamics of the Chemical Bond. *J. Phys. Chem. A.* 104:5660–5694
- Zhang, J.Y., J.Y. Huang, Y.R. Shen, and C. Chen. 1993. Optical parametric generation and amplification in barium borate and lithium triborate crystals. *J. Opt. Soc. Am. B* 10:1758–1764
- Zhang, J.-P., T. Inaba, Y. Watanabe, and Y. Koyama. 2000a. Excited-state dynamics among the  $1B_u^+$ ,  $1B_u^-$  and  $2A_g^-$  states of all-*trans*-neurosporene as revealed by near-infrared time-resolved absorption spectroscopy. *Chem. Phys. Lett.* 332:351–358
- Zhang, J.-P., R. Fujii, P. Qian, T. Inaba, T. Mizoguchi, Y. Koyama, K. Onaka, and Y. Watanabe. 2000b. Mechanism of the Carotenoid-to-Bacteriochlorophyll Energy Transfer via the S<sub>1</sub> State in the LH2 Complexes from Purple Bacteria. *J. Phys. Chem. B* 104:3683–3691
- Zhang, J.-P., T. Inaba, Y. Watanabe, and Y. Koyama. 2001a. Partition of carotenoid-to-bacteriochlorophyll singlet-energy transfer through two channels in the LH2 complex from *Rhodobacter sphaeroides* G1C. *Chem. Phys. Lett.* 340: 484–491

- Zhang, J.-P., L. H. Skibsted, R. Fujii, and Y. Koyama. 2001b. Transient Absorption from the 1Bu+ State of All-*trans*-β-carotene Newly Identified in the Near-infrared Region. *Photochem. Photobiol.* 73:219–222
- Zhou, J.P., G. Taft, C.P. Huang, M.M. Murnane, H.C. kapteyn, and I.P. Christov. 1994. Pulse evolution in a broad-bandwidth Ti:sapphire laser. *Opt. Lett.* 19:1149–1151
- Zigmantas, D., R. G. Hiller, A. Yartsev, V. Sundström, and T. Polívka. 2003. Dynamics of Excited States of the Carotenoid Peridinin in Polar Solvents: Dependence on Excitation Wavelength, Viscosity, and Temperature. *J. Phys. Chem. B.* 107:5339–5348
- Zigmantas, D., R. G. Hiller, F. P. Sharples, H. A. Frank, V. Sundström, and T. Polívka. 2004. Effect of a conjugated carbonyl group on the photophysical properties of carotenoids. *Phys. Chem. Chem. Phys.* 6:3009–3016

118

# List of publications

## **Publications on international journals**

1. M. Zavelani-Rossi, D. Polli, G. Cerullo, S. De Silvestri, L. Gallmann, G. Steinmeyer, U. Keller

"Few-optical-cycle laser pulses by OPA: broadband chirped mirror compression and SPIDER characterization"

**Applied Physics B 74**, s245 (2002)

2. G. Cerullo, D. Polli, G. Lanzani, S. De Silvestri, H. Hashimoto, R.J. Cogdell "Photosynthetic Light Harvesting by Carotenoids: Detection of an Intermediate Excited State"

Science 298, 2395 (2002)

- 3. R. Osellame, S. Taccheo, G. Cerullo, M. Marangoni, D. Polli, R. Ramponi, P. Laporta, and S. De Silvestri "Optical gain in Er-Yb doped waveguides fabricated by femtosecond laser pulses" Electronics Letters 38, 964 (2002)
- 4. G. Cerullo, R. Osellame, S. Taccheo, M. Marangoni, D. Polli, R. Ramponi, P. Laporta, and S. De Silvestri "Femtosecond micromachining of symmetric waveguides at 1.5 micron by astigmatic beam focusing"

  Optics Letters 27, 1938 (2002)
- 5. D. Polli, G. Cerullo, G. Lanzani, S. De Silvestri, H. Hashimoto, R.J. Cogdell "Excited state dynamics of carotenoids with different conjugation length" **Synthetic Metals 139**, 893 (2003)
- 6. R. Osellame, S. Taccheo, M. Marangoni, R. Ramponi, P. Laporta, D. Polli, S. De Silvestri, and G. Cerullo

"Femtosecond writing of active optical waveguides with astigmatically shaped beams"

Journal of the Optical Society of America B 20, 1559 (2003)

- 7. G. Lanzani, G. Cerullo, D. Polli, A. Gambetta, M. Zavelani-Rossi, C. Gadermaier "Photophysics of Conjugated Polymers: the contribution of ultrafast spectroscopy" Physica Status Solidi (a) 201, 1116 (2004)
- 8. M. Labardi, M. Allegrini, M. Zavelani-Rossi, D. Polli, G. Cerullo, S. De Silvestri and O. Svelto

"Highly Efficient Second-Harmonic Nanosource for Near-Field Optics and Microscopy"

**Optics Letters 29**, 62 (2004)

- 9. H. Hashimoto, K. Yanagi, M. Yoshizawa, D. Polli, G. Cerullo, G. Lanzani, S. De Silvestri, A.T. Gardiner and R.J. Cogdell "The Very Early Events Following Photoexcitation of Carotenoids" Archive of Biochemistry and Biophysics 430, 61-69 (2004)
- 10. D. Polli, G. Cerullo, G. Lanzani, S. De Silvestri, K. Yanagi, H. Hashimoto, and R. J. Cogdell

"Conjugation Length Dependence of Internal Conversion in Carotenoids: Role of the Intermediate State"

**Physical Review Letters 93**, 163002 (2004)

11. M. Labardi, M. Zavelani-Rossi, D. Polli, G. Cerullo, M. Allegrini, S. De Silvestri and O Svelto

"Characterization of femtosecond light pulses coupled to hollow-pyramid near-field probes: Localization in space and time"

**Applied Physics Letters 86**, 031105 (2005)

## **Publications on international books**

- 12. G. Cerullo, S. De Silvestri, G. Lanzani, D. Polli, M. Zavelani-Rossi and R.J. Cogdell
  - "Early events of energy relaxation in carotenoids probed by sub-10-fs optical pulses"

**Recent Advances in Ultrafast Spectroscopy** edited by S. Califano, P. Foggi e R. Righini, pp 29-36, (Leo S. Olschki, Firenze, 2003).

- 13. M. Zavelani-Rossi, M. Labardi, D. Polli, G. Cerullo, S. De silvestri, M. Allegrini, and O. Svelto
  - "Highly Efficient Second-Harmonic Nanosource by Femtosecond Pulse Irradiation of a Metal Tip"
  - **Ultrafast Optics IV** edited by F. Krausz, G. Korn, P. Corkum, and I.A. Walmsley, pp 457-462 (Springer Series in Optical Sciences 2004 Volume **95** <u>ISBN</u>: 0-387-40091-5)
- 14. G. Lanzani, G. Cerullo, D. Polli, A. Gambetta, M. Zavelani-Rossi, C. Gadermaier "Photophysics of Conjugated Polymers: the contribution of ultrafast spectroscopy" **Physics of Organic Semiconductors** edited by Wolfgang Bruetting (ISBN 3-527-40550-X) (Wiley-VCH, 2004)